2015

Material phase change under extreme domain confinement in laser material interaction

Chong Li
Iowa State University

Material phase change under extreme domain confinement in laser material interaction

by

Chong Li

A dissertation submitted to the graduate faculty

in partial fulfillment of the requirements for the degree of

DOCTOR OF PHILOSOPHY

Major: Mechanical Engineering

Program of Study Committee:
Xinwei Wang, Major Professor
Meng Lu
Hui Hu
Shankar Subramaniam
Daniel Attinger

Iowa State University

Ames, Iowa

2015

TABLE OF CONTENTS

LIST OF FIGURES

ACKNOWLEGEMENTS

First of all, I am grateful to my major professor, Prof. Xinwei Wang for his help in the last four years. This work cannot be accomplished well without his help. His passion and enthusiasm of the research and work impresses me and inspires me to be dedicated to my future work. In addition, he is more than an advisor. He is a friend and what I got from him is more than the academic knowledge. The life wisdom which I got from him would benefit me throughout my life.

Secondly, I appreciate the effort of all the professors in my committee. Thanks to Prof. Hui Hu, Prof. Daniel Attinger, Prof. Meng Lu, Prof. Shankar Subramaniam for their good questions and brilliant suggestions. Their support is greatly appreciated.

Thirdly, I would like to thank my brother, my sister in law and my parents and other relatives. Without their encouragement and support, I cannot accomplish what I have done. And last but not the least, I also want to say thank you to my colleagues and my friends. They helped me get through the difficult time in this study. I wish all of them a great career and future.

Additionally, support of this work by the National Science Foundation (No. CMMI-1029072) is gratefully acknowledged.

ABSTRACT

Laser has been widely applied in the science and industry fields because of the good spatial and temporal coherence and narrow spectrum. And the spatial confinement is common in the laser-assisted manufacturing field and it results in the change of the manufacturing process. However, due to the short time duration and high energy, the underlying physics is hard to be probed by experiment. Molecular dynamic (MD) simulation is employed to investigate the phenomenon related to the spatial confinement which includes the shock wave, wall confinement in cold sintering and laser induced breakdown spectroscopy (LIBS) enhancement and the tip confinement in surface nanostructuring.

Existence of the shock wave affects the phase change and stress wave development and propagation significantly. It suppressed the bubble growth and shortened their lifetime. No effect from shock wave on the stress wave in solid was observed. The absorption depth and laser fluence played important roles in the stress wave formation and evolution. Secondary stress wave in the target occurred because of the ablated cluster re-deposition.

The final cold-sintered structure was found to be nanocrystalline. Smaller nanoparticles were easy to reconstruct, but the final structure was more destructed, and structural defects were observed. For larger particles, the final cold-sintered structure was partially nanocrystalline. The orientation-radial distribution function (ODF) was developed to investigate the degree of orientation twisting. It was proved to be more

comprehensive than radial distribution function (RDF) in structure analysis for the additional angle information it provides.

Spatial confinement was found effective in improving the sensitivity of laser-induced breakdown spectroscopy (LIBS). The temperature, pressure and number density of the shock wave were observed to increase dramatically immediately after the reflection from the wall. The reflected shock wave and the forward-moving shock wave had a strong collision, and such an atomic collision/friction made the velocity of the shock wave decreases to almost zero after reflection. A temperature rise as high as 218 *K* was observed for the shock wave front after the wall reflection. More importantly, the temperature of the plume is enhanced dramatically from 89 *K* to 132 *K*. Also this high temperature was maintained for quite a long time. This explains the sensitivity enhancement in the spatial confinement of LIBS.

Nanoscale-tip based laser surface nanostructuring is a promising technique for ultrahigh density data storage and nanoelectronics industries. The phase change (e.g. melting, phase explosion, and solidification/re-crystallization) within the tip-substrate region is extremely confined at the scale of a few nm. Such extreme domain constraint could significantly affect the structuring process and the tip apex profile. On the other hand, little is known about this extremely confined phase change by both computer modeling and experiment. In this work, systematic atomistic modeling is employed to explore the tip-confinement effect on the surface nanostructuring. Material ablation is trapped by the tip and the number of atoms flying out from the substrate decreases due to

the tip-confinement. Although large atom-clusters are observed in tip-free scenario, no such clusters are observed in tip-based surface nanostructuring. This is favorable for making nanoscale surface structures. Tip apex oscillation occurs because of its interaction with the substrate. The effect of tip-substrate distance and laser fluence on the surface nanostructuring is investigated in detail. The profile of the cone-shape crater in the substrate is not affected much by the tip-substrate distance. Instead, the laser fluence plays a dominant role in the final crater shape. The protrusion around the crater is affected by both the tip-substrate distance and the laser fluence. For the case of tip-substrate distance d= 7 nm, the protrusion is flatter but wider than d= 1 nm and 2 nm. The tip-confinement also affects the recrystallization process after laser heating. The recrystallization time is longer for the case with tip confinement due to the interaction between the tip and the substrate. The tip apex is distorted during laser ablation. Both the tip-substrate distance and the laser fluence play import roles in the distortion. For the case of laser fluence E= 10 J/m^2, the tip apex is reshaped to be blunt. The nanotip-laser interaction (near-field focusing) could change negatively due to the tip-apex reshaping, and this change will induce undesirable surface nanostructure change. Although the tip-substrate confinement significantly prolongs the solidification/recrystallization process in the substrate, it has little negative effect on the defects formed in the nanostructuring region.

CHAPTER 1. INTRODUCTION

1.1. Effect of shock wave on phase change and stress wave in pico-second laser-material interaction

Over the last few decades, interaction between material and ultrafast pulsed lasers has captured significant attention because of the wide applications of ultrafast lasers in matrix assisted laser desorption (MALDI) [1], laser surgery, microfabrication, pulsed laser deposition (PLD) [2-7] *etc*. Laser material interaction is an extremely complicate process involving optical absorption, mechanical stress generation and propagation, melting, vaporization, and solidification. When the incident laser energy is high enough for a specific material, phase explosion takes place. And when laser material interaction happens under an environment with ambient gas instead of vacuum, a shock wave could form. Numerous simulation and experimental studies have been carried out to investigate the above problems. Song *et al.* [8] used nickel as the specimen to study the laser fluence threshold for phase explosion. In their work [9, 10], it was discovered that extra time is needed for phase explosion to happen and the time lag is around a few nanoseconds under experimental conditions for nickel irradiated by a KrF excimer laser with a wavelength of 248 nm and a pulse width of 25 ns. In the molten region, nucleation and bubble growth during laser and material interaction has been experimentally explored by Park *et al.* [11] and Yavas, *et al.* [12]. Experimental studies about plume structure, dynamics and evolution have also been reported [13, 14].

Accompanying the substantial experimental work, a large amount of simulation work at atomic level has been devoted to obtaining insight into the underlying physics of laser material interaction. Owing to the rapid development of computer technology, the number of atoms that can be studied in simulation has increased dramatically. In one outstanding work by Zhigilei *et al*. [15], the influence of laser irradiation parameters like laser fluence, pulse duration, and initial temperature of the sample on laser ablation is studied systematically and dynamics of plumes are described in detail. Zhang and Wang explored the long-time material behavior in nanosecond laser-material interaction by using large-scale hybrid atomistic macroscale simulation [16]. Other simulation work about the ablation plume and ejected clusters, evaporation and condensation can be found in literatures [13,17-18].

The existence of background gas can significantly affect the dynamics evolution of gas environment, the ablated plume and specimen during laser ablation. Simulation about plume propagation in vacuum and background gas has been reported [19]. Nanoscale shock wave results from the interaction between ejected target atoms and ambient gas. Details of such shock wave behavior can be seen in Feng and Wang's work [20] and visual evidence is provided by Porneala and Willis [21]. Gacek and Wang [22] gave a detailed description of the shock wave dynamics and evolution. Other phenomena related to shock wave such as mutual mass penetration and secondary shock wave have been explored. [22-25]

Voids and bubbles in the molten region are also great concerns for researchers since they are directly related to the phase change process and final surface quality. Zhigilei *et al*. [15] systematically discussed the reason for nucleation and spallation. The tensile stress

generated in laser ablation and the material's ability to withstand the tensile stress is pointed out to be the key for material fracture.

Although laser material interaction has been investigated widely, there still remain some interesting things uncovered. This work studies bubble lifetime and evolution process under the effect of shock wave. Emphasis is placed on the investigation of physical parameters such as stress, temperature and atom number density contour. Furthermore, the effect of ambient gas on stress wave generation and propagation in the solid is studied in detail.

1.2. Structure evolution of nanoparticles under pico-second stress wave consolidation

As a byproduct of laser ablation, the high speed plume gives rise to shock wave in the ambient gas. A transparent overlay was placed on the sacrificial material and specimen to induce a shock wave propagating downwards toward the specimen. Laser-induced compressive stress waves have the potential to compress micro/nanoparticles to form the desired structure. Zhang *et al* have reported the microscale effects of laser shock wave used to obtain the desired residual stress patterns in microcomponents [26, 27]. And Molian *et al* have confirmed that the laser shock wave process can help with generating a strong, wear resistant, durable composite coating on aluminum [28]. In the past, laser shock peening (LSP) has been employed as a surface treatment of metals and was widely applied for turbine engine components. It has the advantage of improving surface properties of metallic components by introducing compressive residual stresses. Peyre *et al* found that the pitting corrosion resistance of 316L steel was improved after laser peening [29]. Lin *et al* discovered

that the combination of laser sintering (LS) and LSP contributes to better fatigue performance [30]. Finite element analysis has been applied to simulate the LSP procedure [31-33].

The interaction of nanoparticles with incident lasers is of great importance in the manufacturing field. Selective laser sintering (SLS) sinters powders of microscale in a layer-by-layer style. Nanoparticle additive manufacturing has been proposed by Nair *et al* as a novel solid freeform fabrication process [34]. In laser sintering, particles/powders will be melted, and then solidify to form a consolidated part. For environment or substrate that cannot sustain such high temperature (melting point of the powder), it becomes challenging to sinter powders on a substrate without severely damaging it.

A new laser-assisted low-temperature consolidation method is come up with numerically. Laser irradiation is employed to generate the stress wave to compress the nanoparticles to achieve cold sintering. Cold sintering has advantages of consolidating powders of weak laser absorption or difficult to melt, or sintering nanoparticles on a substrate that cannot sustain a high temperature. We intend to investigate the various physical processes during stress wave-induced consolidation, in anticipation to unveil how the nanoparticle structure evolves to become dense.

1.3. Shock wave confinement-induced plume temperature increase in laser-induced breakdown spectroscopy

Laser-induced breakdown spectroscopy (LIBS) is a technique developed for element analysis with a laser serving as the excitation source. The wavelength of the electromagnetic irradiation from the excited plasma at high temperatures is analyzed selectively for the presence of analytes and the intensity is proportional to their content concentration in the sample [35-38]. In the past decades, LIBS has been developed into a mature technology and is widely used in multi-component analysis of element composition [39, 40], cultural heritage in-situ investigation [41, 42], steel manufacturing industry [36, 43], environmental monitoring [44] *etc*.

All of the analyses are carried out based on the frequencies of the emitting light from the elements when it is excited to a sufficiently high temperature. Several factors, such as the plasma excitation temperature, the light collection window and the line strength of the viewed transition affect the sensitivity and accuracy of LIBS. A lot of works have been devoted to improving this technique. All the experimental components in LIBS can be made to be miniature and portable. And a large number of works are carried out to make this technique reliable and rugged in the standoff and in-situ analysis [45-48]. Dual pulse LIBS was proposed as a way to overcome the shortcoming of poor sensitivity of the conventional single pulse LIBS by increasing the efficiency of the production of analyte atoms in the excited state [49-52]. At the same time, the combinations of lasers of different wavelengths, pulse sequence and pulse width were investigated for the optimal performance in LIBS [53-55]. Long nanosecond pulses were discovered to be more favorable for the LIBS application

due to the relatively slow heating of the plasma, causing a larger and less-dense plume and therefore fairly intense and less broadened emission lines [56, 57].

Recently, spatial confinement has captured a lot of attention from researchers. It was found effective in increasing the plasma shock wave pressure [58]. Plasma temperature increase and enhanced emission intensity were also observed [59-62]. Different spatial confinement shapes have been studied in Lu's group, which include a pair of parallel walls [59], a pipe [60], and a hemispherical cavity [61]. A temperature rise as high as 3600 *K* was reported by their group in the Mn element analysis excited by the KrF excimer laser with the sample trapped in a hemispherical cap. The compression of the plasma by the reflected shock wave was found to account for the increase of the plasma temperature. Consequently, it leads to great sensitivity improvement of LIBS.

In spite of the interesting spatial confinement phenomenon and the significant temperature and intensity enhancement, little work has been done to unveil the underlying physical mechanism in the sensitivity enhancement. Molecular dynamic (MD) simulation is employed in this work and a potential wall boundary condition is adopted to simulate the wall confinement. A comparison of the confinement case (with potential walls) and free-space case (without potential walls) is made, in an attempt to uncover the energy conversion process and the enhancement physics.

1.4. Material behavior under extreme domain constraint in laser-assisted surface nanostructuring

Surface nanostructuring is an active research area in the last decades because of its promising application in high-resolution nanolithography, ultrahigh density storage, nanoeletronics, and nanophotonics *etc*. [73] Nowadays, miniaturization is the trend of the electronic and mechanical devices. However, the traditional maskless manufacturing techniques are challenged by the diffraction limit. To meet the needs in industries, great effort has been devoted to the development of scanning probe microscopy (SPM) techniques [74-76] which enable ultrahigh surface imaging and characterization [77-80] as well as surface modification at the molecular level. [73]

SPM, which measures the surface topography and properties by scanning the specimen, is a wide spectrum of microscopy techniques including near-field scanning optical microscopy (NSOM) [81, 82], scanning tunneling microscopy (STM) [83], and atomic force microscopy (AFM) [78, 84] *etc*. There are two modes of NSOM, the aperture mode and the apertureless mode. The combination of laser illumination and a sharp tip (tungsten tip, probe of AFM *etc*) yields the apertureless near-field scanning optical microscopy. A resolution as small as 1 nm has been declared for the apertureless mode. [85, 86] For surface nanostructuring, processing structure down to 10 nm has been accomplished. [87-89] And field enhancement [90-94] at the nanoscale and the thermal expansion of tip [95-98] are observed in this apertureless mode. Lu *et al*. demonstrated that the field enhancement and the mechanical indentation resulting from the AFM tip can be applied effectively in the surface nanostructuring in their works. [99, 100]

Not only is the combination of laser and the AFM tip applied in the surface nanostructuring, but also used in the near-field technique, surface enhanced Raman scattering (SERS) [101-103] and tip enhanced Raman scattering (TERS) [104-107]. Raman spectrum arises from the vibrational frequencies of molecules and provides material information which is particularly valuable in chemistry. [108] Combined with the near-field technique, tip enhanced Raman scattering (TERS) has become a powerful tool for material analysis at the nanoscale. Considering the close distance between the tip and the substrate which may result in measurement instability, the thermal expansion of the tip and substrate has been studied extensively. [109, 110] Chen *et al* employed the finite element method (FEM) to simulate the electromagnetic field of the tungsten SPM tip and silicon substrate system under laser irradiation. [111] Tip-substrate distance effect and the optimum tip apex radius for different half taper angles are declared. Yue *et al*. explored the thermal transport at sub-10 nm scale with different polarization angles of the incident laser in their experiment and simulation. [112] A temperature rise as high as 250°C on the silicon substrate for polariation angle of 15° and 30° was reported in their work.

Molecular dynamics (MD) simulation is helpful in understanding the underlying physics from the molecular level. It has been widely applied in exploration of the physical mechanisms in laser-material interaction. [7, 70, 113, 114] Wang studied the thermal and mechanical behavior in surface nanostructuring with laser-assisted STM. [25] The solidification and epitaxial growth [68], the molecular weight and density of the ambient gas [115] have also been studied in surface nanostructuring. Feng *et al.* explored the shock wave

in near-field laser material interaction and the kinetic and physical properties of the shock wave was revealed. [20]

The aforementioned MD simulation works provide great understanding of the physical phenomena of melting, crystallization and the environment effect. However, they all exclude the effect of the tip-confinement. Considering the close distance between the SPM tip and the substrate which is at the molecular level, the effect of the spatial confinement of the tip apex may result in more complicated physical phenomena in surface nanostructuring. Also this knowledge will help understand how and to what extent the tip apex could be damaged by surface nanostructuring. In this work, a nanoscale size tip needle is included to study the tip-confinement effect in the surface nanostructuring process. The tip-substrate distance and the laser fluence's effect are studied in detail. Also tip-apex distortion is studied under different nanostructuring conditions.

CHAPTER 2. EFFECT OF SHOCK WAVE ON PHASE CHANGE AND STRESS WAVE IN PICO-SECOND LASER-MATERIAL INTERACTION

In this chapter, voids lifetime and evolution process under the effect of shock wave are studied. Emphasis is placed on the investigation of physical parameters such as stress, temperature and atom number density contour. Furthermore, the effect of ambient gas on stress wave generation and propagation in the solid is studied in detail. In Section 2.1, the methodologies will be first introduced. The laser energy absorption manner and boundary is specified. Section 2.2 provides MD simulation results which include the atomic snapshots, the temperature and stress contour. Voids dynamics and stress wave evolution are analyzed systematically as well.

2.1. Methodologies

Since argon has simple face-centered cubic (fcc) crystal structure and the interaction between atoms can be precisely and conveniently described by the Lennard-Jones (12-6) potential, it has been selected as the object to investigate laser ablation and shock wave in a lot of literatures [16, 22, 24]. In this work, for simplicity, we also choose argon as the crystal material to study and adopt a model similar to Gacek and Wang's paper [22], as shown in Fig. 1(a).

2.1.1. Simulation model

Shock wave can only form when there exists ambient gas around the crystal target which is going to be irradiated by a pulsed laser. Given our purpose is to study the effect of shock wave on other dynamics problems, and to save the computation cost, we choose argon

as the ambient gas but at the same time we make some modifications to the Lennard-Jones potential to describe the interaction of gas atoms. The original Lennard-Jones (12-6) potential is expressed as

$$\phi_{ij} = 4\varepsilon\left[\left(\sigma / r_{ij}\right)^{12} - \left(\sigma / r_{ij}\right)^{6}\right] \tag{1}$$

where the first term on the right represents the repulsive force potential and the second one is for the attractive force potential. We only consider the repulsive force in the interaction of gas-gas atoms and gas-target atoms while take both repulsive and attractive forces into account in the target-target atoms interaction. ε and σ are well depth and equilibrium separation parameter for the LJ potential, which are set to be 1.653×10^{-21} J and 3.406 Å respectively. r_{ij} in the above equation denotes the pair separation that can be expressed as $r_{ij}=r_i-r_j$.

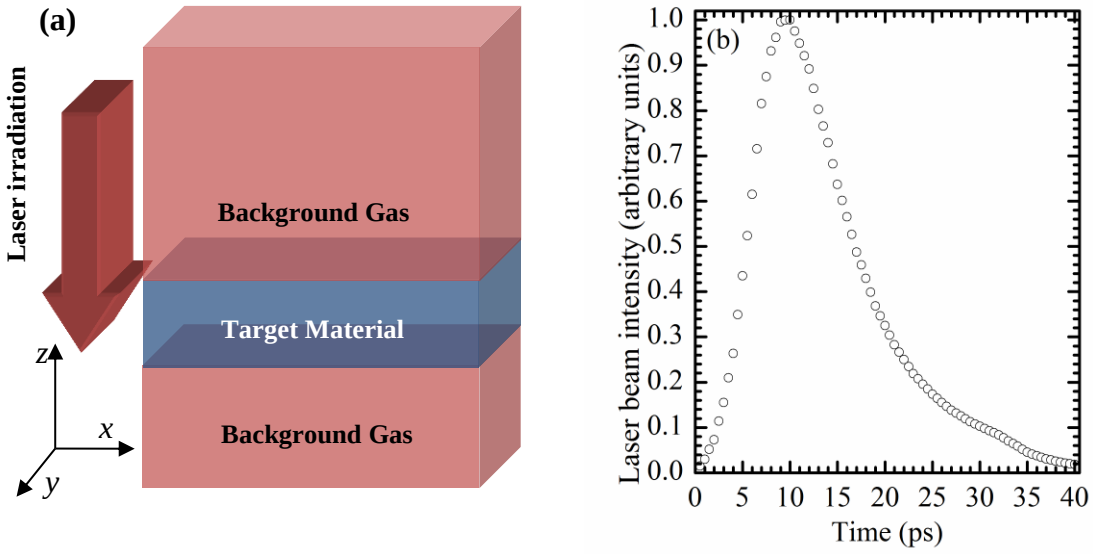

Fig. 2.1 Illustration for domain construction and incident laser irradiation. (a) Blue region is the target and the red regions are the gas atoms. Laser irradiation is in the negative *z* direction. (b) Schematic of laser intensity distribution.

In this model, argon lattice constant is 5.414 Å. The computation domain contains 337500 atoms and measures 32.5×2.7×3627 (nm) ($x \times y \times z$). Figure 1(b) shows the incident laser beam intensity distribution with full width at half maximum (FWHM) 11.5 ps peaked at 9 ps. In order to simulate the situation where the material exposed to a gas environment is irradiated by a laser pulse and eliminate the surface effect, we set the boundaries in *x*, *y* and *z* directions periodical. MD simulation work in this article is performed with the LAMMPS package [63]. The equilibrium temperature chosen for this MD simulation is 50K and the time step is set to be 25 femtoseconds. The cutoff distance is chosen as 2.5σ. Before laser irradiation is applied, the whole system is thermostated and equilibrated at 50K for 3.75 ns by running as a canonical (NVT) ensemble. After that, we run the whole system as a microcanonical (NVE) ensemble for 250 ps. When thermal equilibrium is reached, pressure of the ambient gas is approximately 0.23 MPa. Because this work is to describe and study the phenomena related to shock wave, there is no need to make the ambient gas pressure equal to 1 atm. Other specific details about the modeling can also be found in papers [22,24].

2.1.2. Laser energy absorption manner and non-absorption boundary condition

After equilibrium calculation, laser heating is applied on the target in the negative *z* direction and is absorbed volumetrically in the target. To perform it, the target is divided into a group of bins with equal thickness of δz. For each time step, the incident laser energy is absorbed exponentially and can be expressed as [22]

$$\Delta E = E_0\left[1-\exp(-\delta z / \tau_0)\right] \tag{2}$$

where τ_0 is the adjusted real optical absorption depth and calculated as $\tau_0 = \tau \cdot \rho_0/\rho_1$. ρ_0 *and* ρ_1 are the density for bin and whole target respectively. τ is an artificial absorption depth.

To add the absorbed energy into atoms within each bin, we scale the velocities of atoms by a factor of [22]

$$\chi = \sqrt{1 + \Delta E / \left[0.5 \Sigma_{i=1}^{N} m_i ((v_{i,1} - \bar{v}_1)^2 + (v_{i,2} - \bar{v}_2)^2 + (v_{i,3} - \bar{v}_3)^2) \right]} \quad (3)$$

where $v_{i,j}$ and v_j are the velocity of atom i and the average velocity of atoms in each target bin in x, y, z directions. The new velocity for atom i is calculated as

$$v'_{i,j} = (v_{i,j} - \bar{v}_j) \cdot \chi + \bar{v}_j \quad (4)$$

Laser induces the generation and propagation of stress wave. Once the stress wave reaches the target bottom, it will be reflected and become tensile stress propagating towards the irradiation surface. When tensile stress exceeds what the material can support, fracture of material will occur. With further propagation, the stress wave can possibly reach the vapor-gas zone and finally affect shock wave and other related phenomenon. To get rid of the artifact from stress wave reflection in the target, an external force is added to a specified bottom layer which is approximately 10 Å thick. This stress terminating force is calculated as

$$F_t = -\frac{\rho \cdot v \cdot c \cdot A}{N} \quad (5)$$

where ρ represents density of the designated bottom layer, v the atoms average velocity corresponding to each time step in the layer, c the propagation speed of stress wave which is approximately 1333m/s [7], and A denotes the area normal to the incident laser beam. N is the number of atoms within the bottom layer at each corresponding time step. Our work[7, 22] has proved the validity of this method. During our MD simulation, atomistic snapshots and the velocity plots are examined. No movement of the target is observed and stress wave is not reflected by the bottom. This means the procedure of adding force is effective in eliminating the undesired stress wave reflection at the back boundary.

2.2. Results and Discussion

Firstly, the general pictures of the shock wave evolution and phase change is presented. Afterwards, the voids dynamics is investigated. Right after that, the effect of the laser fluence and ambient gas is taken into consideration. The re-deposition of the ejected clusters and the stress wave in the target are discussed in the last two parts of this chapter.

2.2.1. General picture of phase change under shock wave

The case with a laser fluence of 3 J/m^2 and ambient gas pressure of 0.23 MPa is chosen to describe phase change under the existence of shock wave. Figure 2.2 shows the shock wave evolution. Figure 2.2(a) is for case E= 3 J/m^2 and τ= 5 nm, and Figure 2.2(b) is for E= 3 J/m^2 and τ= 15 nm. In Fig. 2.2(a) the incident laser beam causes material to evaporate violently because its energy intensity exceeds the material ablation threshold. Quickly after the laser pulse stops at t= 40 ps, thermal expansion is predominant and a large number of atoms escape from the target surface because of high pressure from intense phase explosion. The ejected plume moves in a speed higher than sound velocity, and serves like a piston to compress the ambient gas and finally leads to the formation of an evidently strong shock wave at the nanoscale.

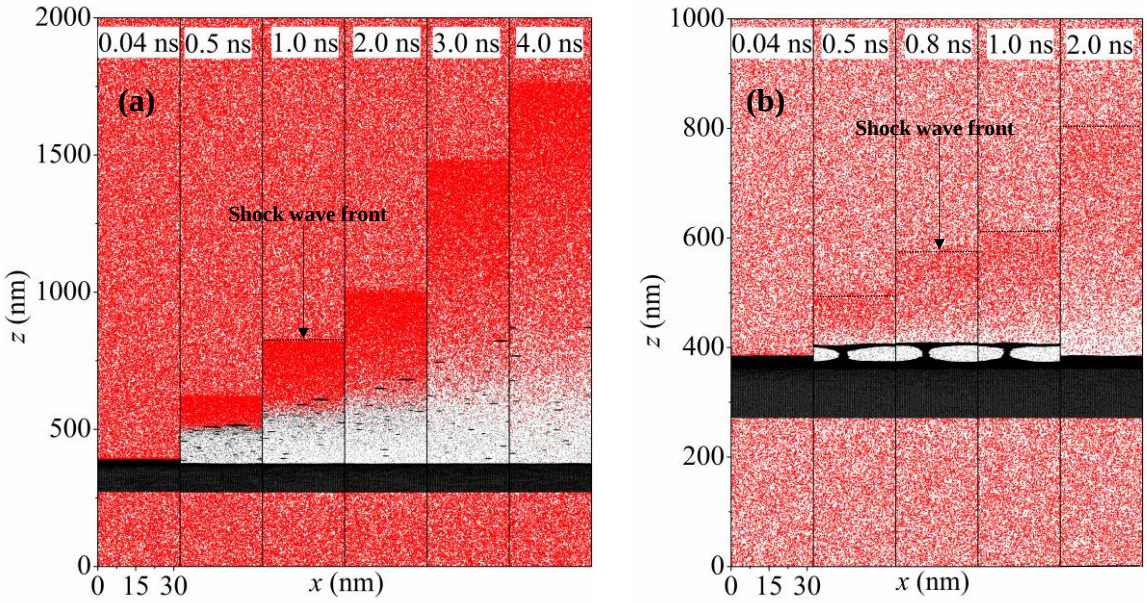

Fig. 2.2 Snapshots for shock wave formation and dynamic evolution. (a) Incident laser fluence E= 3 J/m^2 and the absorption depth τ is 5 nm; (b) E= 3 J/m^2 and τ= 15 nm. Red dots in the atomistic snapshots represent the gas atoms while black ones are for target atoms. Dense red region is the shock wave front, as shown by the dot line in the figures. The shock wave is less visible for τ= 15 nm than that for τ= 5 nm. A big bubble exists in figure (b) from 0.5 ns to 1.0 ns.

For E= 3 J/m^2 and τ= 5 nm, the phenomenon of laser material ablation is similar to that in vacuum at the beginning as illustrated in the atomic configuration part of Fig. 2.8. The sound explanation is that the plume mass and density are prominently larger than those of the ambient gas at the very onset of laser ablation. The impact of background gas can be neglected compared with plume expansion. Nanoparticles account for a large portion of the ejected plume near the surface region. With time going by, plume with high energy penetrates into the background gas continuously. The co-existence region of gas and target atoms expands. An increasing amount of ambient gas will be trapped in the shock wave front and finally strong repulsion from the background gas prevents the ejected plume from

propagating in space. From Fig. 2.8, it is obvious that the ejected layer of targets are in front of that without gas for t= 0.07 ns and t= 0.08 ns. Comparison among the process at 2 ns, 3 ns, and 4 ns in Fig. 2.2(a) demonstrates that the plume is stopped from propagating forward and slightly moving backward started from 3 ns. Thermalization of plume occurs during this period of time. Part of plume's translational kinetic energy is converted into its thermal energy. Figures 2.5(a) and (b) are spatiotemporal temperature contours for E= 3 J/m^2 and τ= 15 nm and E= 3 J/m^2 and τ= 5 nm. The slope line represents the moving of shock wave. There is a temperature rise in the place where the shock wave travels. The ambient gas significantly reduces the velocity of the expansion plume and the speed of the leading shock wave front decreases from 550 m/s at 0.5 ns to 360 m/s at 3 ns for E= 3 J/m^2 and τ= 5 nm. The curved temperature profile in Figs. 2.5(a) and (b) also indicates this speed decrease. Detailed discussions about Fig. 2.5 will be provided later in this work.

The thermodynamics properties including density, temperature, pressure and velocity of the shock wave front changes dramatically during its propagation. At 0.5 ns in Fig. 2.2(a), a dense red region is already distinguished, which represents the shock wave expansion front. The front of shock wave has the highest density, and the density becomes smaller towards the plume-gas interface. The velocity, temperature and pressure show the same trend as density. Detailed analysis can be seen in our previous work [22, 23, 24]. This work will present these parameters with contours in a longer time scale within the whole simulation space to give a more in-depth analysis in the following part.

The laser absorption depth can be varied to control the energy absorption style in the target. When the absorption depth is increased from 5 nm to 15 nm, the phenomenon of phase change under shock wave is dramatically different from that before. Details are shown in Fig. 2.2(b). There is still a plume generated from laser ablation. However, because fewer atoms are ejected out, the plume is much less visible as shown by the comparison between (a) and (b) in Fig. 2.2. The dark red region that represents the shock wave is barely distinguished in Fig. 2.2(b). It is found at t= 0.5 ns, the shock wave front velocity decreases from 550 m/s at τ= 5 nm to 290 m/s at τ= 15 nm, although it is still larger than the local sound speed of 132 m/s in the ambient gas. Because of the low energy gained by the shock wave for τ= 15 nm, the plume and the dark red region will dissipate soon in the ambient gas. Interestingly, when the laser absorption length is set to be 15 nm, a large bubble is observed during the time 0.5~1.0 ns. The dynamics of bubbles evolution in the molten region will be discussed in detail in the next section.

2.2.2. Phase change and bubble dynamics in molten region

In essential, bubbles are fracture or spallation in material during laser-material interaction. Figure 2.3 depicts the bubble evolution. Figure 2.3(a) is for case E= 3 J/m^2, τ= 15 nm, with ambient gas; Figure 2.3(b) is for the case E= 2.5 J/m^2, τ= 15 nm, ambient gas is included in this model; and Figure 2.3(c) for the case E= 3 J/m^2, τ= 15 nm, without ambient gas. As illustrated in Fig. 2.3(b), at the end of laser irradiation (0.04 ns), voids are hardly visible. Only the solid and molten regions can be distinguished. However, when it comes to 0.10 ns, 60 ps after the laser irradiation, several bubbles are observed. They nucleate and grow, and then collapse soon.

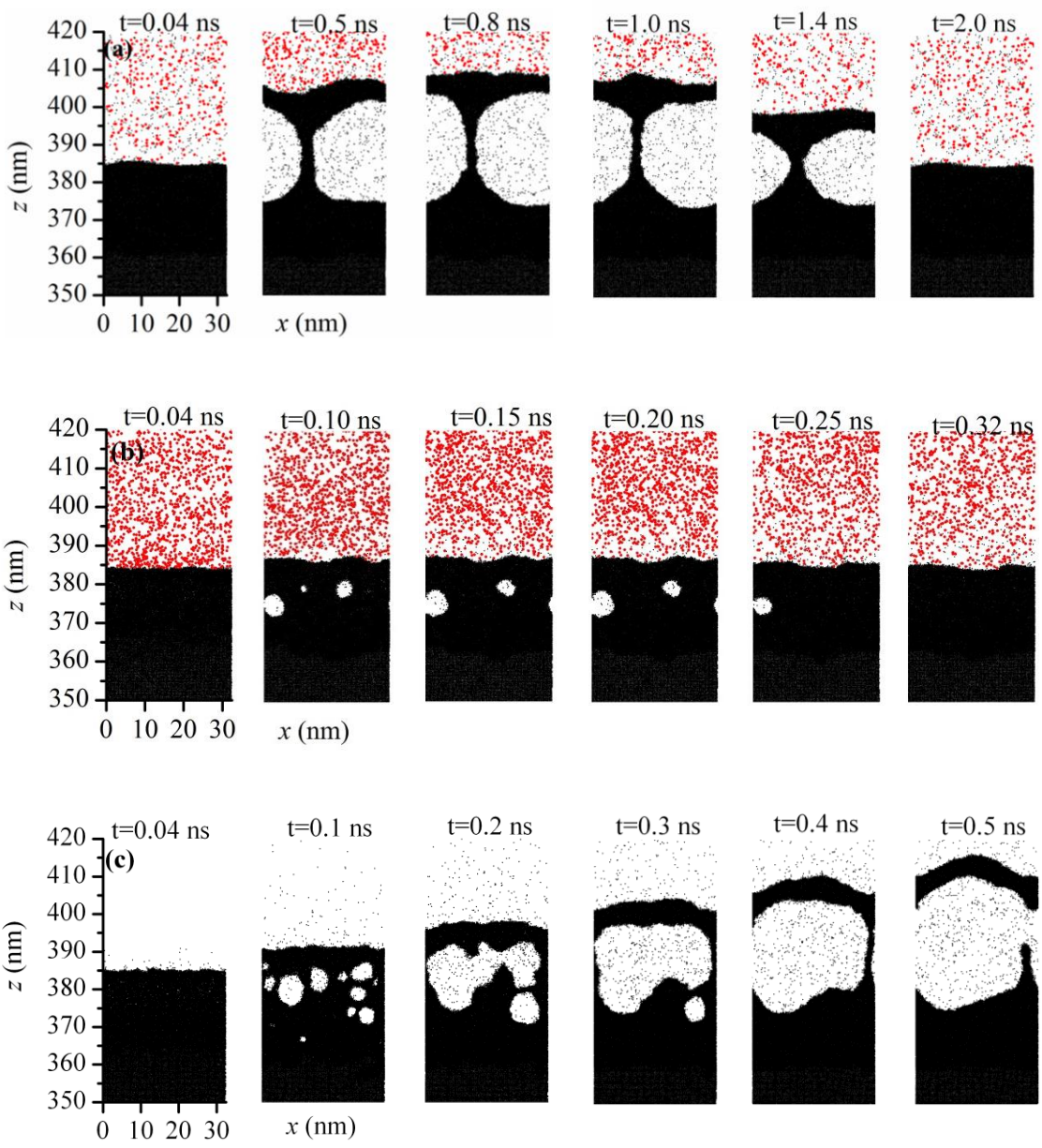

Fig. 2.3 Snapshots of bubble evolution: (a) E= 3 J/m^2 and τ= 15 nm with ambient gas. (b) E= 2.5 J/m^2 and τ= 15 nm with ambient gas. During 0.04 ns-0.32ns, bubble formation, growth and collapsing process is demonstrated. (c) E= 3 J/m^2 and τ= 15 nm without ambient gas. In order to have a close view of the bubble dynamics, only atoms within the 350-420 nm range in the z direction are plotted.

Zhigilei and Garrison [64] pointed out that the tensile stress resulting from the interaction of laser-induced pressure with the free surface is the main reason for bubble formation. It takes time for tensile stress to propagate along the irradiation direction and reach certain depth, where the maximum tensile strength exceeds the material's limit and consequently bubble formation is observed. In addition, the ability of material to support tensile stresses depends on temperature [65, 66]. The tensile strength limit for a material decreases as the temperature approaches the melting point. Figure 2.7 shows the atomic snapshots and stress wave for case E= 3 J/m^2, τ= 15 nm. Clearly, tensile stress does not attain the maximum value at the depth of 375 nm. However, bubbles are observed around the depth of 375 nm in Fig. 2.3(a). The relationship between the tensile stress limit and temperature should account for this phenomenon.

In this work, comparison between bubble evolution under laser fluence 3 J/m^2 and 2.5 J/m^2 is made. We can see that from the comparison between Fig. 2.3(a) and Fig. 2.3(b), when laser energy is increased, at the beginning of bubble formation, a wider molten region range and violent foamy structure is observed. With more energy absorbed during laser irradiation, more atoms gain enough energy to overcome the constraint force from the ambient gas and other solid atoms. At 0.5 ns, solid atoms above 370 nm disintegrate badly when E= 3 J/m^2 while in Fig. 2.3(b) the bubbles have collapsed. It can be noted from Fig. 2.3(b) that there are still some voids form and then collapse. In this situation the recoil effect from the ejected cluster and plume can also prevent some of the bubbles from growing and forces them to collapse significantly. In Fig. 2.3(a) all the bubbles form and grow into a big size bubble and then gradually collapse. The existence of background gas does affect the phase change and

bubble dynamics. When ambient gas is considered at laser fluence 3 J/m^2, collapse process is observed. However, for the scenario without ambient gas, a layer of atoms with a thickness of 10 nm in the *z* direction flies out.

Figure 2.4 shows the bubble evolution process and their lifetime under the situation E= 2.5 J/m^2, τ= 15 nm with the target placed in the gas environment. Figure 2.4(a) illustrates the index of bubbles studied in this figure. From the two-dimensional (2D) view it is noted that bubbles are not exactly round. Therefore an effective radius is used to describe the volume change. First of all, the 2-D area of bubbles is evaluated by MATLAB Image Processing Toolbox. Then the effective radius is derived by calculating the radius of a circle with the corresponding equal area. Finally, the effective volume can be obtained by multiplying the effective area by the length in the *y* direction (thickness), namely 2.7 nm. Figure 2.4(b) shows the radius change and derivative of radius against time is calculated to describe the bubbles growing/collapsing speed as shown in Fig. 2.4(c). Based on Fig. 2.4(c), the lifetime of bubbles can be calculated and is shown in Fig. 2.4(d).

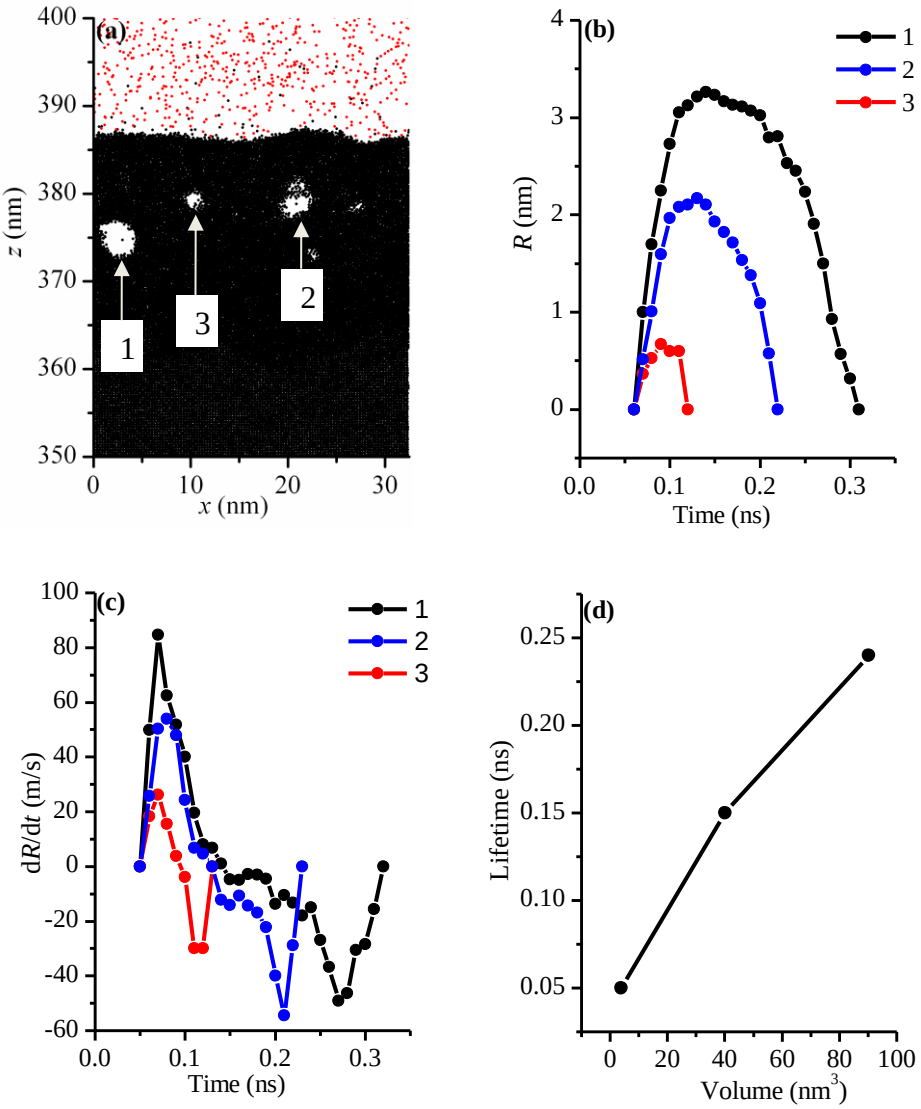

Fig. 2.4 Bubble dynamics for E= 2.5 J/m^2, τ= 15 nm: (a) bubble identity, snapshot for t= 0.08 ns is chosen for identity definition; (b) bubble radius at different times; (c) bubble radius evolution rate; (d) relationship between bubble lifetime and bubble volume.

We can see that bubble 1 which is located at the left hand side has the biggest volume and longest lifetime while bubble 3, the one at x= 10 nm has the shortest lifetime. All the voids experience a volume increase and decrease process during its lifetime. For bubble 1, it starts to grow in a relatively small rate at 0.04 ns, and then reaches the maximum growth rate of 85 m/s. Subsequently, it will grow in a smaller rate until reaching the maximum volume at

0.11 ns. After that it begins to contract and collapse. Besides, for bubbles with a large volume, there is a period within which it is quite stable. Bubble 1 is approximately stable from 0.12 ns to 0.18 ns [Fig. 2.4(c)]. Interestingly, from this figure we also notice that the growth and collapse processes are almost symmetric. Under the effect of tensile stress, the bubbles at first grow up quickly. However, the attraction force from the molten region and the repulsive force from ambient gas work together to prevent the voids from expansion. When the effect of the restraint force is dominant, we see a decelerating growth process. Otherwise, the bubbles will grow in an increasing rate. Generally, bubbles with a larger volume have a larger maximum growth rate of about 85 m/s, just like bubble 1. For smaller bubbles, as bubble 3, it has a much smaller peak change rate, approximately 26 m/s.

2.2.3. Dynamic physical process under the effect of shock wave

Comparison of temperature, stress, target atom number and gas atom number density is made in this work for detailed physical process analysis. Figure 2.5 depicts the spatiotemporal temperature and stress contours for E= 3 J/m^2, τ= 5 nm and E= 3 J/m^2, τ= 15 nm respectively. And Fig. 2.6 shows the atom number density contour for target and gas corresponding to these two cases. The time starts from the beginning of the laser irradiation and last for almost 5 ns in the simulation. For the target atom number density contour, there are dark and light strips which indicate the inequality of atom number density [Figs. 2.6(c) and (d)]. However, this is a false impression. To get the number density contour, the whole simulations box has to be divided into a number of small bins. In this work, for the contours, including the target atom and gas atom number density contours and stress contours, the whole space is divided into bins of 1 nm width in the z direction. Since the lattice constant of

argon crystal is 5.414 Å, 10 Å is definitely not the multiple of that. So the atoms contained in the bins may fluctuate in number slightly. This explains the dark and light strip lines in our contours, especially for the target part. For temperature contour, an interval of 21.656 Å is used in the *z* direction.

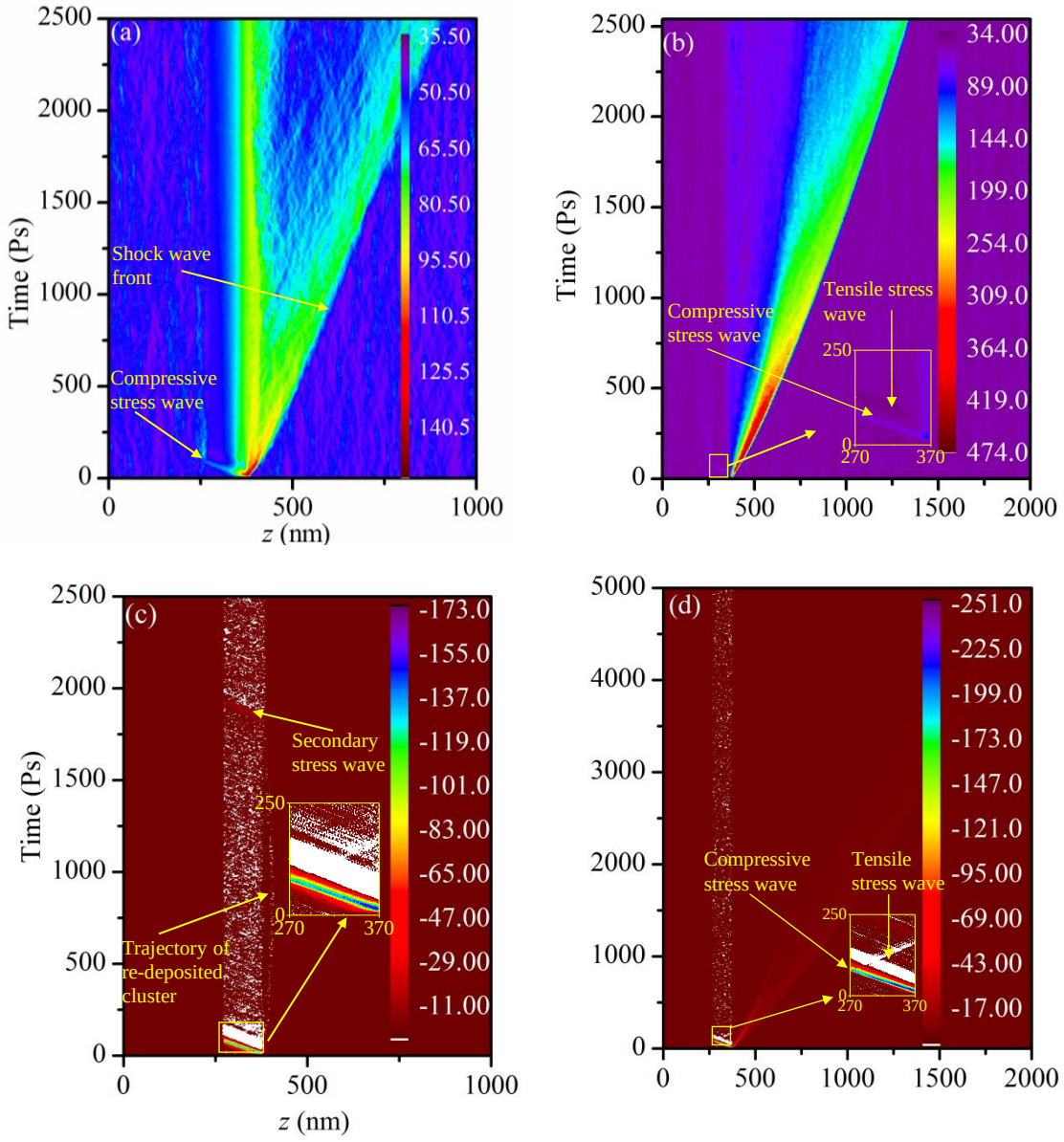

Fig. 2.5 (a) Spatiotemporal temperature contour for E= 3 J/m^2, τ= 15 nm; (b) temperature contour for E= 3 J/m^2, τ= 5 nm, zoom-in plot is used to illustrate the temperature relationship

with stress wave; (c) stress contour for E= 3 J/m^2, τ= 15nm; (d) stress contour for E= 3 J/m^2, τ= 5nm. The slope lines in the temperature contours indicate the development of the shock wave. There is a temperature drop along time in the contours. A secondary stress wave is shown in figure (c) in the zoom-in figure.

The absorption depth does strongly impact phase change and the stress wave evolution. The increase of absorption depth can expand the depth of receiving significant amount of laser energy. In the following part, detailed analysis of the difference will be presented. The shock wave expansion velocity is different for the two absorption depths used here. For 3 J/m^2, τ= 5 nm, the shock wave moves faster. As shown in Fig. 2.5(a), at 2.5 ns, the shock wave generated by the laser irradiation of 3 J/m^2, τ= 5 nm moves to the vicinity of z= 1300 nm, while the one induced by laser irradiation of 3 J/m^2, τ= 15 nm only travels to a place right below z= 1000 nm [shown in Fig. 2.5(b)].

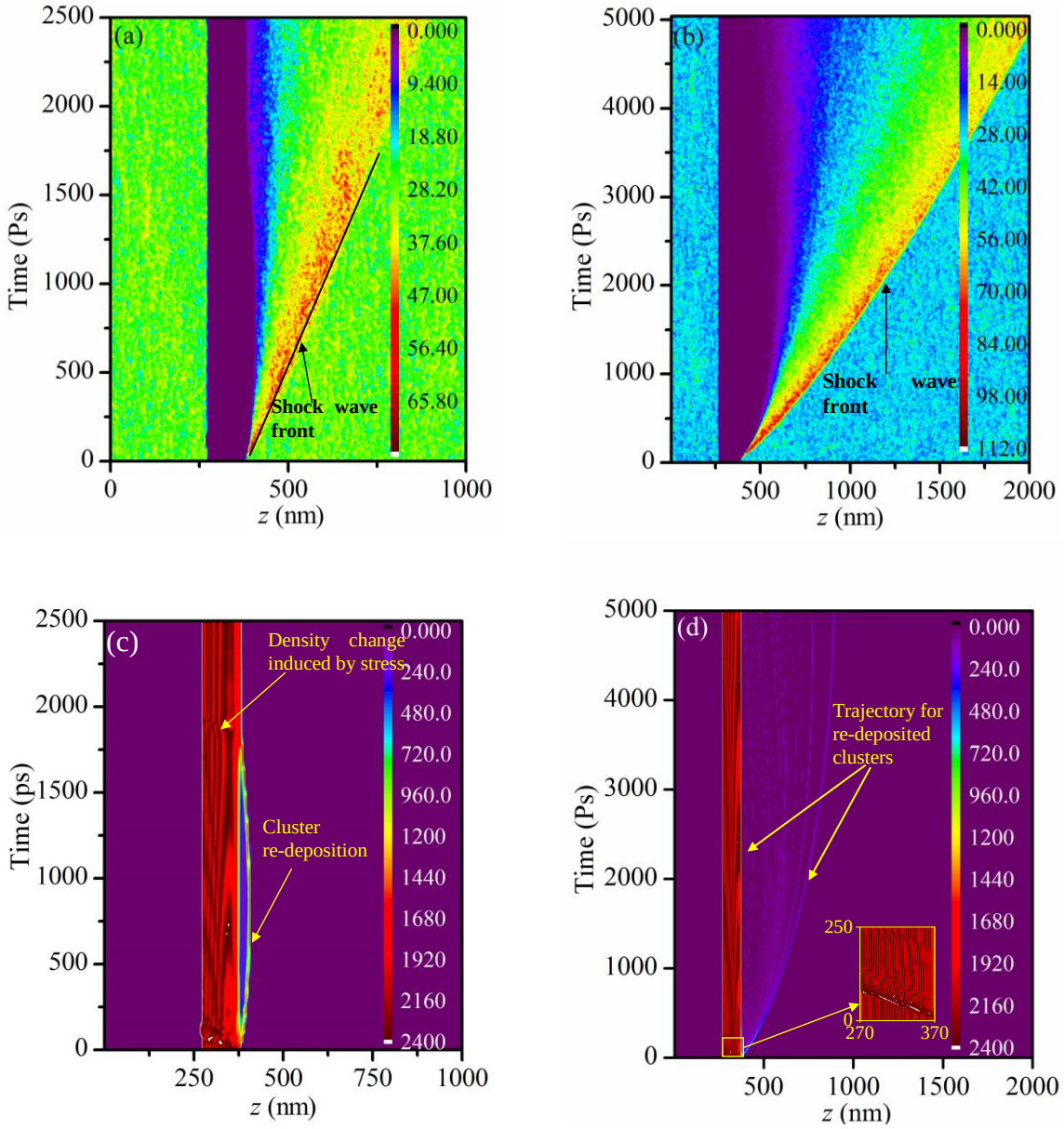

Fig. 2.6 Atom number contour: (a) gas number contour for E= 3 J/m^2, τ= 15nm; (b) gas number contour for E= 3 J/m^2, τ= 5nm; (c) target number contour, E= 3 J/m^2, τ= 15nm; (d) target number contour, E= 3 J/m^2, τ= 5nm. Stress waves can be told from the deformed twisted lines in the number contours, indicating the local density is changed by the local stress wave. The re-deposition in (c) leads to a secondary stress wave.

At the beginning, the ejected clusters characterize the maximum temperature. With the time going by, the temperature will go down because of the interaction of target atoms

with gas. In the corresponding part of the temperature contour, along the oblique line the temperature drops gradually, as shown in Figs. 2.5(a) and (b). Part of plume's translational kinetic energy is converted into its thermal energy. The temperature will go down with the rise of absorption depth. For E= 3 J/m^2, τ= 5 nm, the maximum temperature is 476 K, while with the same laser fluence and τ= 15 nm, the temperature of the target only goes to 154 K. The maximum temperature occurs near the end of laser irradiation.

Re-deposition is different for the two cases. For E= 3 J/m^2, τ= 15 nm, a large part of target atoms is pushed out while around 1.8 ns this part recombines with the rest of the target [Fig. 2.5(c)]. By contrast, with a shorter absorption depth, 5 nm, Fig. 2.5(d) shows that some of the targets are removed from the upper surface. The curves in Fig. 2.5(d) and Fig. 2.6(d) demonstrate the trajectories of the ejected atoms. From Fig. 2.6(d) we can observe that some of the ablated atoms/cluster already re-combine with the target within the 5 ns time while some of them will take a longer time to come back. Clusters flying out will decompose with time and slow down and finally re-deposit on the surface. When the atoms/cluster re-combine with the target, they will strike the target and could cause a strong secondary stress wave in the target. Such phenomenon will be discussed in detail in the next section.

2.2.4. Stress wave in the target under shock wave effect

Multiple stress waves are observed in our MD study. Laser induced stress wave consists of a strong compressive component and a weak tensile component. The interaction of compressive stress wave with the interface and the relief of compressive stress may account for the generation of the tensile component. Similar phenomenon and detailed

explanation can be seen in Wang's work [66] and Wang and Xu's work [67]. Stress wave during laser-material interaction has already been investigated intensively in a lot of literatures. The relationship between compressive stress, tensile stress and the laser fluence has been discussed before [15]. Effect of laser irradiation duration on the induced stress wave can also be found in the above work. In this work, the difference of the stress between situations with and without ambient gas is explored in detail.

The existence of gas does play a role in the phase change. However, as to the generation and propagation of stress wave, no big difference is distinguished. Stress is a main driving force behind the fracture formation during laser ablation. As to the generation of stress wave, it is believed to result from the direct laser energy absorption as well as recoil driving force from target atoms ejection [15]. Figures 2.7 and 2.8 show the stress wave generation and propagation for E= 3 J/m^2, τ= 5nm and τ= 15nm. The existence of ambient gas hampers the excited target atoms from expanding in the space and there are differences in the development of the molten regions. However, in all the plots of the two figures, no deviation is observed for stress with and without ambient gas. The momentum of the plume is significantly larger than the restraint force from the ambient gas. So no big difference is present here on the stress wave in the solid.

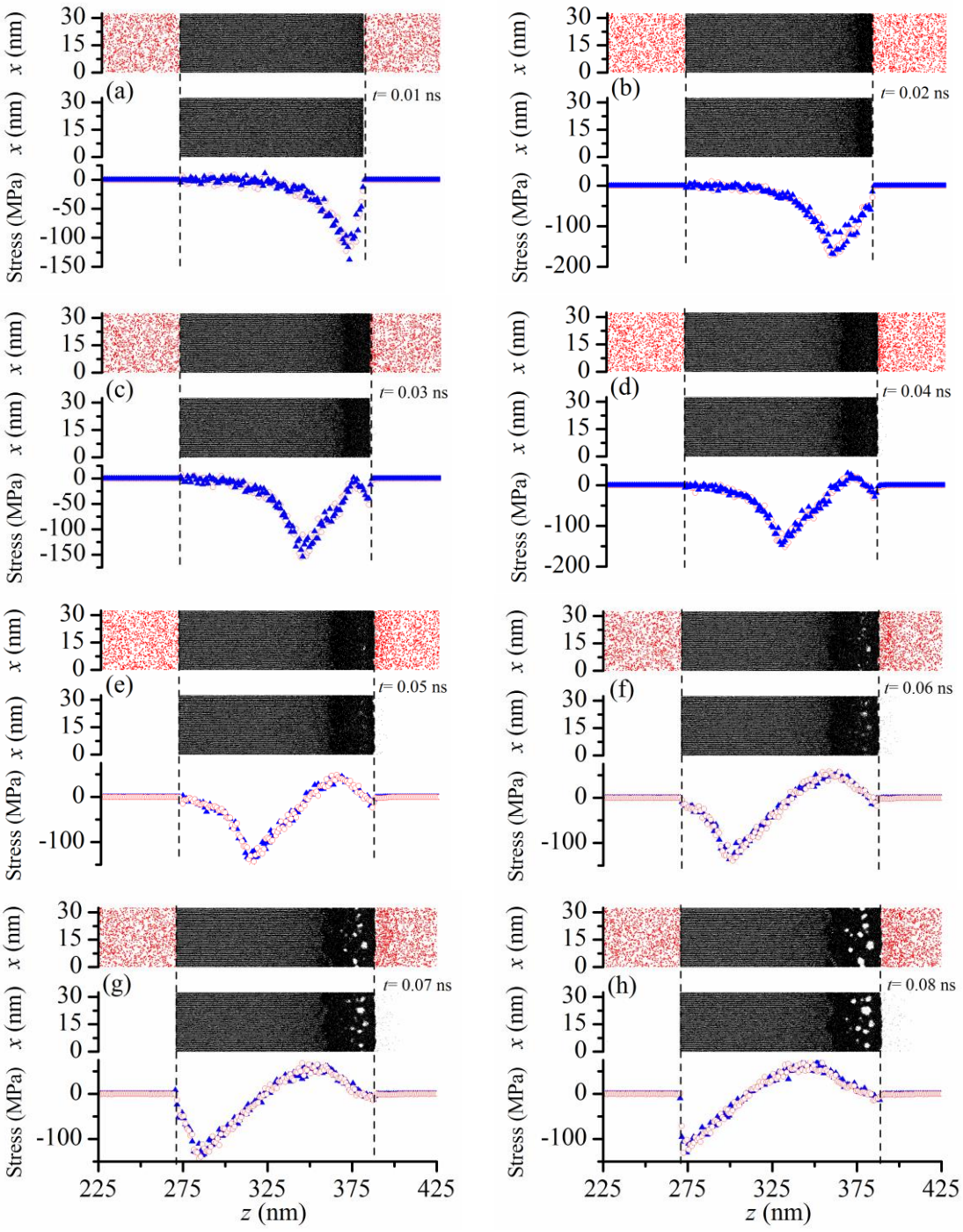

Fig. 2.7 Phase change and the stress wave for E= 3 J/m^2, τ= 15 nm. Two cases with and without ambient gas are compared here. The blue symbol is for case without ambient gas, and the red one is for the case with ambient gas. The negative stress peak is the maximum value of the compressive stress and the positive peak is for maximum tensile stress. No obvious difference for the stress wave is observed between gas and non-gas situations. To

help identify the relative position of the stress wave in the physical domain, the atomic configurations are also plotted. The red dots are for gas atoms, and the black dots are for target atoms.

Noticeably, from target atom number density [Figs. 2.6(c) and (d)] and temperature contours [Figs. 2.5(a) and (b)], stress wave within the target can also be told. Deformed fold lines in the target number density contours show the change of target density due to the local stress. Additionally, as marked in Fig. 2.5(a), the stress wave can also be detected by the change of temperature. The tensile stress will come along with a temperature decrease while compressive stress induces a temperature increase.

The reasons for the generation of the stress wave vary from each other. Laser-induced compressive stress appears first and then it is the tensile stress wave [Fig. 2.5 (d)]. The compressive and tensile components always accompany each other. The stress waves are not entirely gone at the bottom of the target. However, for the residual stress, the magnitude is very small and even negligible. Another relatively large stress wave is caused by re-deposition. Here we name it secondary stress wave and it is caused by collision of atoms/cluster with the target surface. In Fig. 2.5(c), the trajectory of re-deposited cluster is marked. In Fig. 2.5(c) and Fig. 2.6(c) the upper layer atoms are dragged back at 1.8 ns. Right after this we can see the stress wave in the stress contour or atom number density contour. Magnitude of this kind of secondary stress wave is much less than the stress wave directly induced by laser irradiation. For τ= 15 nm, the maximum stress value is approximately -140 MPa. In contrast, the maximum value of the secondary stress wave is only about -15 MPa.

We can see from the stress evolution figures [Fig. 2.7 and Fig. 2.8], when the absorption depth is 5 nm rather than 15 nm, there is a sharp drop in the stress wave front. The stress arises from energy absorption. The way how the energy is absorbed will directly affect the distribution of energy in the target. When the absorption depth is 5 nm, energy will damp quicker in space than the case of τ= 15 nm. For the region far away from the irradiation surface, the energy absorbed is too small to be considered. Then a sharp drop will be noticed in the stress wave front. Interestingly, In Fig. 2.8, there is one more peak compared to Fig. 2.7 which represents pressure in the flying-out part. This part has been marked in Fig. 2.8(c) for t= 0.03 ns. As the time going by, the peak is moving along the positive z direction.

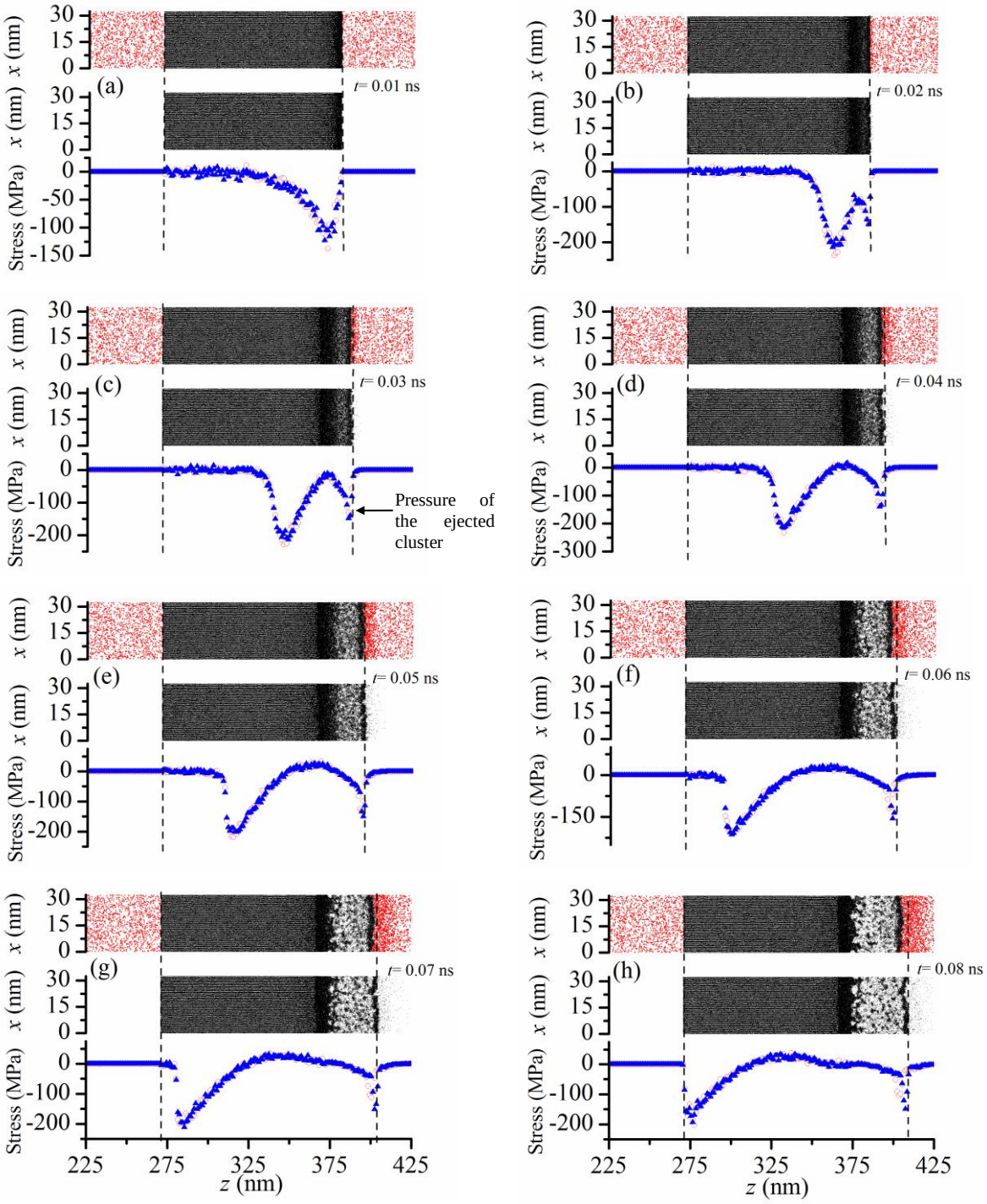

Fig. 2.8 Phase change and the stress wave generation and propagation for E= 3 J/m^2, τ= 5 nm. Two cases with and without ambient gas are compared here. The blue symbol is for case without ambient gas, and the red one is for the case with ambient gas. A sharp drop is observed in the stress wave front. This is the big difference induced by the absorption depth of τ= 5 nm to τ= 15 nm. To help identify the relative position of the stress wave in the physical domain, the atomic configurations are also plotted. The red dots are for gas toms, and the black dots are for target atoms.

Figure 2.9 shows the relationship between the magnitude of stress wave at 0.04 ns versus the laser energy. With the increase of the laser fluence, the magnitude of stress increases dramatically (almost linearly) [Fig. 2.9(b)]. In Fig. 2.9(a) all the laser energy is absorbed under the same absorption length τ= 15 nm. Three peaks are identified in the figure. From the right hand side, the first one represents the ejected clusters while the second and third one is the tensile and compressive components within target. A sharp drop is observed in the stress wave front for the stress wave propagation for lager laser fluences and the ejected clusters moves faster with the rise of the laser energy.

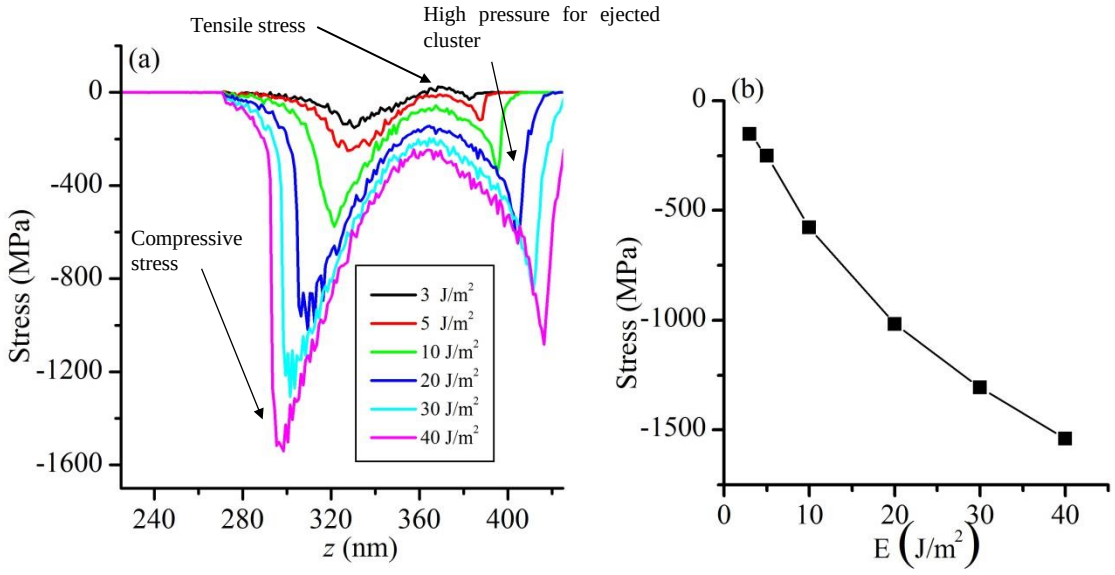

Fig. 2.9 Comparison of stress waves for different laser fluence: (a) the stress wave in the target at t= 0.04 ns and (b) the relationship between stress wave maximum value and the laser fluence. All the cases are run under the same gas environment.

CHAPTER 3. STRUCTURAL EVOLUTION OF NANOPARTICLES UNDER PICO-SECOND STRESS WAVE CONSOLIDATION

In this work, large-scale atomistic modeling is conducted to explore a relatively cold consolidation process: nanoparticles compressed by a stress wave from a sacrificial layer that is ablated by a picosecond laser. The temperature, stress, atomic configuration, and crystallinity are studied in detail to understand the structural behaviors under extreme compression. An orientation-radial distribution function (ODF) is designed to study the status of the nanocrystalline structure in detail. The methodology is detailed at first, then the results and discussion is presented.

3.1. Methodology

Argon is chosen as the material to be used in the simulation, due to its widely available potential, physical properties and significant computational cost reduction. Lennard-Jones potential (6-12 potential) is used to describe the interaction of atoms. For argon, the LJ potential well depth ε is 1.653×10^{-21} J and equilibrium separation parameter σ is 3.406 Å. The cut-off distance of the potential is 2.5 σ. Figure 3.1(a) shows the initial atomic configuration of the sacrificial layer and arrays of nanoparticles with a diameter of 10 nm. The whole physical domain measures $91.6\times33.5\times22$ nm^3 ($x\times y\times z$). The sacrificial layer is 13.8 nm along the x direction and 29.8 nm, 19.8 nm in the y and z direction. This sacrificial layer is used to absorb the laser energy. Under irradiation, this layer will quickly vaporize, generating a very strong plume moving against the nanoparticle region. Under the strong compression of this plume, the nanoparticles are expected to reconstruct. Arrays of nanoparticles occupy the space of $59.8\times31.4\times20$ nm^3. The gap between the sacrificial layer

and the top of the nanoparticles is approximately 15 nm to avoid the deformation of the sacrificial layer or nanoparticles resulting from their interaction. Nanoparticles of three different diameters (D =5 nm, 8 nm, 10 nm) are studied in this work.

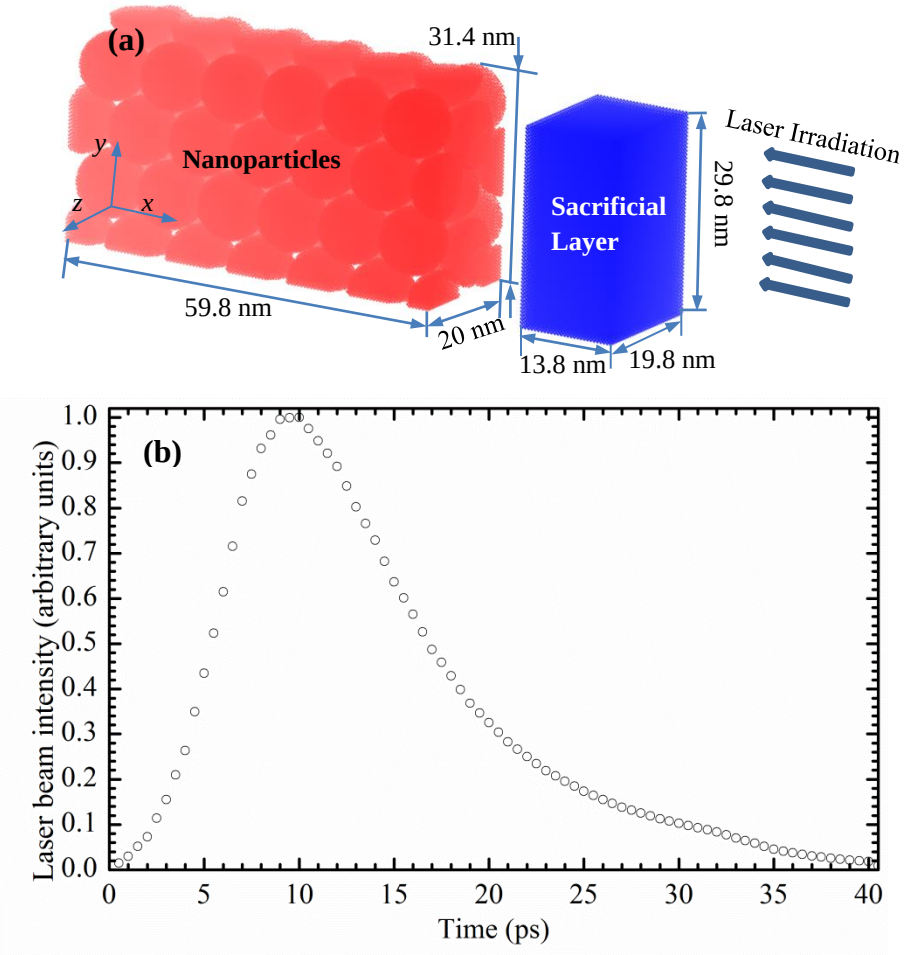

Fig. 3.1 (a) Schematic of the physical domain under simulation. The blue region is the sacrificial layer to absorb the laser energy, and the red region is argon nanoparticles (10 nm diameter) to be compressed (cold-sintered). The whole simulation box measures 91.6×33.5×22 nm^3 (x×y×z). The size of nanoparticle region is 59.8×31.4×20 nm^3 (x×y×z). The size of the sacrificial layer is 13.8×29.8×19.8 nm^3 (x×y×z). The gap between the sacrificial layer and nanoparticles is approximately 15 nm. A potential wall boundary is applied to the six walls of the simulation box. Laser irradiation is applied in the negative x direction. (b) Temporal profile of the picosecond laser pulse used in the simulation. The FWHM of the pulse is 11.5 ps, and the peak is located at 9 ps.

The arrangement of nanoparticles is similar to the hexagonal close packed (HCP) crystal structure. Each nanoparticle of diameter *D* occupies one point of the HCP structure and the nanoparticles are tangential to the nearest neighbors. All the particles follow the same crystographical orientation in the initial structure. This eases our study and analysis of the crystalline destruction by the consolidation process. To constrain the movement of atoms, wall potential (wall/LJ93) is implemented in the six boundaries. The strength factor ε for wall-particle interaction is 1.653×10^{-21} J and the size factor σ is 3.615 Å in this work. 8.515 Å is chosen as the cutoff distance for the wall boundary. 5 fs is chosen as the time step for the simulation. First, the whole system is thermostated at temperature T= 50 K for 4 ns as a canonical (NVT) ensemble. Then the system is run as a microcanonical (NVE) ensemble for 500 ps to damp the disturbance introduced to the system during the NVT calculation. The thermal equilibrium is confirmed to be reached after the 500 ps NVE run.

Laser energy with a temporal distribution as seen in Fig. 3.1(b) irradiates the sacrificial layer surface afterwards. The full width at half maximum (FWHM) of the incident laser beam intensity distribution is 11.5 ps and peaked at 9 ps. The laser energy comes in the negative *x* direction. Laser energy is absorbed volumetrically in the sacrificial layer and the absorption process obeys the Beer-Lambert law. In the simulation, the laser energy is absorbed in the layer-by-layer way and it is only absorbed by the sacrificial layer.

3.2. Results and Discussion

The general picture of the compression is presented at first. Then the structure evolution under the compression process is investigated. Particle size and laser fluence is

varied to discuss the effect on the compression process. Finally, orientation-radial distribution function (ODF) is introduced for the first time to describe the structure state.

3.2.1. Temperature and stress distribution and evolution during compressing

In nanoparticle consolidation, temperature and stress are two critical factors that influence the structure evolution. First of all, we show pictures to illustrate how the nanoparticles are compressed by the strong stress wave from the sacrificial layer. Then the temperature and stress are studied. Figure 3.2 shows the general picture of the consolidation process for case D= 10 nm, E= 2.7 mJ/cm^2. To have a clear view, a slab ranging from z= 9 nm- 9.5 nm was taken out to generate the atomic snapshots. In the beginning, the laser energy is absorbed by the sacrificial layer. Then the sacrificial layer begins to melt under the laser irradiation. Due to the constraint of the top and side potential walls, the sacrificial layer is pushed towards the top surface of nanoparticles. This is shown in Fig. 3.2 at t= 40 ps. 65 picoseconds after laser irradiation, the sacrificial layer is in touch with the nanoparticles. Afterwards, the nanoparticles start to be compressed and crushed from the top to bottom gradually. The sacrificial-layer atoms concentrate on the top surface of the nanoparticles and very few atoms is observed to be embedded in the nanoparticle array. Finally, nanoparticles are deformed into amorphous/nanocrystalline (termed “destructed” structure in this work) state as that shown at t= 300 ps in Fig. 3.2.

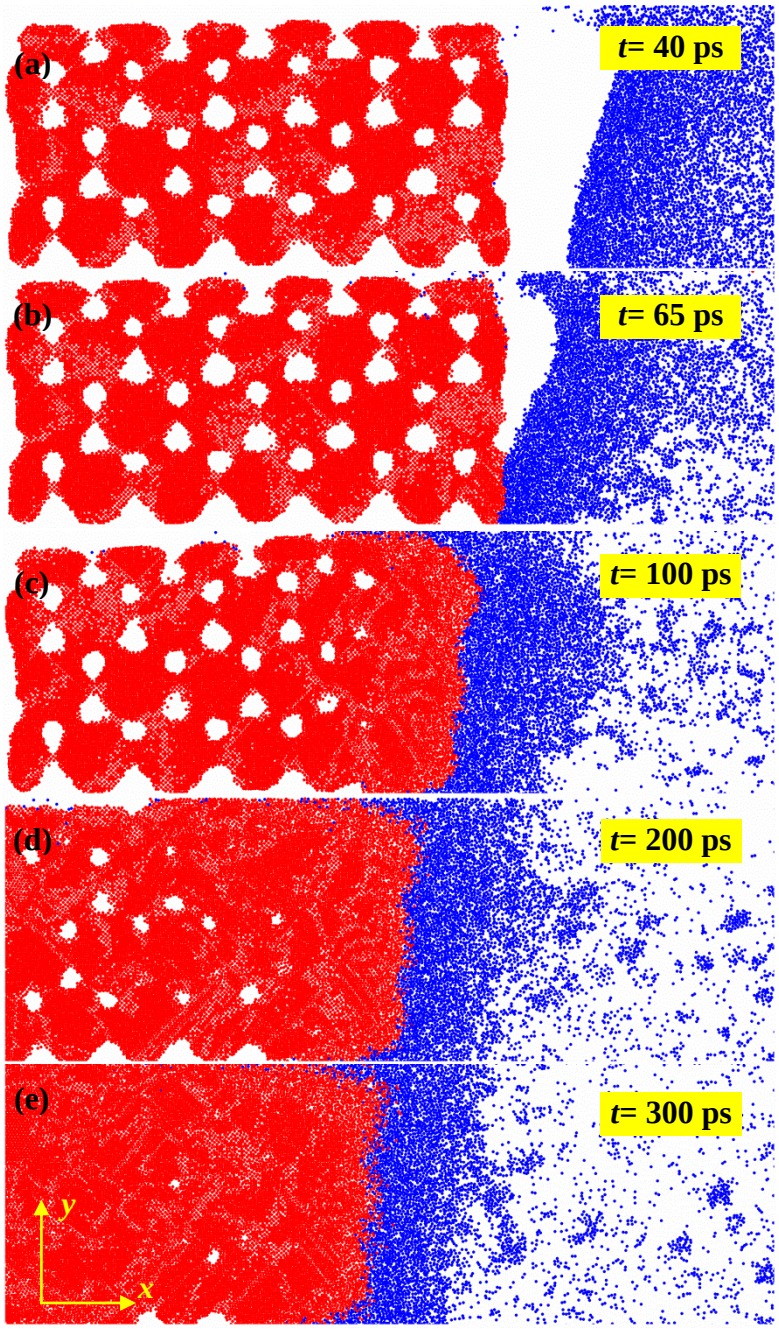

Fig. 3.2 Snapshots for compressing of nanoparticles with D= 10 nm. The laser fluence is E= 2.7 mJ/cm^2. From t= 40 ps to 65 ps, the sacrificial layer melts and is pushed down towards the top of nanoparticles. At t= 100 ps to 300 ps, the nanoparticles are compressed. At the end of 300 ps, the nanoparticles are almost destructed completely.

Temperature and stress contours are plotted to explore their distribution and evolution during the compressing process. Figure 3.3(a) and (b) show the temperature and stress contours for the case illustrated in Fig. 3.2. Before the consolidation starts, nanoparticles are in a state of equilibrium and the temperature is uniform around 50K as shown at the initial moments in Fig. 3.3(a). As time progresses, the consolidation process is accompanied by a quick temperature rise. Heat is transferred from the high-temperature sacrificial layer to the nanoparticles array. And it contributes to the fast collapse of the nanoparticles. Noticeably, a high temperature is supposed to be transferred from the top surface to the bottom in the consolidation process. However, as shown in Fig. 3.3(a), instead of straight slope line, the temperature contour line is shown with a hump as marked in Fig. 3.3(a). This means there is heat transferred from the bottom towards the inside. Since the bottom is fixed with the potential wall, the compression near the bottom surface accounts for the temperature rise. This can also be validated by the spots of the high compression force shown in Fig. 3.3(b). As a consequence, the temperature of the bottom part close to the potential wall is a little bit higher than that in the middle part. In general, the high temperature will go down gradually with the consolidation process. In Fig. 3.3(a), the large green region of the material after about 250 ps is around 67K, lower than the melting point of Argon: 83.8K. Considering the high pressure existing in the material, the melting point should be even higher than 83.8K. This indicates that under the rapid pressure consolidation induced by the stress wave, the argon nanoparticles experience structure damage and reconstruction, rather than melting and solidification.

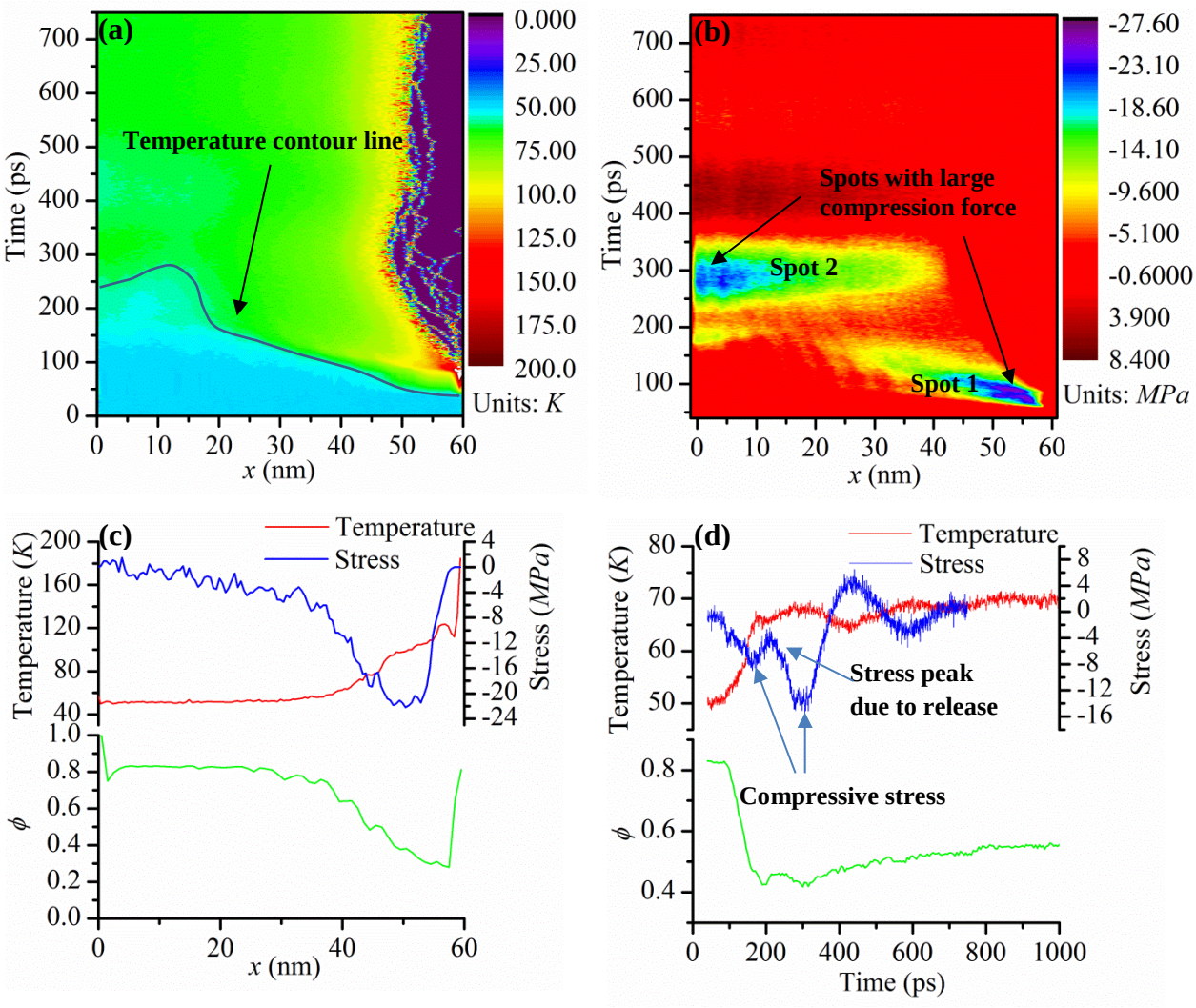

Fig. 3.3 (a) Spatiotemporal temperature distribution for nanoparticles with D= 10 nm during laser-induced stress wave consolidation (E= 2.7 mJ/cm^2). A temperature contour line is given for the convenience of telling the change of temperature for different parts of nanoparticles with time. (b) Stress contour for the case D= 10 nm, E= 2.7 mJ/cm^2. The stress refers to the normal stress and is calculated as $\sigma = (\sigma_{xx} + \sigma_{yy} + \sigma_{zz})/3$. Two spots with large compression force are pointed out. Spot 1 is due to the compression of sacrificial layer and spot 2 results from the constraint of the bottom potential wall. (c) Temperature, stress, crystallinity against location x at time t= 100 ps. The stress peak is accompanied by a sharp drop of crystallinity afterwards. (d) Temperature, stress, crystallinity against time at location x= 25.35 nm.

Figure 3.3(b) is the stress contour of nanoparticles in the consolidation process. The stress refers to the normal stress and is calculated as $\sigma = (\sigma_{xx} + \sigma_{yy} + \sigma_{zz})/3$. Similar to the

temperature distribution, the compressive stress will move from the top surface to the bottom quickly, but also experiences damping. Before t= 45 ps, no obvious compressive stress is observed. Afterwards, around t= 70 ps, the first spot (Spot 1) under big compression force shows up. This is exactly the time when the sacrificial layer touches the nanoparticles and starts to compress them. Part of the compressive stress is released by the structure collapse of the top nanoparticles. However, part of the compressive stress manages to go deep down into the nanoparticles arrays. Interestingly, another big compression spot (Spot 2) appears around the time t= 275 ps. This is induced by the compression at the bottom. Finally, at approximately t= 325 ps, the particle structure is completely destroyed and the compressive stress begins to be released from that time.

The crystal structure is a key criterion to judge the state of nanoparticles at atomic level. And crystallinity is the index to show that the particles are close to the perfect crystal state or away from the perfect crystal structure. In this work, crystallinity is defined as [68, 69]

$$\phi(r_{i,x}) = \frac{1}{N} \left| \sum_i e^{j2\pi(2r_{i,x}/\lambda)} \right|, \tag{6}$$

where $r_{i,x}$ is the x coordinate of atom i and λ is the light wavelength for crystallinity characterization. Here we assign λ with the value of the lattice constant a= 5.414 Å. $2r_{i,x}$ is the light travel distance from x= 0 and then comes back. If atoms are regularly distributed in space with their spacing in the x direction equal to $n(a/2)$, the function will be equal to 1. In the amorphous state, the function $\phi(r_{i,x})$ will be much less than 1, in fact very small (close to zero). The nanoparticles are divided along the x direction into layers with Δx= 10 Å. Each

layer is then divided into cubes of 10 Å size, and the crystallinity of each cube is calculated. The crystallinity of each layer is the average of the crystallinity of all the cubes in it.

Figure 3.3(c) is the temperature, stress and crystallinity at time t= 100 ps. Figure 3.3(d) is the temperature, stress and crystallinity evolution at x= 25.35 nm against time. In Figs. 3.3(c) and (d), it can be seen that when the stress wave passes by, the crystallinity drops dramatically. This strongly confirms the structure damage by the high compressive stress. The high temperature moves from the top surface to the bottom nanoparticles. Because of the high laser fluence (E= 2.7 mJ/cm^2) in this case, the atoms around x= 25.35 nm experience a sudden temperature rise around t= 180 ps and then stay at the plateau value of T= 67 K [shown in Fig. 3.3(d)]. The stress evolution in Fig. 3.3(d) shows the nanoparticles around x= 25.35 nm are compressed from t= 77 ps to 380 ps, which peaks at t= 300 ps. At 300 ps, the compressive stress reaches the highest level, explaining why the crystallinity is the worst at that moment. In Fig. 3.3(d), the temperature rise around 180 ps releases part of the compressive stress which is shown as a small peak in Fig. 3.3(d). It is obvious that the crystallinity drops following the compressive stress. This reveals the close relationship between the compression force and the structure destruction.

3.2.2. Structure evolution during nanoparticle compression

As mentioned above, the crystallinity's value strongly reflects the structure of the material: a value close to 1 indicating crystalline structure close to the original one (we call this the "retained" structure), and a low value meaning destructed structure or severe structure damage. Note this "destructed" structure could mean either amorphous, or the lattice is strongly twisted from the original orientation. Figure 3.4(a) shows the contour of the crystallinity of the nanoparticles for the case discussed in Fig. 3.3. There is a black line marked as crystallinity drop line in this figure. Below the black line, the crystallinity is very close to 1 which means sound crystalline structure. Above the crystallinity drop line ϕ is dropped to around 0.5. It should be noted that the crystallinity contour above 50 nm (x> 50 nm) at the late stage ($t\geq$ 100 ps) is not reliable when the nanoparticles are compressed, since there may be one or just a few atoms in some layers above 50 nm. Noticeably, the compression force from the potential walls also contributes to the destruction of the structure of the nanoparticles at the bottom. As marked in Fig. 3.4(a), directly above the crystallinity drop line, the constraint from the potential walls plays an important role in destroying the structure completely. The effect of potential walls is also obvious when it comes to the cases with less laser fluence as shown in Fig. 3.4(b) and Fig. 3.4(c).

Figure 3.4(b) is the crystallinity contour for the case D= 10 nm, E= 2.0 mJ/cm^2. In contrast with Fig. 3.4(a), the crystallinity drop line in Fig. 3.4(b) is in a hump shape. The crystallinity is below 0.5 at the bottom part around t= 300 ps. However, in the middle part ranging from x= 16 nm to 22 nm, the average crystallinity is above 0.6. The case D= 10 nm, E= 1.5 mJ/cm^2 has this similar observation, too [Fig. 3.4(c)]. In Fig. 3.4(c), although the

crystallinity of nanoparticles at the bottom is above 0.5, the crystallinity in the range *x*= 16-30 nm is apparently higher than the bottom part, which means the middle part of the crystal structure is more well preserved than the bottom nanoparticles. So it is conclusive that the compression in the bottom part plays a critical role in damaging the particles close to the bottom.

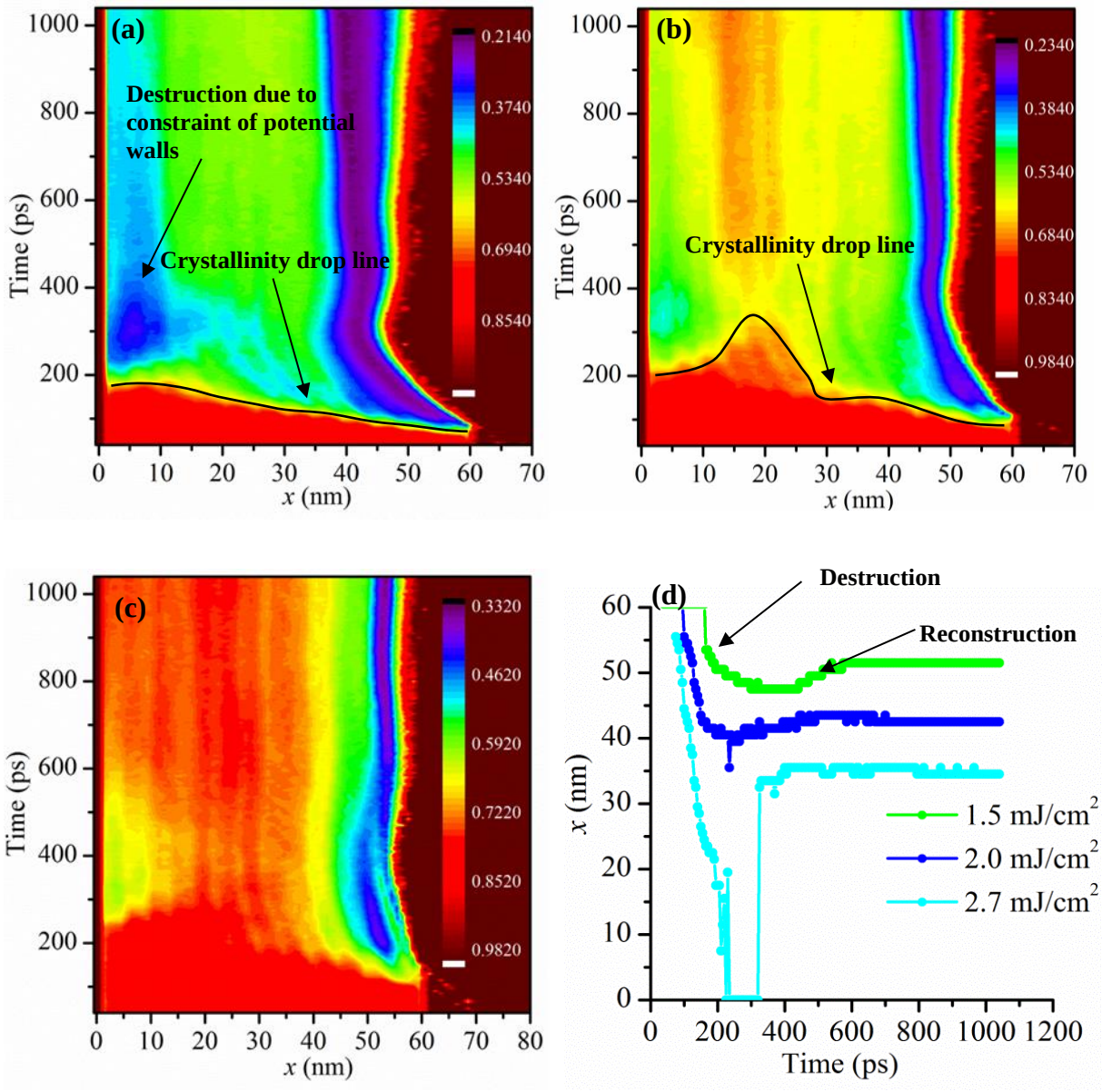

Fig. 3.4 Spatiotemporal contour of structure crystallinity for argon nanoparticles of *D*= 10 nm under compressing by laser fluence of (a) 2.7 mJ/cm^2, (b) 2.0 mJ/cm^2, and (c) 1.5

mJ/cm^2. In figs. (a) and (b), the crystallinity drop line is quite distinguishable and is marked using a solid curve. Below the line, the crystallinity ϕ is approximately 1, while above the line ϕ is around 0.5. (d) Retained-destructed interface evolution against time. For E= 2.7 mJ/cm^2, the interface goes down quickly because the nanoparticles are completely destroyed. After that the reconstruction process occurs. For E= 2.0 mJ/cm^2 and E= 1.5 mJ/cm^2, only part of the nanoparticles are completely destroyed. After the reconstruction, the interface will be stable at x= 42 nm and x= 52 nm, respectively.

Figure 3.4(d) shows the retained-destructed structure interface which is identified by the crystallinity ϕ of each layer. Comparing Fig. 3.3(a) and Fig. 3.4(a), along the crystallinity drop line, the temperature of the nanoparticles are still well-below the melting point. So the process is more like stress-induced structure change rather than a melting procedure. If ϕ of a layer is less than 0.5, it is defined as the destructed region in this work. Otherwise it is viewed as the retained part. Interestingly, for the case D= 10 nm, E= 2.7 mJ/cm^2, the top, middle and bottom parts are initially crushed into a destructed state. On the other hand, after time t= 400 ps, the crystallinity goes back to being above 0.5 for the middle part. As a result, two retained-destructed interfaces show up along the time. Figure 3.4(d) plots the retained-destructed interface that is closer to the top surface. Until this point, we can draw a conclusion that nanoparticle consolidation consists of two processes: plastic and elastic. The plastic compressing gives a permanent final amorphous/nanocrystalline structure. The elastic compressing is responsible for the temporary structure damage, and such damage will disappear after the stress wave is released. Such temporary structure damage has been observed in our past work on laser-material interaction that involves melting and solidification [25, 68].

The crushing process does not generate enough heat that makes temperature of all the nanoparticle atoms rise above the melting point T_m= 83.85K. As in the case where D= 10 nm, E= 2.7 mJ/cm^2, the temperature in the middle part is around 65K. As a result, the observed crystalline reconstruction after consolidation is not re-solidification. As shown in Fig. 3.4(d), the retained-destructed interface for the three cases all experience processes that involve damage moving deep down towards the bottom at first and then coming back towards the top surface (crystalline reconstruction) and finally staying in a plateau value. The dropping down part is the structure damaging process and the rising part represents the reconstruction process. The nanoparticles are completely destroyed so the retained-destructed interface will decrease dramatically and finally vanishes for the case D= 10 nm, E= 2.7 mJ/cm^2. After that, at approximately t= 320 ps, reconstruction begins from the middle part (x= 32 nm) of the crystalline region. The crystalline part will then expand. For cases D= 10 nm, E= 2.0 mJ/cm^2 and D= 10 nm, E= 1.5 mJ/cm, the crystalline reconstruction is observed from t= 200-600 ps and not all the nanoparticles are crushed down into destructed states in these two cases.

3.2.3. Effect of particle size and laser energy

The above discussed nanoparticle consolidation process is for particles of 10 nm diameter. It is expected that the process itself could vary a lot if particles of different sizes are present. Here the size of nanoparticles is varied to study the size effect. We use another two different particle sizes: D= 5 nm and 8 nm. Figures 3.5 (a) and (b) are the crystallinity contour for cases D= 5 nm and D= 8 nm with the same laser fluence, E= 2.7 mJ/cm^2. This structure contour is intended to explore how the structure evolves during stress wave consolidation. For size D= 5 nm, the bottom nanoparticles are pushed back towards the top

surface at t= 400 ps. For size D= 8 nm, this happens at t= 460 ps. However, no pushing-back is observed for nanoparticles of size D= 10 nm. During the particle consolidation process, a shear stress can be easily established at the particle-particle contact region. When the diameter of the nanoparticles decreases, the number of nanoparticles will increase for the same volume under study. Specifically, the arrangement of nanoparticles of size D= 5 nm indicates that there is more shear stress in the contact part of the nanoparticles (due to the dramatically increased surface-to-volume ratio). Compared with D= 10 nm and D= 8 nm, much less energy is needed for destruction and the extra energy will give rise to the pushing back process in the case of D= 5 nm. As shown in Fig. 3.5(a) and Fig. 3.5(b), for D= 5 nm, the crystallinity value drops more quickly and the average crystallinity is obviously lower than D= 8 nm. In addition, it is also found that the downward movement velocity for case D= 5 nm dissipates slower than the cases D= 8 nm and D= 10 nm. Finally, the pushing back process occurs earlier for the case D= 5 nm, E= 2.7 mJ/cm^2.

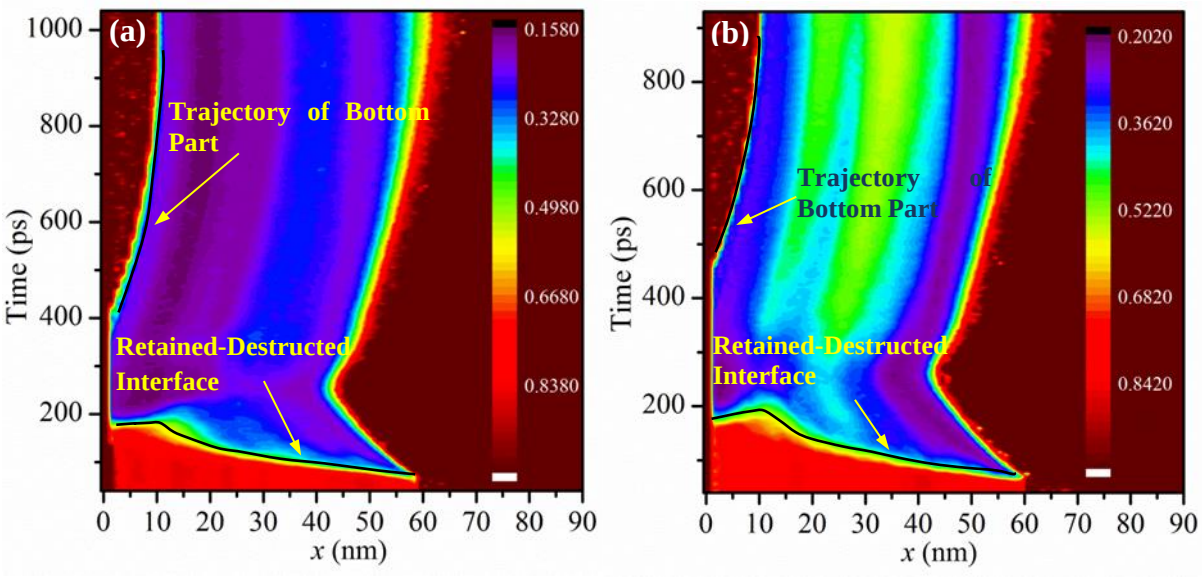

Fig. 3.5 Spatiotemporal contour of crystallinity for nanoparticles of different sizes: (a) D= 5 nm under laser fluence of 2.7 mJ/cm^2. (b) D= 8 nm under laser fluence of 2.7 mJ/cm^2. In both cases, the bottom parts of the nanoparticles are pushed back by the wall towards the top

surface, as indicated by the trajectory of the bottom part in the figure. This is obvious by comparison between Fig. 3.4(a) and figs. (a) and (b) in this figure. It is shown that when the particle size is bigger, this push-back effect becomes weaker.

A specific moment t= 1.04 ns (the final stage of our simulation) is chosen for the comparison of atomic snapshots and is shown in Figs. 3.6(a)-(e). This comparison will help reveal how the final material structure looks and how it is affected by the particle size and laser energy. Figures 3.6(a)-(c) are for comparison to explore the particle size effect, and Figs. 3.6(c)-(e) show the effect of laser fluence for the cases of D= 10 nm. Comparing Figs. 3.6(a)-(c), we can conclude that a smaller particle size is more favorable for the compression destruction because of more contact surface among particles and more accumulation of shear stress as discussed above. Structure defects due to the atomic dislocation are marked in Figs. 3.6(a). These defects follow an angle of about 45 degrees with respect to the laser incident direction. It is in this direction (45°) that the maximum shear stress exists, and this stress causes the structural defect. It also has been observed that the defect line is 45 ° with respect to the laser irradiation direction in our previous work [25, 68]. The corresponding crystallinity (ϕ) contours are plotted in Figs. 3.6(f)-(j) for the convenience of comparison and analysis.

Small-size nanoparticles are easily crushed into the destructed state as shown by Figs. 3.6(f)-(h). The smaller the particles are, the lower the average crystallinity is. And the high laser fluence also contributes to the destruction of nanoparticles. A higher laser fluence leads to more deformation of nanoparticles. Figures 3.6(h)-(j) are for the same particle size, but with different laser fluence. The sacrificial layer gains more energy in the higher laser

fluence situation. The downward momentum is much stronger and finally results in the more serious collapse process of nanoparticles. Comparison between Figs. 3.6(h)-(j) shows that when the laser fluence is smaller, the nanoparticles cannot be compressed tightly to form a fully dense structure. At the nanoparticles arrangement level, voids/pores do exist in the final structure although the nanoparticles are closely connected [Fig. 3.6(e)]. For the solid region, great crystallinity is preserved during consolidation, as indicated in Fig. 3.6(h)-(j).

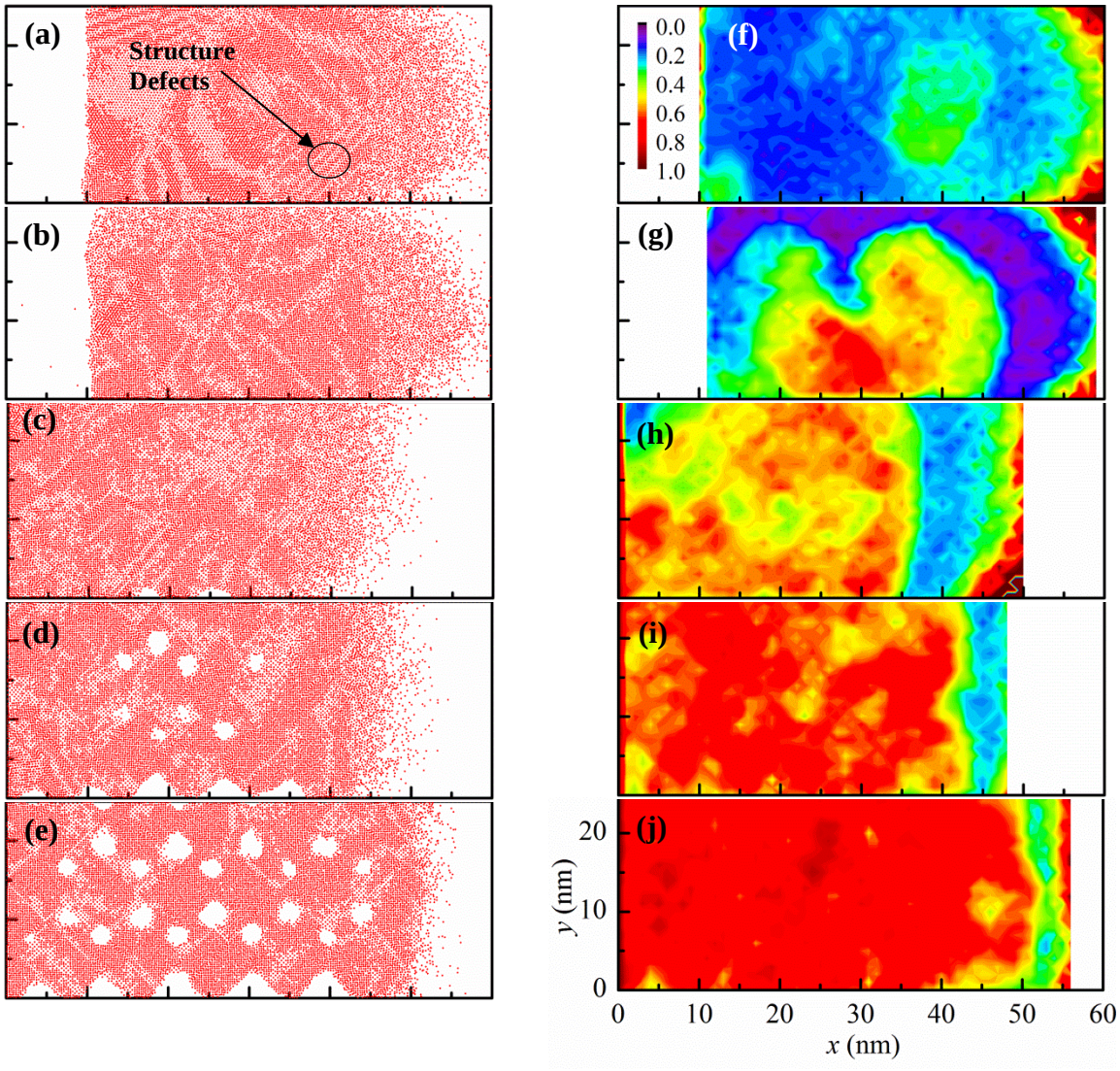

Fig. 3.6 Atomic configuration and contour of the crystallinity function at t= 1.04 ns to illustrate the effect of particle size and laser fluence. The y axis ranges from 0 to 25 nm. The x axis is from 0 to 60 nm. The simulation box size is a little bit different for cases with

different particle diameters. For the cases with D= 10 nm, the simulation box is $91.6 \times 33.5 \times 22$ nm^3 ($x \times y \times z$) while for the cases with D= 5 nm (with 783419 atoms) and D= 8 nm (with 763760 atoms), the simulation box is $92 \times 26.6 \times 23.6$ nm^3 ($x \times y \times z$). Only atoms between z= 9-9.5 nm are plotted in the figures. (a) D= 5 nm, E= 2.7 mJ/cm^2; (b) D= 8 nm, E= 2.7 mJ/cm^2; (c) D= 10 nm, E= 2.7 mJ/cm^2; (d) D= 10 nm, E= 2.0 mJ/cm^2; (e) D= 10 nm, E= 1.5 mJ/cm^2. The final structure position of the case D=5 and 8 nm is a little bit to the right of the wall due to the bouncing-back movement described in the text. For ϕ calculation, the simulation box is divided in the x and y direction with a size of 1 nm. Then the cube volume of the cases D= 5 nm and D= 8 nm is $1 \times 1 \times 23.6$ nm^3 and is $1 \times 1 \times 22$ nm^3 for cases D= 10 nm. (f) D= 5 nm, E= 2.7 mJ/cm^2; (g) D= 8 nm, E= 2.7 mJ/cm^2; (h) D= 10 nm, E= 2.7 mJ/cm^2; (i) D= 10 nm, E= 2.0 mJ/cm^2; (j) D= 10 nm, E= 1.5 mJ/cm^2.

3.2.4. Nanocrystalline structure after consolidation

Even though the crystallinity function shows how badly the crystal structure is destructed, we do not know whether the crystal is partially amorphous or just orientationally twisted. For smaller particles, during consolidation, they are easily twisted and are ready to change the crystallographic orientation to accommodate the impact from the stress. Therefore, the final structure could be more nanocrystalline-like with significant crystallographic orientation variation in space. And we believe this gives a smaller crystallinity function value as shown in Fig. 3.6(f). When the particles become larger, they are reluctant to be twisted and could retain some original crystallographic orientation. Therefore, a higher value of the crystallinity function is observed in Fig. 3.6(h). To confirm this explanation, an orientation-radial distribution function (ODF) is developed in this work for the first time. Similar to the radial distribution function (RDF), ODF reveals the atom density distribution as a function of the distance to the reference atom in the 3D space. Furthermore, it provides the angle information which is missing in RDF: the relative direction of the atoms to the reference one. The Euler angles show us the 3D space orientational arrangement of structure. The angle information in the x-y plane is good enough

to demonstrate how severely the structure is twisted in space at atomic level in this work. To simplify the calculation work, only angle information in the *x*-*y* plane is discussed here. The angle is defined with respect to the *x* axis and it is designated to be in the range 0˚ to 180˚.

For simplicity, only the atom number is used for the analysis. Figure 3.7(a) is the 3D image of the face-centered cubic (fcc) structure and Fig. 3.7(b) is the structure projection in the *x*-*y* plane. In this fcc crystal cell, atom 2, 3, 4 are the 1st order nearest atoms to atom 1 as shown in Fig. 3.7(a). In our ODF computation, the atomic distance is obtained from the 3D space, while the angle is calculated with all the atoms projected to the 2D plane (*x*-*y* plane). As shown in Fig. 3.7(b) the angles to the *x* axis are 0˚, 45˚, 90˚ for the nearest distance atoms. Since the unit cell is repeated along the *x* and *y* axis and the angle in ODF is defined in [0˚, 180˚], the angles for the 1st order nearest atom distance are 0˚, 45˚, 90˚, 135˚ and 180˚ in ideal situations. Figure 3.7(c) is the atom number variation as a function of the distance in different ODF angles. At Φ= 0˚, the first peak is 3.83 Å. The second peak is 5.41 Å. Interestingly, since the atom-atom connection line of length 6.63 Å cannot be projected paralell to the *x* axis in the *x*-*y* plane, so there is no peak in 6.63 Å. Then the third peak is 7.76 Å. The RDF can only give us the radial distribution information as shown in Fig. 3.7(c). However, the ODF includes the informaton about the atom density variation in different angles, and gives twisting details as shown in Fig. 3.8. In this work, in the ODF(*r*, Φ), *r* refers to the atom-atom distance in 3D space while Φ is the angle projection of the atom-atom connection in the *x*-*y* plane.

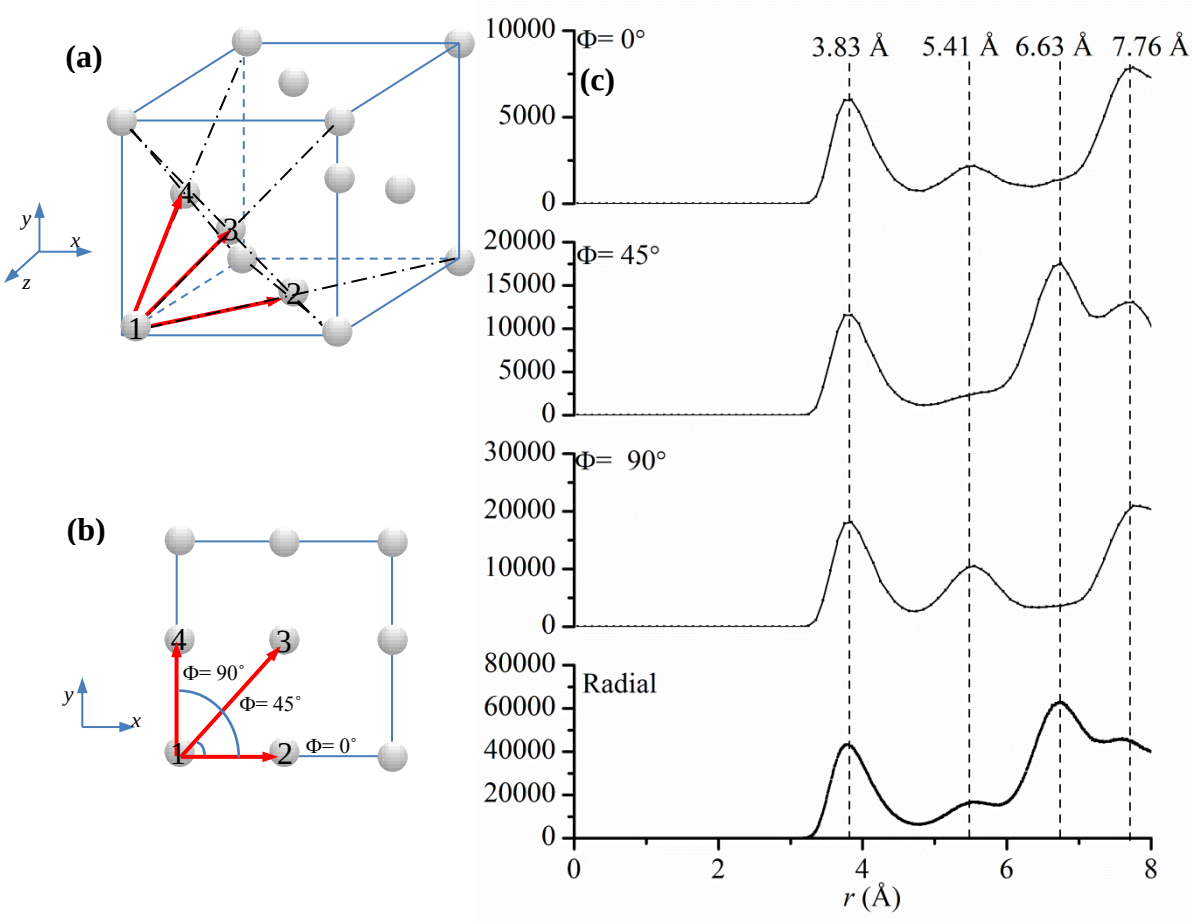

Fig. 3.7 (a) The structure of fcc crystal in 3D space. The 1st order nearest atoms to atom 1 are atom 2, 3 and 4. The 1st nearest distance is 3.83 Å; (b) The projection of fcc struture in the *x*-*y* plane. The angles are 0˚, 45˚, 90˚. The unit cell is extended along the *x* and *y* axis. So the angles are 0˚, 45˚, 90˚, 135˚, 180˚; (c) Atom number variation with atomic distance. The *y* axis is the atom number within every 0.1 Å spacing along Φ= 0˚, 45˚, 90˚ and 0.00852 Å for radial (RDF).

Figure 3.8 is the atom ODF polar contour. Before the laser energy is applied, the ODF of the 5 cases is similar to each other as shown by Figs. 3.8(a), (c), (e). The spots with a larger atom number are distributed at certain radii which correspond to the 1st-4th nearest atom distance (3.83 Å, 5.41 Å, 6.63 Å, 7.76 Å). Furthermore, the speckles in Figs. 3.8(a), (c), (e) are well located around certain angles. This proves that the structure at the initial state is

very close to the perfect crystal structure. However, the ODF of the final state of the 5 cases differs a lot. Figures 3.8(b), (d), (f) share the same laser fluence (E= 2.7 mJ/cm^2), but their particle size varies. For the case with a smaller particle size, like Figs. 3.8(b) (D= 5 nm), the distribution contour in the 1st, 2nd, 3rd and 4th nearest atomic distance is blur. Furthermore, the angle range in the above distance is broad. The angle in the 1st nearest distance is twisted. The angle should be in 0˚, 45˚, 90˚, 135˚, 180˚ for non-twisted crystal. However, in Figs. 3.8(b), the angle is 0˚, 60˚, 120˚, 180˚. Since the shear stress in the angle 45˚ and 135˚ is the largest one, materials are more likely to be twisted to other angles. For a large particle size, like Fig. 3.8(f) (D= 10 nm), the distribution contour is much clearer. At the 1st nearest atomic distance, the angles are well located in 0˚, 45˚, 90˚, 135˚, 180˚. For the case D= 8 nm, E= 2.7 mJ/cm^2, the distribution contour is blur but well located at the corresponding angles. We can conclude its destruction level should be between the case D= 5 nm, E= 2.7 mJ/cm^2 and the case D= 10 nm, E= 2.7 mJ/cm^2.

Figures 3.8 (f), (g), (h) demonstrate the effect of laser fluence. They are all for the same size of particles: D= 10 nm. For the case with a less laser fluence (D= 10 nm, E= 1.5 mJ/cm^2), the atom distribution in 1st-4th nearest distance is well located around the corresponding angle. The contour is much clearer than the case with D= 10 nm, E= 2.7 mJ/cm^2 and the angle distribution is less broad.

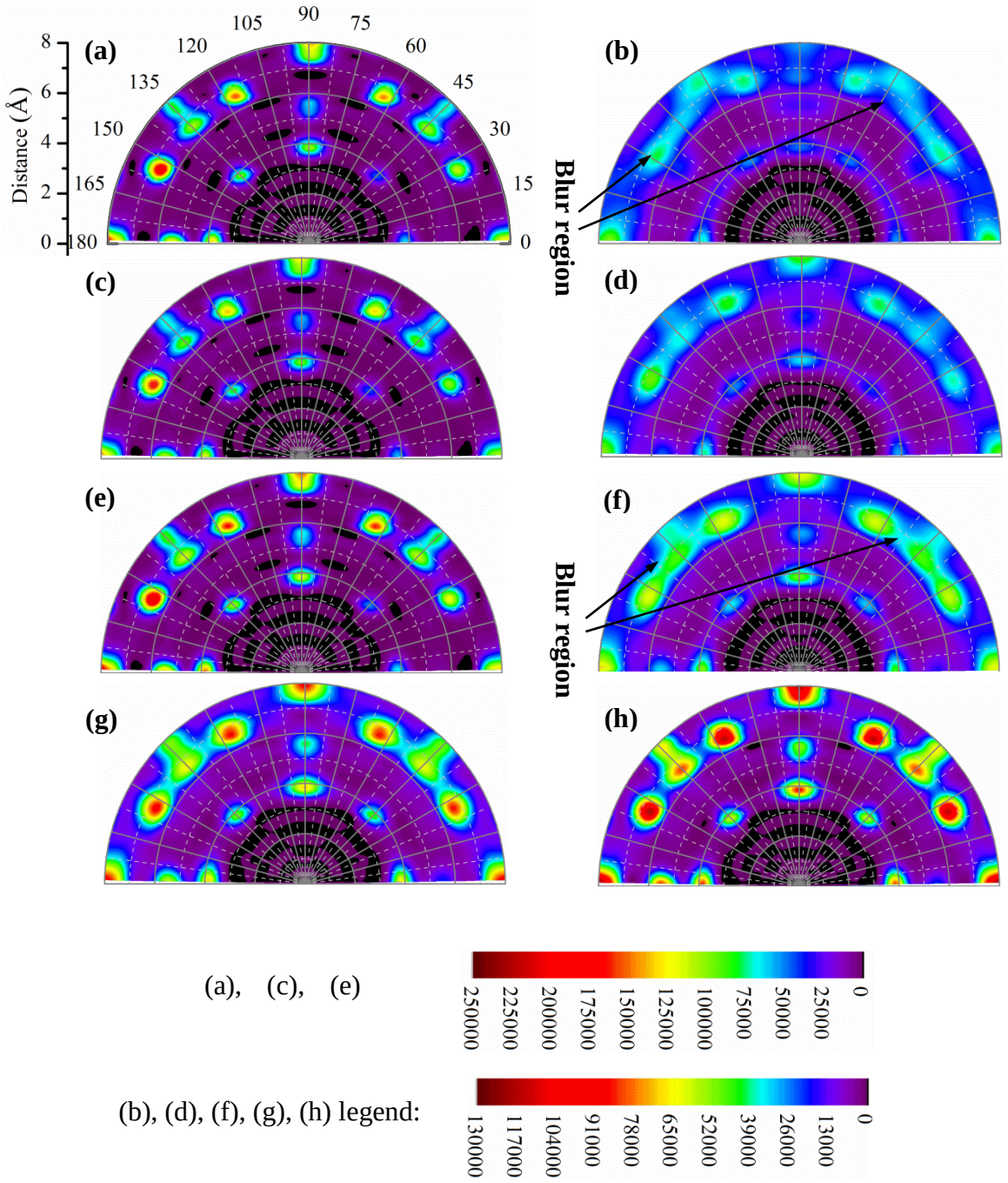

Fig. 3.8 Polar contour of the orientation-radial distribution function (ODF). The calculation is conducted in the *x*-*y* plane. The angle is the one between the line connecting the two atoms and the *x* axis. It is defined to range from 0 to 180 degrees. The contour value demonstrates the atom number in certain distance range (0.1 Å) and angle range (2 degrees). (a) D= 5 nm, E= 2.7 mJ/cm^2, initial state (before laser energy is applied); (b) D= 5 nm, E= 2.7 mJ/cm^2; final state; (c) D= 8 nm, E= 2.7 mJ/cm^2, initial state; (d) D= 8 nm, E= 2.7 mJ/cm^2, final state; (e) D= 10 nm, E= 2.7 mJ/cm^2, initial state; (f) D= 10 nm, E= 2.7 mJ/cm^2, final state; (g) D=

10 nm, E= 2.0 mJ/cm^2, final state; (h) D= 10 nm, E= 1.5 mJ/cm^2, final state. The major tick is every 15 degrees for the angle and 2 Å for the distance. The difference among the initial states for different particles size is small. (b), (d), (f) show that the smaller particles are much easier to be twisted. (f), (g), (h) inform us that a high laser fluence induces severe twist of particles.

The angle variation with the atom-atom distance after consolidation for D= 10 nm, E= 2.7 mJ/cm^2 is explored for the analysis as shown in Fig. 3.9. The 1st nearest distance is 3.83 Å. As we refer to Fig. 3.9, the angle should be 0˚, 45˚, 90˚, 135˚, and 180˚. The 2nd nearest distance is 5.41 Å, and the angles are 0˚, 90˚ and 180˚. The 3rd nearest distance is 6.63 Å. The corresponding angles are 26.6˚, 45˚, 63.4˚ and 116.6˚, 135˚, 153.4˚. The 4th nearest distance is 7.66 Å. The corresponding angle are 0˚, 45˚, 90˚ and 135˚, 180˚. The intial state [Fig. 3.9 (a)] is very close to the perfect crystal structure: the peak of each order nearest distance is well located at the corresponding angle and the peak is sharp. At the final state [Fig. 3.9 (b)], the peak is blunt and the distribution is no longer well located around the specific angle, especially for the 3rd nearest distance. The atoms are widely ranged from 26.6˚-63.4˚ and 116.6˚-153.4˚, which is corresponding to the blur region in figure 3.9 (f). The crystal structure at final state are twisted to widely spread in the angle regions.

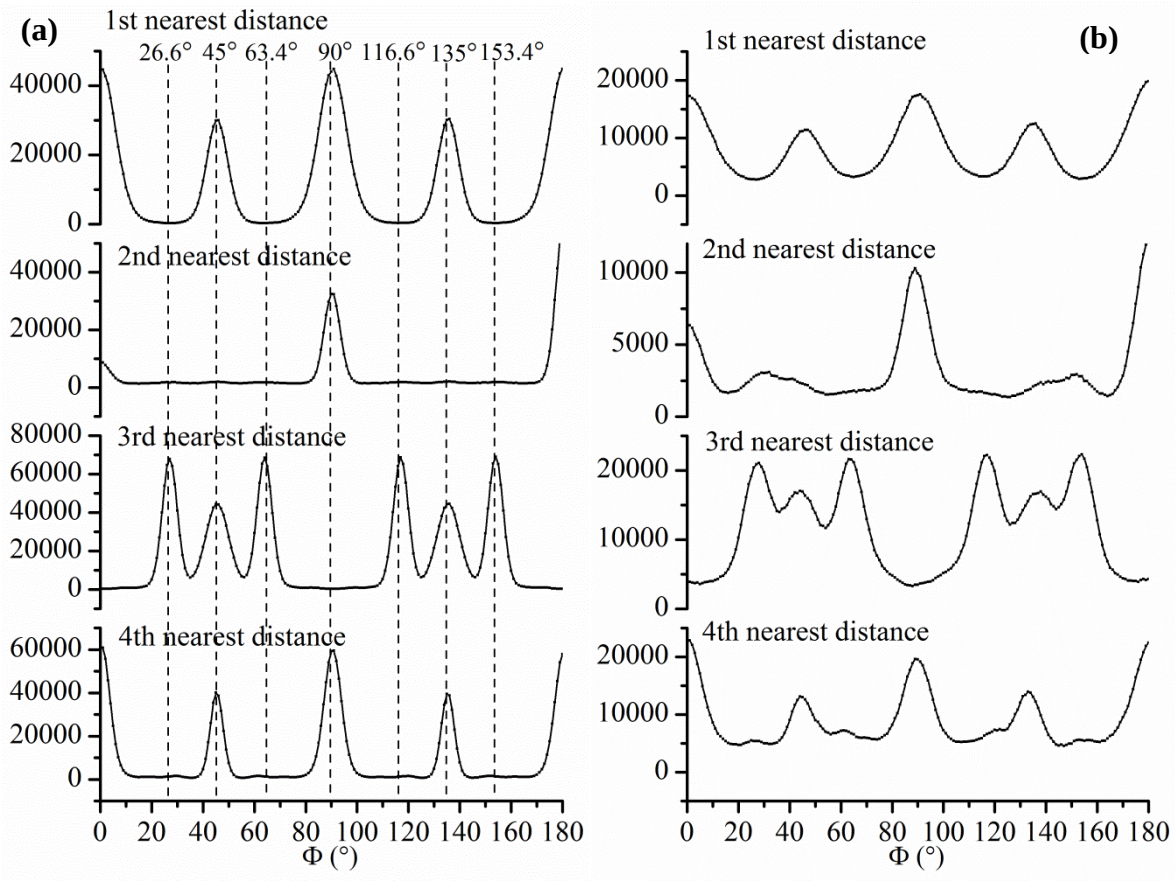

Fig. 3.9 The angle distribution of the atoms in the 1st-4th order nearest atom distance for *D*= 10 nm, *E*= 2.7 mJ/cm^2. The *y* axis value is the atom number per degree in the corresponding distance. (a) The angle distribution at the intial state (before the laser energy is applied). Sharp peaks are observed around certain angles which are indicated by the dash lines; (b) The angle distribution at the final state. The peaks are still visible but less sharp. The atoms are quite broadly distributed in angles compared with (a).

The atom number in the destructed state is studied to reveal the process of compressing. Figure 3.10 shows the evolution of the destructed-state atom number against time. The peak point can be viewed as the number of destructed atoms (including temporary and permanent destruction). It is easy to understand that a high laser fluence leads to more destructed atoms when the nanoparticles size are the same where the total atom number is the same. For most cases, the destructed atom number will rise and then fall, which indicates a

destruction-then-reconstruction process. However, for the case D= 5 nm, E= 2.7 mJ/cm^2, the number of destructed atoms will rise and then stay on the plateau value, which means the damage of the crystal structure is mostly a plastic process.

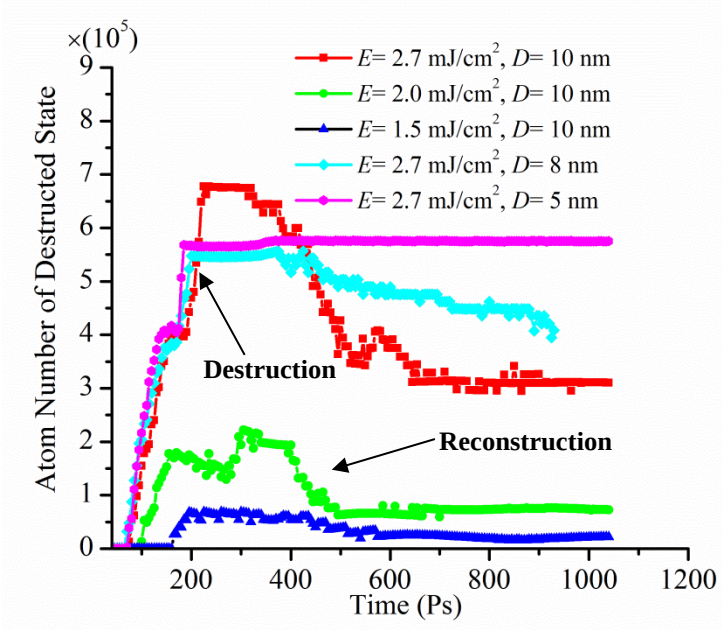

Fig. 3.10 Evolution of the number of atoms in destructed state against time. Five cases are investigated as indicated in the legend. For the case D= 5 nm, E= 2.7 mJ/cm^2, the atoms are completely destructed into destructed state and no reconstruction process is observed. In the other 4 cases, reconstruction of the temporarily destroyed structure occurs and the reconstruction number can be viewed as the final plateau value for each case.

CHAPTER 4. SHOCK WAVE CONFINEMENT-INDUCED PLUME TEMPERATURE INCREASE IN LASER-INDUCED BREAKDOWN SPECTROSCOPY

Spatial confinement is found effective in improving the sensitivity of laser-induced breakdown spectroscopy (LIBS). This work reports on the physics of shock wave spatial confinement via atomistic modeling. Reflection-induced atomic collision/friction near the wall reduces the shock wave velocity close to zero and remarkably increases the local temperature (~218 *K*) and pressure. As a result, the reflected ambient gas expands quickly toward the plume and compresses it. The temperature of the plume goes up significantly in the compression process: from 89 to 132 *K*. The lifetime of the plume is also boosted dramatically, from 480 ps to ~1800 ps.

4.1. Methodology

Argon is chosen as the material for the investigation in this work. The LJ potential well depth ε is 1.653×10^{-21} J and equilibrium separation parameter σ is 3.406 Å. And the cut-off distance is set to 2.5σ. A large domain size and a long laser pulse require more time for computation. To achieve an efficient computation, a picosecond laser pulse and a nanometer size domain are adopted. For the convenience of comparison, simulations of the cases with potential walls and without potential walls are conducted. The main difference lies in the boundary condition settings. The spatial confinement is accomplished by the wall boundary condition while the free space condition is achieved by the periodic boundary condition. Figure 4.1 shows the model size of the case with potential walls in this work. The whole simulation box measures $32.5\times2.7\times1000$ nm^3 ($x\times y\times z$) and the case with free space has a box

size of $32.5 \times 2.7 \times 3627$ nm^3 ($x \times y \times z$). The target size is $32.5 \times 2.7 \times 108.3$ nm^3 for both cases. The gap between the bottom of the target and the bottom of the simulation box is 271 nm. The total atom number is 264660 for the confinement case and 337500 for the free-space case.

The case with potential walls is employed to investigate the spatial confinement effect. A wall potential (wall/LJ93) is implemented in the upper and lower boundaries along the z direction. The other four boundaries are periodic. The strength factor ε for wall-atom interaction is 1.653×10^{-21} J and the size factor σ is 3.615 Å in this work. 8.515 Å is chosen as the cutoff distance for the wall boundary. 5 fs is chosen as the timestep for the simulation. For the free-space case, periodic boundary conditions are applied in all six boundaries. More details concerning the setup of the models can be seen in our previous work [22, 70].

The full width at half maximum (FWHM) of the incident laser beam intensity distribution is 11.5 ps and the peak is at 9 ps as shown in Fig. 4.1(b). The laser fluence is 5 J/m^2 and the pulse duration is 40 ps.

To avoid the downward movement resulting from the laser shock wave and the expected disturbance of the reflected stress wave, a special treatment is applied to the bottom (of size Δz= 1 nm) of the target to absorb the stress wave resulting from the laser irradiation. An external force is added to a specified bottom layer which is approximately 10 Å thick. The force is used to eliminate the stress-induced momentum. The theory and the details of implementation can be seen in our previous work [22, 70] and the work by Zhigilei [71].

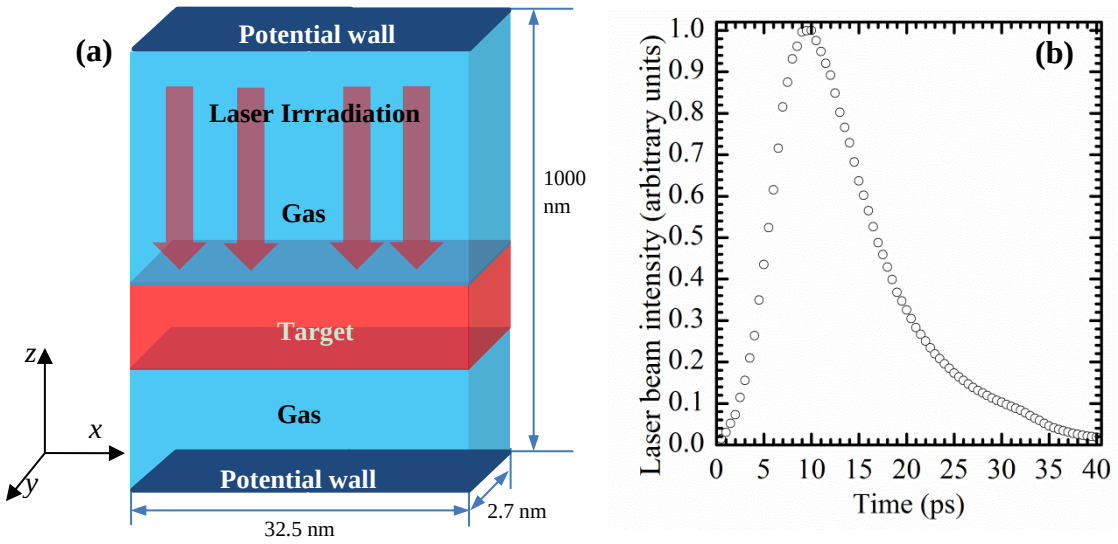

Fig. 4.1 (a) Atomic configuration of the model for the case with spatial confinement. The entire simulation box measures $32.5\times2.7\times1000$ nm^3 ($x\times y\times z$). The target measures $32.5\times2.7\times108.3$ nm^3 ($x\times y\times z$). The gap between the bottom of the target and the bottom of the simulation box is 271 nm. Laser energy propagates in the negative z direction. For the confinement case, the upper and lower boundaries along the z direction are in wall/LJ93 potential. The other four boundaries are periodic. For the free-space case, the simulation box size is $32.5\times2.7\times3627$ nm^3. The target size and location remains the same as the spatial confinement case. But the six boundaries are in periodic boundary condition. (b) Laser profile. The FWHM of the pulse is 11.5 ps, and the peak is located at 9 ps. Laser fluence in this work is 5 J/m^2.

4.2. Results and discussion

4.2.1. Shock wave confinement and temperature enhancement: general pictures

Two cases: (1) E= 5 J/m^2, τ= 5 nm, with spatial confinement and (2) E= 5 J/m^2, τ= 5 nm with free space are explored and discussed. The shock wave and plume evolution against time for the case with periodic boundary conditions (free space) has been investigated before. Details can be seen in our previous work [22, 70].

Figure 4.2 is a series of snapshots at different times of the case with confinement. The target ablates at first because the laser fluence is above the ablation threshold for argon. The explosive plume then moves upward and pushes the ambient gas (red in the figure) to move forward at a supersonic speed. At t= 80 ps, the shock wave is still in the beginning stage of formation. When it comes to t= 400 ps and t= 720 ps, the shock wave front and plume are split. Interestingly, the ablated atoms are not moving forward with the same speed and the plume is separating from each other because of the velocity difference. The density of the plume front is higher than the bottom part since the relatively fast part of plume is constrained by the ambient gas. And this is similar to the shock wave. Considering that the whole simulation box is 1000 nm along the z direction and the top surface is a potential wall, reflection of the shock wave is expected to occur. Our simulation results show that the shock wave front is reflected at around t= 1000 ps after the laser irradiation.

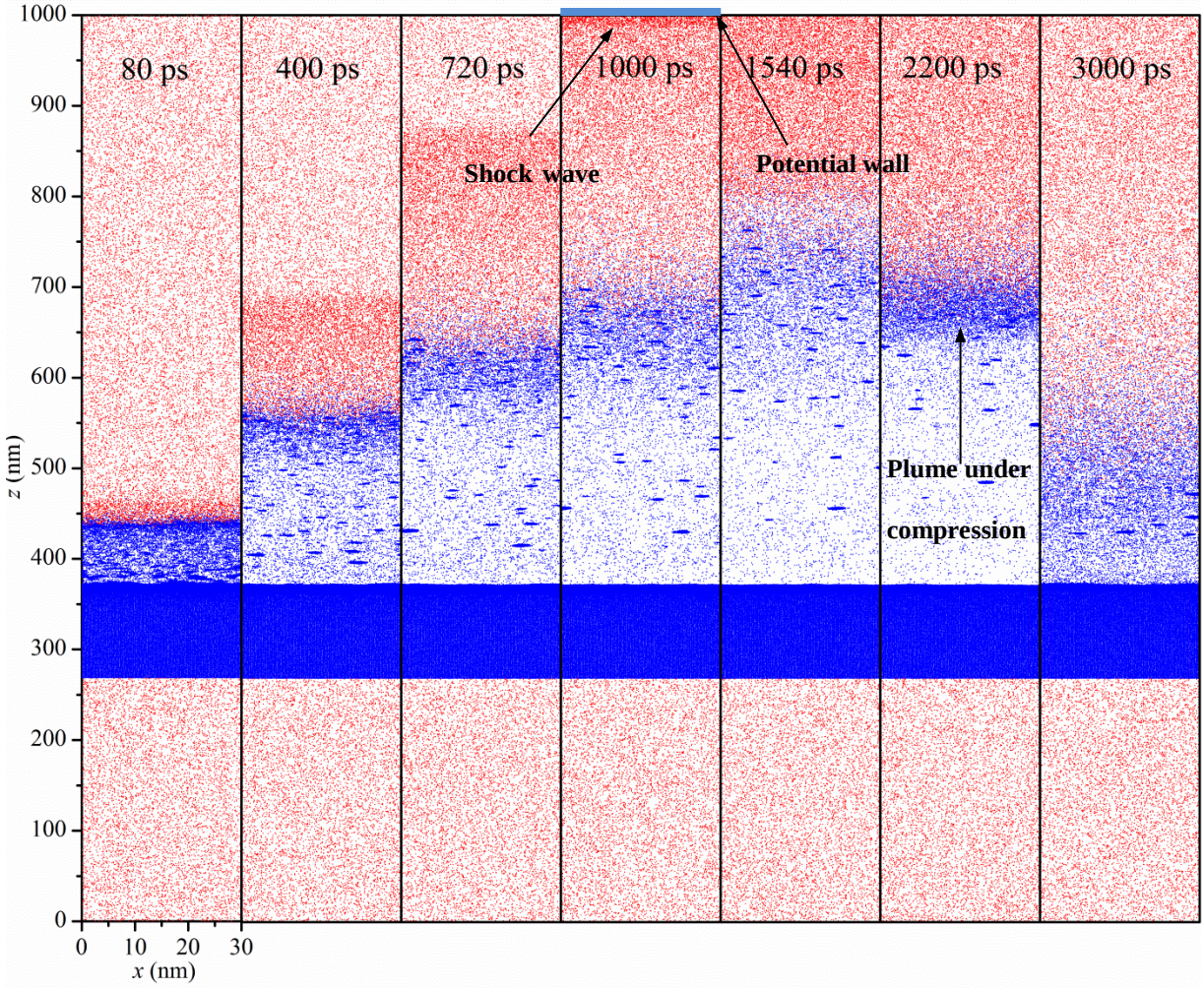

Fig. 4.2 Snapshots of the spatial confinement case. The reflection happens around *t*= 1000 ps as marked in the figure. Snapshots from *t*= 80 ps to *t*= 720 ps are the ones before the reflection and the ambient gas is compressed. Snapshot from *t*= 1540 ps to *t*= 3000 ps are after the reflection and the plume is compressed. Before the reflection, the shock wave depth is increasing with time while the plume density is decreasing. After the reflection, the plume is compressed and the plume density increases with time.

The ambient gas is much denser near the potential wall at *t*= 1000 ps which is the same time that the reflection occurs as in Fig. 4.2. Interestingly, the ambient gas is not observed to be reflected immediately at a high speed. Instead, the plume continues to move forward by the comparison of the plots of *t*= 1000 ps and *t*= 1540 ps. From the start of the

ablation to the moment the shock wave reaches the upper potential wall, the front of the plume becomes less and less dense. While from t= 1540 ps to t= 3000 ps, the plume front is becoming denser and denser, which indicates the plume is under compression from the reflected shock wave. The plume reaches the longest depth at t= 1540 ps in Fig. 4.2. Along with the compression process, the plume depth is decreasing and finally at t= 3000 ps, the plume and ambient gas have penetrated into each other and the interface of the plume and ambient gas is less distinguishable.

Figure 4.3(a) is the temperature contour of the whole simulation system. At the beginning of the material ablation, the ejected plume is at high temperature (above 500 K). Because of the interaction of the plume and the ambient gas, a high temperature shock wave is generated. At the same time, the velocity difference results in the separation of the ejected clusters. The upper part of the plume is at a slightly higher temperature. A closer look at the temperature distribution in the shock wave, as the inset in Fig. 4.3, reveals that the temperature at first increases to a high value and then drops down along the negative z direction. The physical front of the shock wave is not at the highest temperature. For the convenience of defining the shock wave front, we assume the layer at the highest temperature in the shock wave region is the shock wave front in this work. It is well documented that the shock wave fronts are usually characterized by discontinuities in density and pressure. In the past we have confirmed that in laser-material interaction the highest temperature-defined shock wave front indeed is consistent with that defined by density and pressure discontinuities. For a normal shockwave, temperature, pressure and density all experience discontinuities across the shockwave front. Caution should be exercised on using temperature

to define the shock wave front when the shockwave front is not normal to the local propagation front (oblique shock wave).

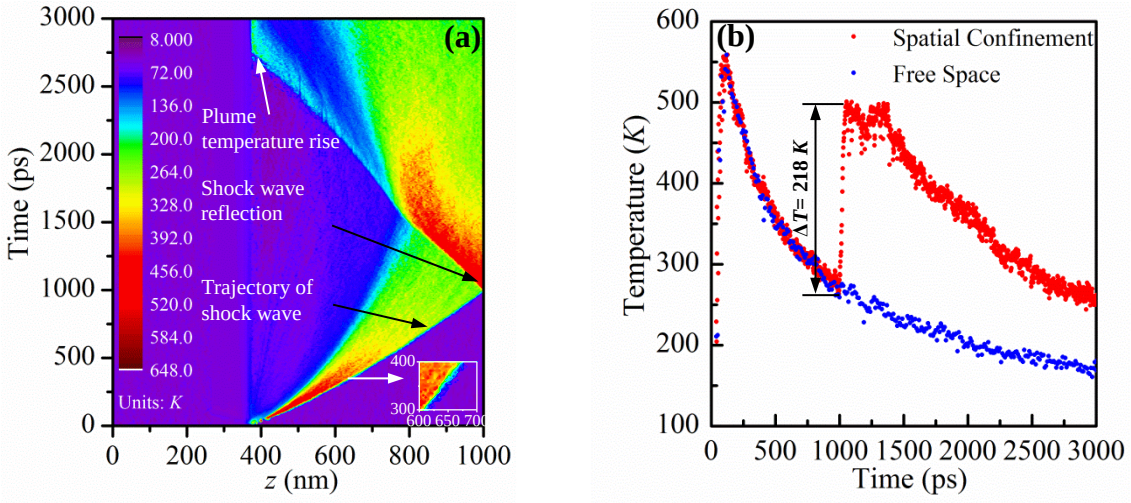

Fig. 4.3 (a) Spatiotemporal contour of temperature. There is a temperature jump of ambient gas right after the reflection at t= 1000 ps. The temperature rise of the plume is also observed when it is compressed by the ambient gas after t= 1500 ps. This temperature rise reaches a very substantial level at about 2700 ps as indicated in the figure. The inset shows that the temperature of the shock wave is not the highest in the physical shock wave front. Instead, the temperature of the shock wave will at first increase to a high value and then decreases smoothly along the negative z direction. (b) Shock wave front temperature comparison for the cases with spatial confinement and the case with free space. Before t= 1000 ps, the data of the cases with confinement and with free space agree with each other very well. After t= 1000 ps, the temperature of the free-space case drops down smoothly. However, for the case with wall-confinement, a temperature rise of about 218 K is observed.

Figure 4.3(b) shows the temperature evolution of the shock wave front against time. In the beginning stage of shock wave formation, a sharp temperature rise occurs. Then the temperature of the shock wave is observed to drop continuously. The data for the case with spatial confinement and the case with free space agree well with each other before the shock wave reaches z= 1000 nm. However, right after the shock wave reaches the wall, the shock wave front temperature jumps from 277 K to 495 K as shown in Fig. 4.3(b) for the case with

confinement. The high temperature remains at around 495 *K* for 330 ps from 1050 ps to 1380 ps when the plume continues to compress the shock wave. Then the temperature of the shock wave begins to decrease smoothly. There is no temperature rise for the shock wave front of the free-space case after its formation and its temperature drops down smoothly.

When the plume continues to compress the shock wave after *t*= 1000 ps, the pressure of the upper ambient gas increases and the plume density in the lower part decreases. This also means the pressure difference between the plume and shock wave is becoming larger. Finally, this big pressure difference results in the backward movement of the ambient gas which pushes the plume down, as shown from *t*= 1540 ps to 3000 ps in Fig. 4.2. Congruently, in Fig. 4.3(a), the plume temperature rise is observed after *t*= 1500 ps which is noticeable around *t*= 2700 ps. The plume temperature rise in the final stage is of great significance for the sensitivity improvement in LIBS since the temperature rise will elongate the radiation lifetime and increase the signal intensity.

4.2.2. Shock wave confinement and reflection: physics behind the temperature enhancement

In Fig. 4.3 we observed a clear temperature rise of the shock wave front after reflection, and a later-on temperature rise of the plume. In this section, we intend to study various aspects of the shock wave and plume, in anticipation to uncover the physics behind the temperature rise. First, we study the mass distribution: atom number density, to gain a fundamental understanding of shock wave confinement and the following compression of the plume by the reflected shock wave. Figure 4.4(a)-(c) is the number density contour, which

includes the total number density contour, the gas atom density and target atom density contour. The movement of the ejected clusters and the shock wave is quite distinct as marked in Fig. 4.4(b) and (c).

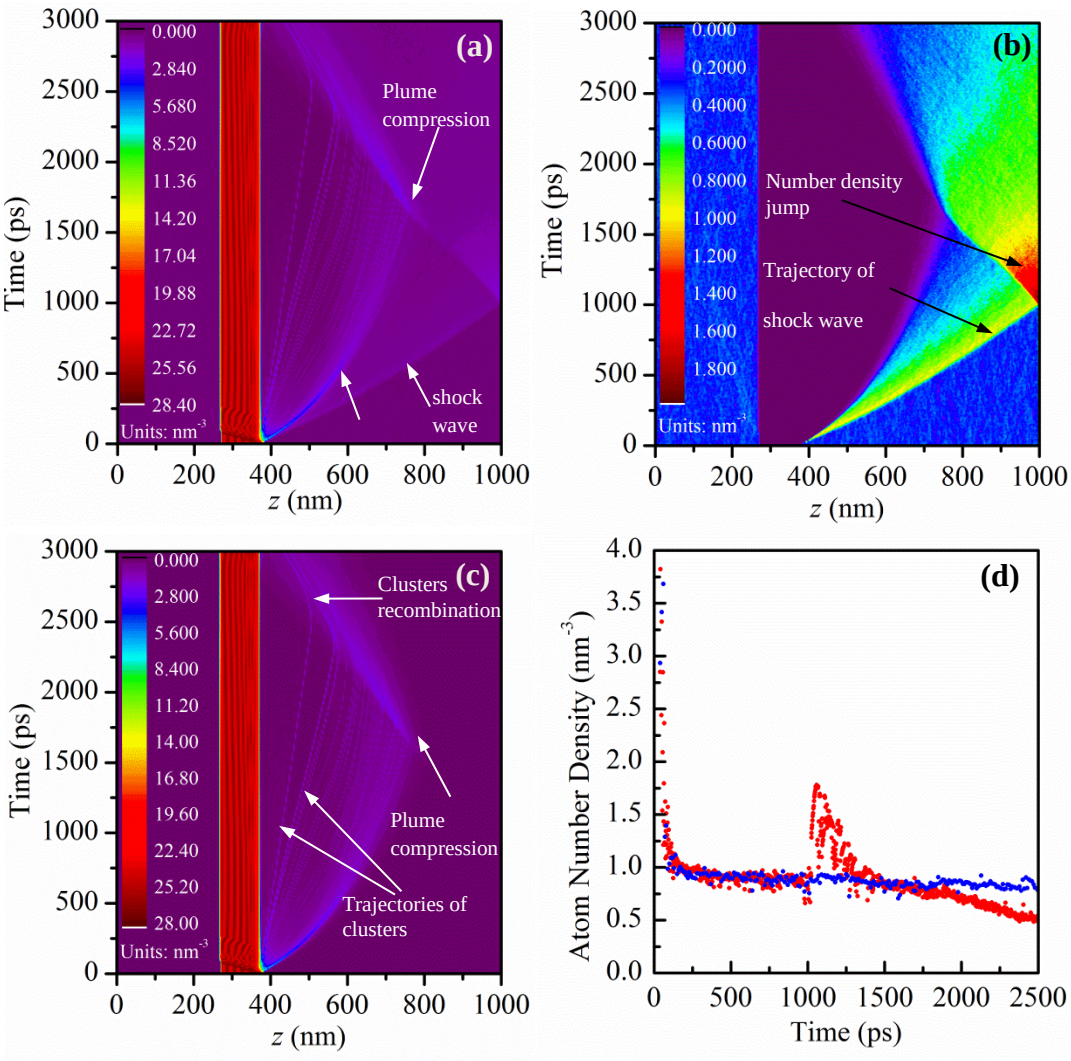

Fig. 4.4 Number Density contour. (a) Total atom number density which includes both the target atom and the gas atom. The trajectories of the shock wave and the ejected clusters are easily distinguishable. The plume and shock wave split from each other right after the ablation. The shock wave reflection happens at t= 1000 ps. The moving-back gas starts to compresses the plume at t= 1500 ps. (b) Ambient gas atom number density. A density jump is observed after the reflection at t= 1000 ps. (c) Target atom number density. The trajectories of the clusters are marked out. After the shock wave is reflected, a lot of clusters combine with each other under the compression of ambient gas. (d) Comparison of the shock wave front atom number density for the case with spatial confinement and free-space case. There is a sudden rise of atom number density right at the moment of reflection.

The shock wave is generated as a result of the compression of the ambient gas by the ejected plume. The plume and the shock wave are observed to split from each other right after the ablation. Because of the velocity difference between them, the gap between the plume and the shock wave grows with time before reflection as shown in Fig. 4.4(a). Similar to the temperature distribution, the density is not highest at the interface between the shock wave and ambient gas. It increases to a high value and then drops quickly toward the ambient gas. The results show the shock wave front defined using the highest temperature always has the highest density in the shock wave. Right after reflection, there is a number density jump due to the continuous compression of the shock wave. This is clearly marked in Fig. 4.4(b) (the red region close to the wall). After that, the atom number density of the shock wave decreases continuously.

As shown in Fig. 4.4(c), the ambient gas starts to suppress the plume at approximately t= 1500 ps, causing some of the clusters in the plume to re-combine. An increase of the number density of the plume is observed. Figure 4.4(d) shows the comparison of the atom number density of the shock wave front for the case with confinement and free space. The potential wall results in an atom number density increase of almost 2 times in the shock wave front. At the end of the simulation, a small portion of the ambient gas penetrates into the plume. This can also be clearly seen in Fig. 4.2 at 3000 ps. The shock wave front atom number density is lower than that without spatial confinement from t= 1700 ps due to the continuous relaxation of the reflected-shock wave's pressure.

Figure 4.5(a) is the pressure contour of the system. The stress wave in the solid is very clear. For the detailed analysis and discussion of the stress wave in the solid, please refer to our previous work [70, 72]. The ablated material in high speed leads to the sharp rise of the ambient gas pressure. Due to the interaction of the shock wave and the ambient gas, the pressure of the shock wave experiences continuous decay before the reflection. However, it is always higher than the plume part and non-shock wave region in the ambient gas. Right after the reflection, a sudden pressure rise is observed around the time t= 1000 ps. Refer to Fig. 4.2, this is the moment when the shock wave reaches the potential wall and is reflected. Dunbar *et al* discovered that the pressure of the shock wave front could increase as many as 11 times in their spatial confinement experiment [58]. Shortly after that, the shock wave pressure decreases as a result of its backward movement and the pressure drops just like the number density. During this backward motion, the pressure of the shock wave is larger than the pressure in the plume region. This is the driving force of the backward movement of the shock wave. At the end of the simulation, the difference in the pressure is blurred and the ambient gas and plume mix with each other. In summary, it is clear that right after the reflection, the shock wave front's pressure is increased dramatically, much higher than the plume's pressure. This pressure difference causes the ambient gas to move back toward the target and the compression of the plume. To have a clearer understanding of this movement reversal process we plot the velocity contour shown in Fig. 4.5(b).

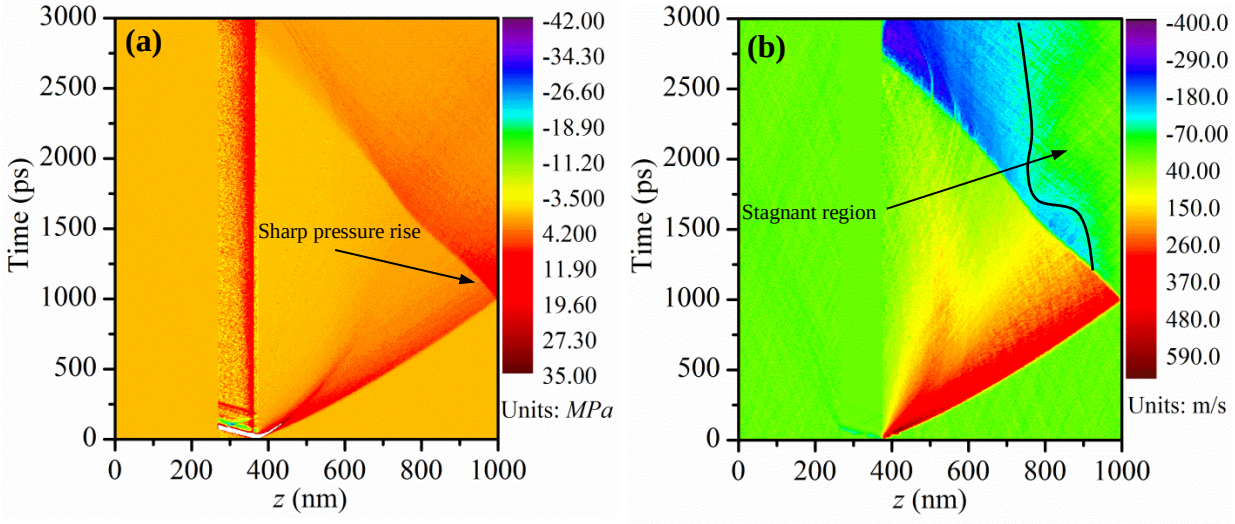

Fig. 4.5 (a) Pressure contour of the whole simulation system. A large compressive stress occurs in the solid at the beginning of laser ablation. With the split of the plume and shock wave, the pressure drops down smoothly. However, at approximately t= 1000 ps, another big pressure occurs in the shock wave due to the reflection and confinement. (b) Velocity contour. The ejected plume has a high velocity. The interaction of the ambient gas and the plume results in the dissipation of the velocity. The plume and the shock wave slow down smoothly before the reflection. The reflection by the potential wall results in a sudden drop of the velocity of the shock wave. Then the ambient gas accelerates to move towards the plume due to the big pressure difference. The ambient gas starts to compress the plume at around t= 1500 ps and the reflected-shock wave stops accelerating at that moment. At the same time, the plume starts to accelerate to move back toward the target surface due the compression by the reflected ambient gas.

We clearly see a velocity rise after the ablation and the plume and shock wave move in at different velocities. This finally results in the separation of the plume and shock wave. The atom collision brings the velocity of the ambient gas adjacent to the wall area close to 0 when the shock wave arrives at the potential wall and is reflected back. A large part of the kinetic energy of the shock wave is converted to thermal energy due to the collision. Therefore, a sudden temperature rise occurs. The pressure also increases abruptly at this moment as shown in Fig. 4.5(a). Then, the remaining part of shock wave that is moving

forward collides with the atoms in the high pressure region and the velocity is absorbed quickly. Consequently, the stagnant region marked in Fig.4. 5(b) increases with time.

After reflection by the wall, the velocity of the shock wave increases with time due to the fact that its pressure is higher than that in the plume, illustrated in Fig. 4.5(a). This is due to the phenomenon that the compressed shock wave front accumulates in the near-wall region, leading to a very high local pressure. Interestingly, after the reflection, only the interface of the ambient gas and the plume possess a high velocity. The other parts are almost stagnant as marked in Fig. 4.5(b). The velocity of the upper ambient gas in the region z> 740 nm is around zero since t= 1900 ps. This means their kinetic energy is almost completely converted into thermal energy. Figure 4.3(a) shows this stagnant region has a stable and high temperature. When the plume is under compression from the reflected shock wave, its velocity starts to decrease to zero. Then it moves toward the target surface. The highest velocity of the plume occurs at the end of the simulation. The pressure of the plume also increases because of the compression by the shock wave. Similar to the temperature rise at the moment of reflection of the shock wave, the shock wave's collision with the plume and with the ambient gas contributes to the temperature increase of the plume.

4.2.3. Temperature and lifetime of plume

In LIBS, the critical factors determining the signal intensity and probing sensitivity are the temperature and lifetime of the plume. In this section, these two factors are studied in detail under the shock wave confinement. Figure 4.6(a) is the comparison of the velocity of the shock wave front for the case with confinement and the case with free space. A sharp

jump in the velocity of the shock wave front occurs when the shock wave forms. The reflection occurs at around *t*= 1000 ps. Before *t*= 1000 ps, the two lines are almost the same. For the free-space case, the velocity decreases smoothly with time. However, in the spatial confinement case, the velocity drops from 311 m/s to 0 suddenly at *t*= 1000 ps due to wall reflection. Then the shock wave front moves toward the plume with an increasing velocity. This is because the accumulated shockwave front in the near-wall region induces a very high local pressure. This high pressure pushes the ambient gas to move toward the target surface region, where the local pressure is much lower. Around *t*= 1500 ps, the velocity begins to decrease and is approximately zero after *t*= 2000 ps. The decrease in velocity starting at 1500 ps results from the collision of the backward-moving shock wave and the forward-moving plume. Starting from this moment, the backward-moving shock wave is in contact with the plume, and pushes them backward. Therefore, the shock wave front velocity begins to decrease. The kinetic energy of the ambient gas is converted to thermal energy. A large part of the energy is transferred to the plume through the compression and collision afterwards.

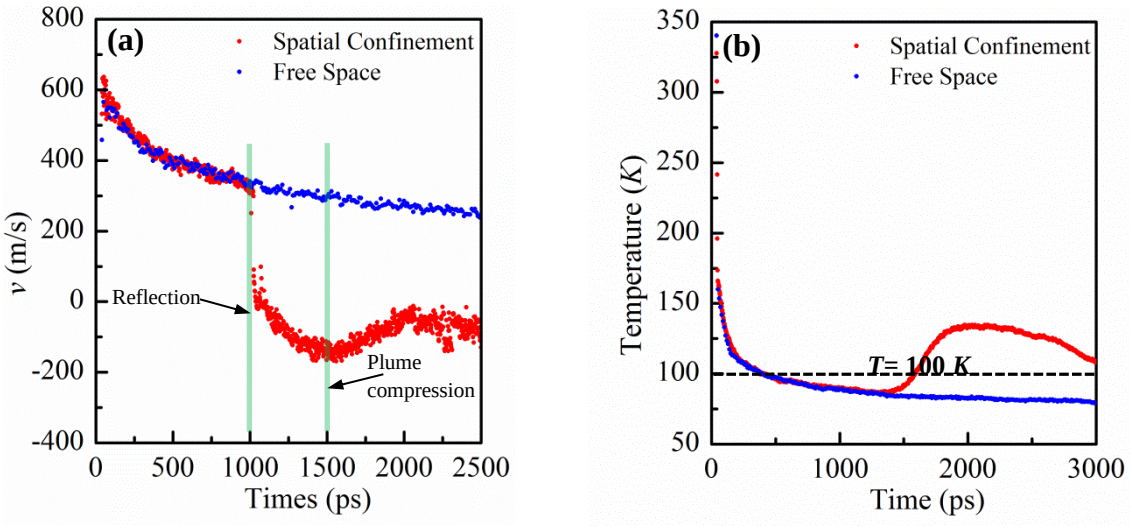

Fig. 4.6 (a) Velocity comparison for the cases with and without confinement. Before the reflection (*t*= 1000 ps), the results of the two cases agree well with each other. The reflection

results in a sudden drop of velocity (from 324 m/s to 0). The reflected-shock wave accelerates to move back towards the plume and then slows down. (b) Plume average temperature comparison. Only the plume above z>= 400 nm are counted in this work for temperature calculation. For the confinement case, the temperature drops down at first due to the interaction of the plume and the ambient gas. Part of the energy is transferred from the plume to the ambient gas. The plume is compressed by the ambient gas from *t*= 1500 ps. The plume temperature is observed to increase at this very moment. After *t*= 2500 ps, part of the plume is pushed to the region below *z*= 400 nm. The plume temperature decreases again. However, for the free-space case, the temperature decreases smoothly with time. Meanwhile, the time for the plume to stay above 100 *K* has been increased from 480 ps to 1800 ps because of the confinement.

Figure 4.6(b) is the average temperature of the plume. To calculate the temperature, we choose the target atoms above *z*= 400 nm, which moderately represent the plume in the physical process. The laser burst results in a sudden rise of the plume temperature. After that, the energy of the plume is transferred to the ambient gas and the temperature drop is observed. At the same time the plume and shock wave front are separating with each other and the gap is increasing with time, which means the interaction between the plume and shock wave is weakening. As a result, the rate of the temperature drop is decreasing with time as shown in Fig. 4.6(b). Around *t*= 1500 ps, there is a sharp temperature rise from 89 *K* to 132 *K* for the spatial-confinement case. This occurs at the same moment when the reflected-shock wave begins to compress the plume. The compression of the plume is the reason for the temperature rise. In the experiment, a temperature rise of the plasma as high as 3600 *K* (hemispherical cavity) and 1000 *K* (cylinder confinement) has been reported in Lu's group [60, 61]. After *t*= 2500 ps, the plume temperature begins to decrease, because only the plume that is above *z*= 400 nm is considered in the temperature calculation and part of the plume is pushed back below that region after *t*= 2500 ps. It is a little hard to define the life time of the plume that can be useful during LIBS in our case since we do not know exactly

above what temperature the plume will emit useful radiation that could be detected. The boiling point of argon is 87.35 *K*. If we take a value of 100 *K* as the criterion above which the plume is assumed to be able to emit useful radiation, some first-order life time analysis can be conducted here. As shown in Fig. 4.6(b), the time for the temperature above 100 *K* in the case with confinement is more than 1800 ps. In contrast, the time above 100 *K* in the free-space case is only 480 ps. The lifetime of the plume is significantly elongated by 1320 ps which is very beneficial for more sensitive detection in LIBS.

Although it is apparent that both the ambient gas and the plume experience a temperature rise, it is still possible that the average temperature in the contour maybe misleading. The average velocity of the ambient gas is around zero after the reflection. [Fig. 4.5(b)] There is a possibility that the reflected atoms and the forward-moving atoms have the same velocity but in opposite directions. Under such a scenario, the average velocity is still zero, but a lot of the movement is macro-scale translational movement, and cannot be used for temperature calculation. To confirm that the temperature in our case is the real temperature, the velocity distribution comparison with the velocity in the thermal equilibrium state (Maxwellian distribution) is given as Fig. 4.7. The atoms ranging from z = 975 nm to z= 985 nm are chosen as the region for the analysis here. The average temperature in that region at t= 1200 ps is 430K. The actual velocity data fits the Maxwell curve of velocity distribution in 430K as in Fig. 4.7. This proves the validity of our temperature evaluations.

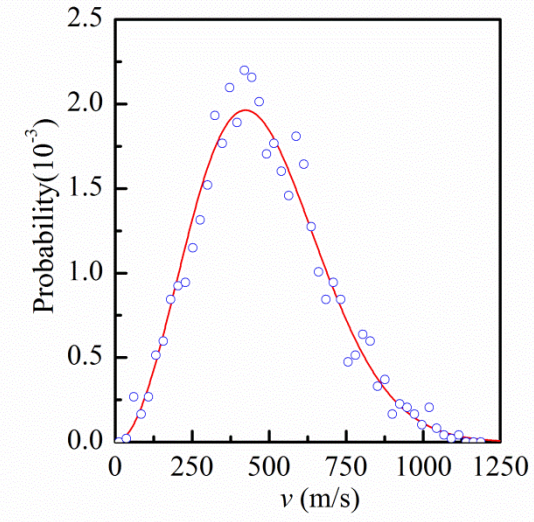

Fig. 4.7 Comparison of the velocity distribution of atoms ranging from z= 975 nm to z= 985 nm at t= 1200 ps with Maxwellian velocity distribution. The solid line is the Maxwellian velocity distribution at T= 430 K which is the average temperature of the atoms in the selected region. The hollow dots are the velocity distribution of atoms in MD simulation.

CHAPTER 5. MATERIAL BEHAVIOR UNDER EXTREME DOMAIN CONSTRAINT IN LASER-ASSISTED SURFACE NANOSTRUCTURING

In this chapter, systematic atomistic modeling has been conducted to understand the tip-confinement effect on the surface nanostructuring. Material ablation was trapped by the tip and a significant decrease of the number of atoms flying out of the surface was observed. Tip oscillation occurred because of the interaction with the substrate. The effect of laser fluence and tip-substrate is explored.

5.1 Methodologies

Argon is chosen as the material in this simulation work, due to its great computational efficiency. This is critical for this work since our modeled system is composed of a large number of atoms and the whole physical process under simulation is very long (close to 5 ns). Argon crystal is arranged in the simple face-centered cubic structure and well described by the Lennard-Jones (12-6) potential. It is easy for the modeling and fast for the computation while the conclusion does not lose its generality. A lot of works in our group [7, 22, 70, 113, 114, 116] have proved its validity in laser-material interaction simulation. The LJ potential well depth ε is 1.653×10^{-21} J and the equilibrium separation parameter σ is 3.406 Å. And the cut-off distance is set to 2.5σ. LAMMPS is employed in this work. [63]

Figure 5.1(a) shows the physical model of the simulation and the domain construction. To save the computation cost, a quasi-3D model is adopted. The thickness of the whole simulation system (including the tip and the substrate) in the *y* direction is 10 nm: relatively small in scale compared with *x* and *z* direction size. Periodic boundary conditions are applied in

the *x* and *y* directions. The boundary condition in the *z* direction is the fixed boundary condition. The substrate measures 100 nm×10 nm ×30 nm (*x*×*y*×z). The interaction of substrate-substrate atoms obeys the Lennard-Jones (12-6) potential.

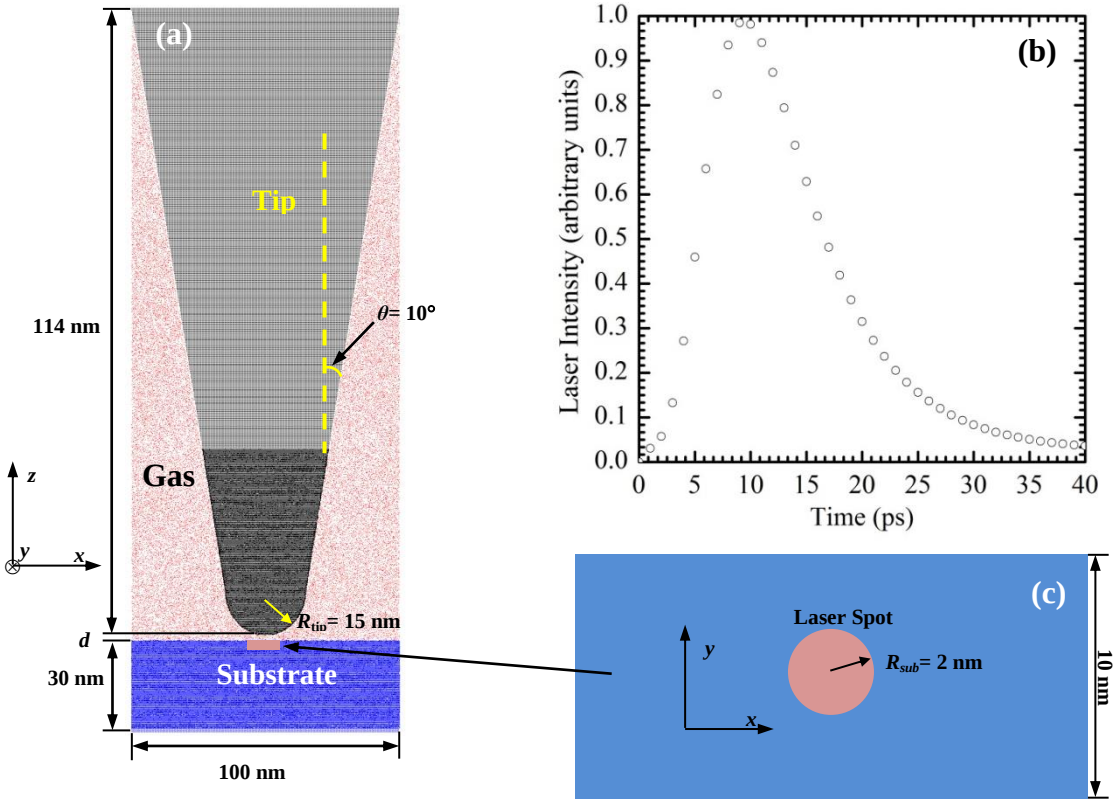

Fig. 5.1 (a) Physical model for simulating the tip-substrate nanostructuring process. The laser energy is focused to a circular region with R_{sub}= 2 nm in the substrate underneath the tip apex. The substrate measures 100 nm×10 nm×30 nm (*x*×*y*×z). There are 3 important parameters for the tip construction: apex radius R_{tip}= 15 nm, half taper angle θ= 10°, length of tip *L*= 114 nm. The atoms inside the tip at *z*≥ 98.1 nm are removed and the actual shape in the region *z*≥ 98.1 nm is an empty cell surrounded by 5 walls (*x*, *y* direction and *z* direction on the top) with a thickness of 1 nm. (b) Laser beam intensity distribution. The full width at half maximum (FWHM) of the incident laser beam intensity distribution is 11.5 ps and peak occurs at *t*= 9 ps. (c) Profile of the laser spot. The spot is circular with a radius of R_{sub}= 2 nm.

There are three important parameters for the tip construction: apex radius R_{tip}= 15 nm, half taper angle θ= 10°, and tip length L= 114 nm. The tip thickness is also 10 nm in the y direction. The atoms inside the tip at $z\geq$ 98.1 nm are removed and the actual shape in the region $z\geq$ 98.1 nm is an empty cell surrounded by the five walls (x, y direction and z direction on the top) with a thickness of 1 nm. The tip atoms in the region $z\geq$ 97.1 nm are set static. They do not move in the simulation. Since we are interested in the tip area close to the substrate, this simplification is not going to affect the final results and analysis. The tip is created based on the argon crystal. The interaction of tip-tip atoms are described by the LJ (12-6) potential as mentioned before. However, as to the interaction of the tip atoms and the substrate atoms, only the repulsive component is considered and the attractive force is neglected. And since the shock wave phenomenon [22, 69, 70] has been observed even at the nanoscale and the behavior of the tip and shock wave may be strongly changed due to their interaction, it is necessary to introduce ambient gas atoms [red dots in Fig. 5.1(a)] in this model. Only the repulsive force is considered for the gas-gas, gas-tip and gas-substrate atoms interaction. More details can be found in our previous works. [22, 70] The gas pressure is 0.22 MPa in the thermal equilibrium state at T= 50 K.

In the experiment, the substrate is placed underneath the tip. The incident laser irradiates the AFM tip in a certain polarization angle (the angle to the tip axis) which can be adjusted in the experiment. The tip serves as a receiving antenna to collect the laser energy as well as an emitting antenna which results in the enhancement of an optical field at the nanoscale. [112] For the MD simulation, the antenna effect of the tip is not easy to be realized. Since the laser absorption in the tip is ignored in this work and the emphasis is placed on the near-field heating of the substrate, the laser irradiation is focused on a circular spot with a radius of 2 nm on the

substrate. Figure 5.1(b) shows the laser beam intensity distribution. A single laser pulse of 40 ps is applied in this simulation work. The laser energy is spatially uniform on the spot. The full width at half maximum (FWHM) of the incident laser beam intensity distribution is 11.5 ps and the peak occurs at t= 9 ps. Laser energy absorption obeys the Beer-Lambert law. To accomplish it, the laser absorption region is divided into a number of bins of thickness Δz=1 nm. And the artificial absorption depth of 5 nm is used in our work. The incident laser energy decreased exponentially after the absorption in each bin. The details have been discussed in our previous works. [22, 69,70]

After constructing the whole physical domain for modeling and definition of atom interaction and boundary conditions, the system is at first treated as a canonical ensemble (NVT) and modeled for 1 ns and then a microcanonical ensemble (NVE) for 800 ps at T= 50 K to reach thermal equilibrium. Then the laser energy is applied on the substrate surface. After that, the whole system is in NVE again for recrystallization. During the laser irradiation and in the early stage of laser ablation, the time step is set to 2 fs. Other than that, the time step is set to 5 fs.

5.2 Results and discussion

In this section, the general picture of the material behavior under the tip-confinement is presented at first. Then the effect of tip-substrate distance and laser fluence is discussed. At last, the tip oscillation and substrate defects are investigated.

5.2.1 Material behavior under extreme domain confinement: a general picture

Surface nanostructuring is affected by the incident laser (including the laser fluence *E* and the polarization angle), the tip-substrate distance *d*, and the substrate material properties. In this modeling, different laser fluence *E* and various tip-substrate distance *d* are used to study their effects. The influence of these two factors is going to be discussed in the next several sections. In this section, the case of laser fluence E= 5 J/m^2, and tip-substrate distance d= 2 nm is chosen to demonstrate the general pictures of laser ablation and recrystallization process when tip-confinement is considered.

Figure 5.2 is the atomic snapshot at different times. Laser energy is applied from t= 0 ps. It is clearly shown that the ablation has already started at t= 10 ps. The tip apex is also affected by the ablation from the substrate. Without the tip-confinement, the ablated substrate material expands freely in the space and it has been studied in detail in our previous works. [22, 70] In this nanostructuring, the ablated materials attack the tip apex in high speed. Due to the close distance and the high speed of the ejected plume, the structure of the tip apex is distorted and becomes amorphous as shown at t= 20 ps. The dark region in the apex indicates the hot and amorphous status of the small part in the tip. And the destruction is not permanent since the region under destruction disappeared and no voids are formed afterwards.

Even though the laser pulse is very short, the thermal expansion lasts a relatively long time after the laser pulse. Figures from t= 10 ps to t= 100 ps show the thermal expansion and relaxation of the substrate. From t= 200 ps to the end of the simulation t= 4290 ps, recrystallization is observed. Because of the strong stress wave in the substrate, the structure of

the material is distorted from the well-arranged crystal structure as shown at t= 100 ps. From the atomic configuration, it is seen that most of the damages are temporary and it is back to the good crystal structure again in the recrystallization process. This can be confirmed by the crystallinity study discussed later. However, the destruction in the laser irradiation region is permanent. At the end of simulation at t= 4290 ps, a cone-shape crater forms. Meanwhile, defects close to the bottom in the substrate are also observed.

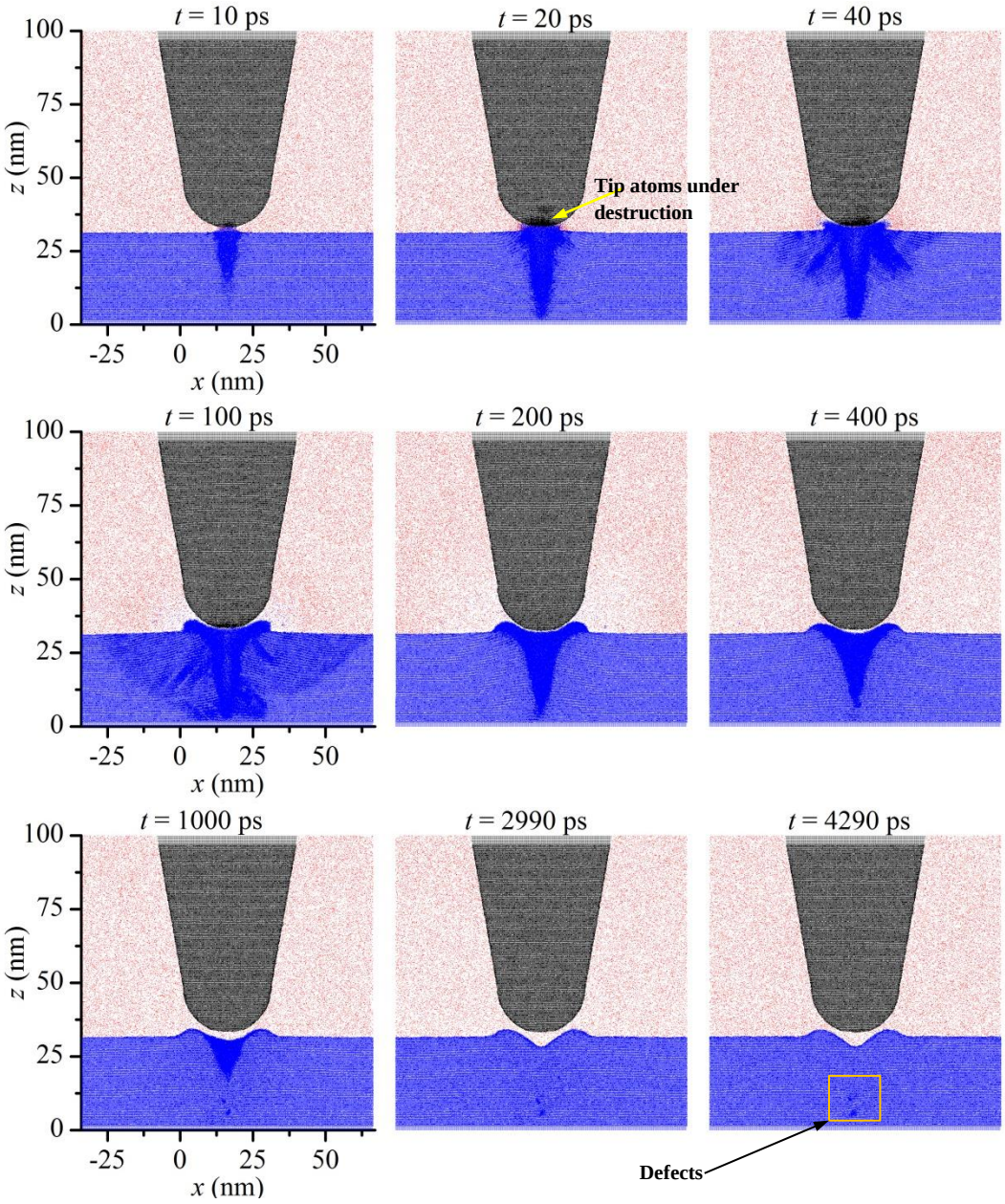

Fig. 5.2 Snapshots of the case E= 5 J/m^2, d= 2 nm. Laser ablation starts from around t= 10 ps. Because of the confinement by the tip, the ablated material is prevented from moving freely in space. The apex of the tip is slightly distorted by the ablated-out substrate. Recrystallization (t= 200-2990 ps) is observed following the ablation. Finally, a steady cone-shape crater is formed. And at the same time, there are defects in the final sample structure at the bottom, as marked in the figure at t= 4290 ps.

Figure 5.3 is for the temperature contours corresponding to the nanostructuring process in Fig. 5.2. Initially, the thermal equilibrium at T= 50 K of the whole system is achieved before the laser irradiation. Laser irradiation starts at t= 0 ps. A hot spot which is above 320 K is observed at t= 10 ps underneath the tip. From t= 10 ps to t= 40 ps, the region of high temperature expands because of the heat transfer from the irradiation spot to the surroundings. And at the same time, laser ablation is observed. However, the ablation is prohibited from expanding in space by the tip. Shock waves with a high temperature front are shown in the Fig. 5.3 at t= 100 ps. The temperature of the substrate drops continuously from 100 ps to 4290 ps. By the end of the simulation t= 4290 ps, the temperature of the substrate is close to 50 K again.

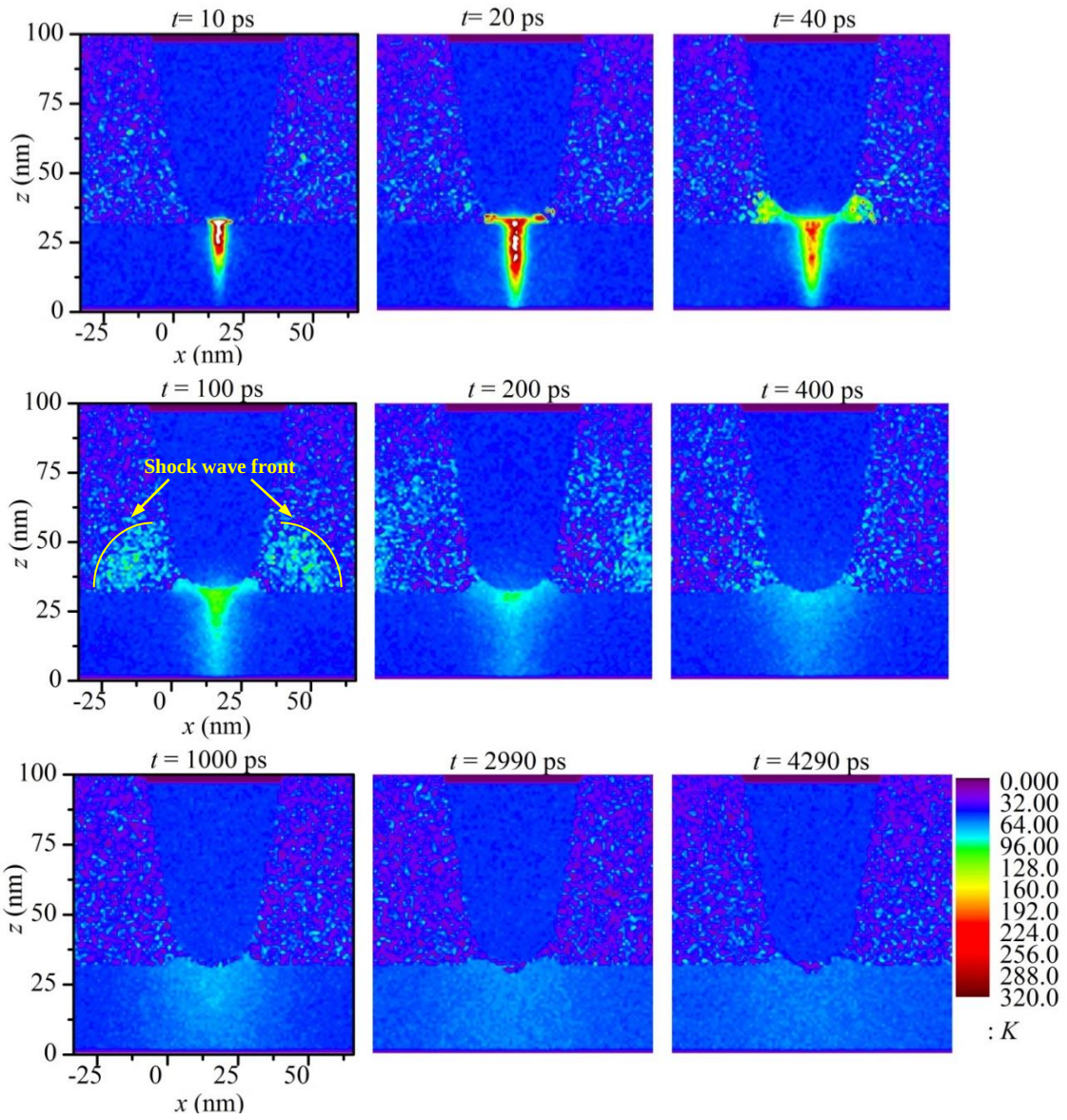

Fig. 5.3 Temperature contours of the case E= 5 J/m^2, d= 2 nm. The temperature of the area under direct laser irradiation goes up very quickly. And the high temperature results in ablation. Consequently, a shock wave can be seen very clearly at t= 100 ps and t= 200 ps. Afterwards, the temperature in this area goes down in the recrystallization process.

Figure 5.4 shows the atom number density contours for the case in Fig. 5.2. To get the contour, the whole domain is divided into $1\times10.2\times1(x\times y\times z)$ nm^3 cubes. In the part irradiated by the high energy laser, the atom number density decreases during the laser irradiation as shown

from *t*=10 ps – 40 ps. Argon lattice constant differs from the cube size in the contours. Consequently, the atom number density in the cubes changes periodically. The contours show patterned blocks of red and dark color and this periodicity is very helpful in viewing the structure distortion and defects. As the thermal energy dissipates towards the bottom and the surroundings, recrystallization occurs. From *t*= 200 ps, the atom number density increases continuously in the region of laser irradiation. Noticeably, there is distortion in the atom number density contour in the region of defects at *t*= 4290 ps. The final defects are the structure distortion effect.

The laser irradiation leads to the structure destruction of the substrate and distortion of the tip apex. Crystallinity is a good parameter to describe the crystal structure destruction and it is defined in chapter 3 as equation 6. If atoms are regularly distributed in space with the corresponding crystal structure, the function will be equal to 1. In the amorphous state, the function $\phi(r_{i,x})$ will be much less than 1, in fact very small (close to zero).

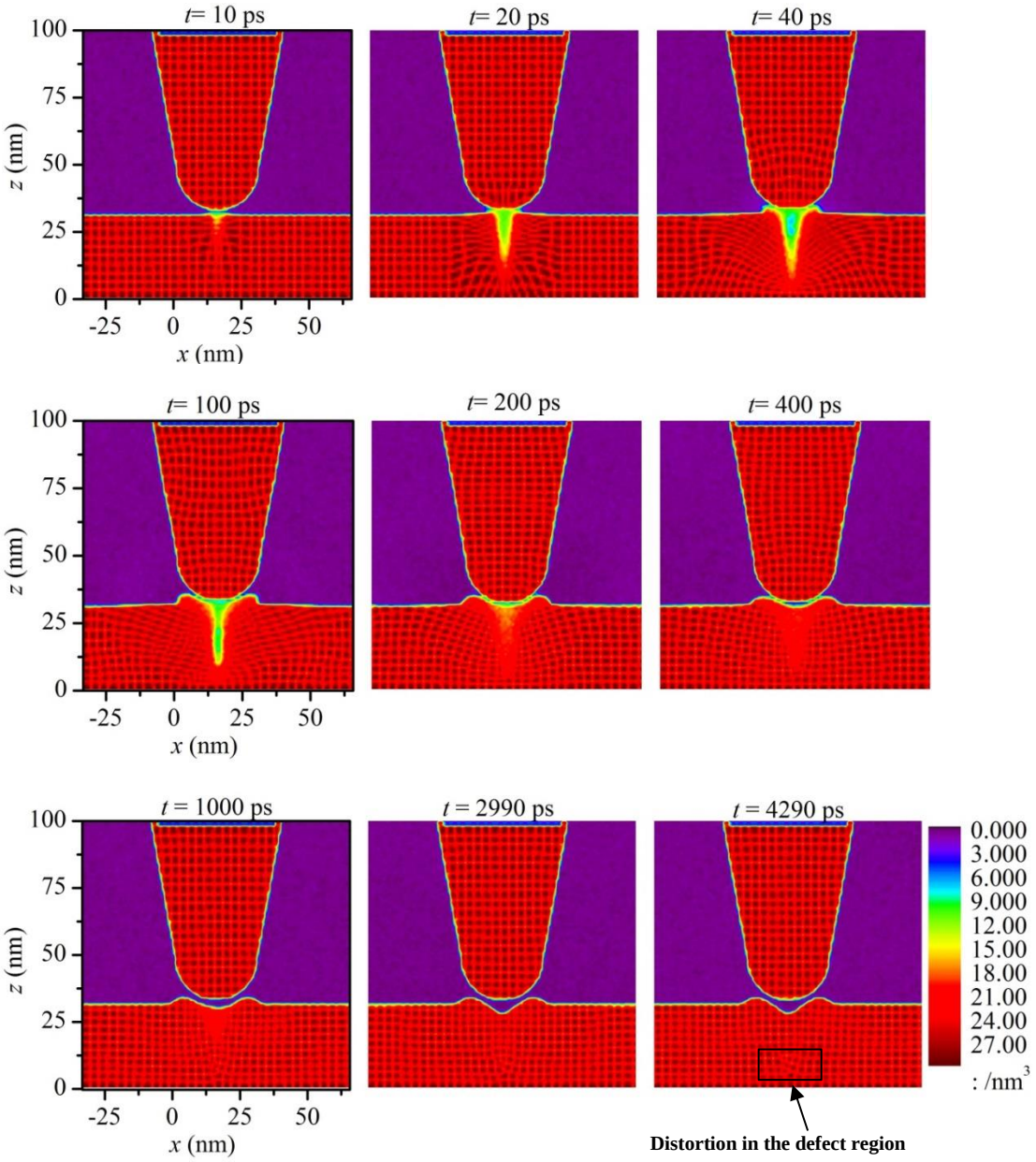

Fig. 5.4 Atom number density contours of the case E= 5 J/m^2, d= 2 nm. The whole domain is divided into 1×10.2 ×1 ($x \times y \times z$) nm^3 cubes. The melting area is characterized by the uniform low atom number density. The distortion resulting from the stress wave accompanies the melting process. The recrystallization starts from t= 200 ps. The distortion is remarkable in the place of defects. Argon lattice constant differs from the cube size in the contour calculation. Consequently, the atom number density in the cubes changes periodically. The contours show patterned blocks of red and dark color and this periodicity is very helpful in demonstrating the defects (e.g. lattice bending and dislocation).

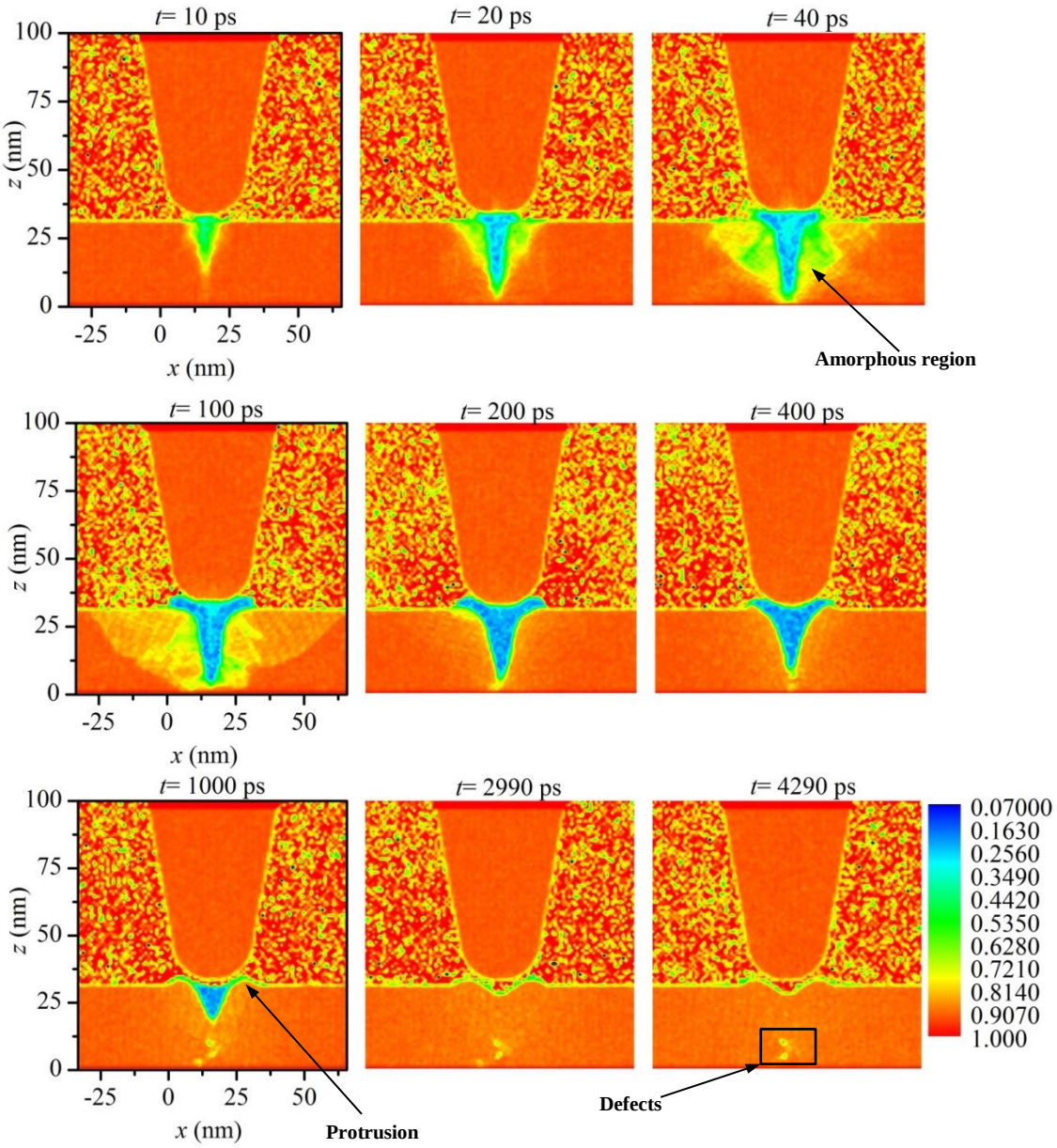

Fig. 5.5 Crystallinity contours of the case E= 5 J/m^2, d= 2 nm. The whole domain is divided into cubes of size 1×10.2 ×1 (x×y×z) nm^3. The melting area is characterized by low crystallinity (close to 0). The structure adjacent to the melting region is also destructed as shown at t= 40 ps and 100 ps. In the recrystallization process, the laser irradiation spot is the last part for full recovery in crystallinity. Defects are characterized by the low crystallinity value spots as marked in the figure at t= 4290 ps.

Figure 5.5 is the crystallinity contours for the case E= 5 J/m^2, d= 2 nm. Before laser irradiation, both the tip and the substrate are in good crystal structure and their crystallinity value

is very close to 1. Because of the laser irradiation, the melting region expands from *t*= 10 ps to *t*= 40 ps. The crystallinity value in the melting region is low and very close to 0. The crystallinity of the tip apex also drops because of its interaction with the exploded substrate plume. The amorphous region expands towards the substrate bottom as well as the in the radial direction afterwards. So the amorphous region becomes wider and deeper from *t*= 10 ps to *t*= 100 ps. From *t*= 200 ps to *t*= 2990 ps, the amorphous region shrinks. Protrusions show up at *t*= 1000 ps in the recrystallization process. At the end of the simulation, the crystallinity of both the tip and the substrate is close to 1 again which indicates good crystal structure at the steady state. Defects in the substrates at the final state can be readily identified since they have a low crystallinity value (0.5~0.7), as shown in the figure at *t*= 4290 ps.

5.2.2 Effect of constraint domain size

When the laser fluence is above the material ablation threshold, material phase explosion occurs. Systematic studies have been done to understand the plume and thermal and stress issues in laser ablation in vacuum. [18, 64] The ablated material explodes and expands into the open space with a high velocity. When an ambient gas is included in the analysis model, a shock wave is formed. Its formation and propagation has been explored in our previous works. [22, 70]

Here the tip-confinement effect is considered and studied in detail. In Fig. 5.6, the comparison of the case with free space and the ones with tip is made. The laser irradiates the substrate at first. Afterwards, laser ablation happens and shock wave forms. For the tip-free case, the ablated material can move out freely in the ambient gas and a strong shock wave is formed. Meanwhile, there are several clusters in the region 40 nm< *z* <100 nm in the tip-free case.

However, there are no clusters in the cases with tip-confinement because of the repulsive force from the tip in the near-field. And the expansion of the laser ablation is blocked by the tip. The shock wave is attenuated as well when the tip confinement is included. With the increase of the tip-substrate distance *d*, the constraint of the tip on the substrate material explosion becomes less and less. As a result, the shock wave resulting from the laser ablation becomes stronger and stronger.

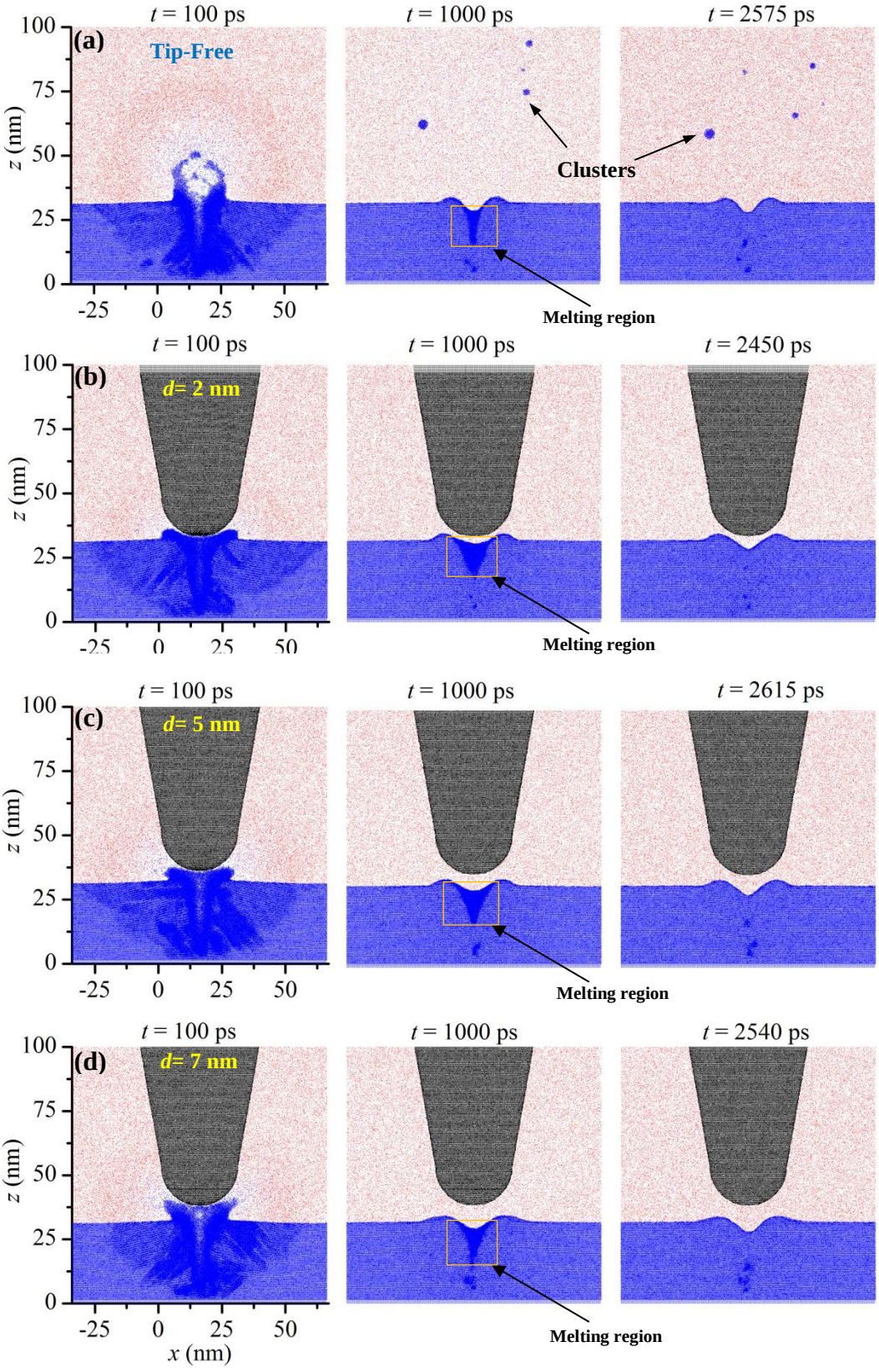
t = 100 ps
t = 1000 ps
t = 2575 ps
(a)
Tip-Free
Clusters
Melting region
t = 100 ps
t = 1000 ps
t = 2450 ps
(b)
d= 2 nm
Melting region
t = 100 ps
t = 1000 ps
t = 2615 ps
(c)
d= 5 nm
Melting region
t = 100 ps
t = 1000 ps
t = 2540 ps
(d)
d= 7 nm
Melting region
z (nm)
x (nm)
100
75
50
25
0
-25
0
25
50

Fig. 5.6 Tip confinement and tip-substrate distance effect on surface nanostructuring. For all cases, the laser fluence is E= 5 J/m^2. (a) Laser irradiation without a tip. Laser ablation and suspended clusters are observed. A strong spherical shock wave forms. (b) Tip-substrate distance d= 2 nm. (c) Tip-substrate distance d= 5 nm. (d) Tip-substrate distance d= 7 nm. For (b), (c) and (d), laser ablation is strongly blocked by the tip. The dynamics of the melting shows some different characteristics among the four cases.

Correspondingly, the comparison of the snapshots at t= 100 ps for d= 2, 5 and 7 nm demonstrates that the tip apex distortion is less severe with the increase of the tip-substrate distance. Moreover, the recrystallization process also shows some differences. At t= 1000 ps, the profile of the melting region is different. Due to the interaction of the tip and the substrate, the melting region with d= 2 nm is more widely open than the cases of d= 5 nm and 7 nm. For the tip-free case, the melting region is very narrow. So it is conclusive that the constraint by the tip also slows down the recrystallization process in substrate after laser heating.

Figure 5.7(a) is the cone-shape crater profile at the end of the simulation for different tip-substrate distance scenarios. The depth is not affected by the tip-substrate distance d too much. However, the protrusion around the crater shows different profiles. For the free space case, the protrusion height is lower and the width of the protrusion is smaller. For the cases of d= 2 nm and d= 5 nm, the protrusion and the crater match with each other very well. However, for the case d= 7 nm, the protrusion height is a little bit lower and the width becomes wider. The crater emerges first because part of the substrate material is removed in the laser ablation region. After laser ablation, part of the ejected substrate atoms move back towards the substrate because of the interaction with the ambient gas and the tip.

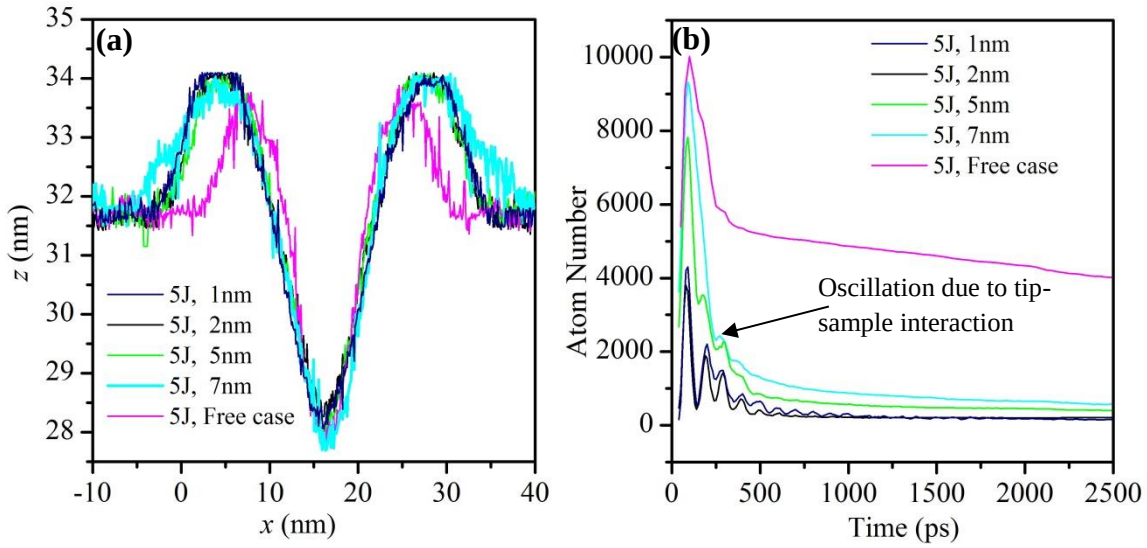

Fig. 5.7 (a) Final shape of the cone-shape crater in the substrate. The depth of the crater is not affected too much by the tip confinement. The side profile of the crater is slightly affected by the inclusion of tip confinement. The protrusion is different because of the tip and the tip-sample distance. (b) The number of atoms flying above z= 34.5 nm during the ablation process. Oscillation is observed due to the interaction of the tip and the sample.

To understand how the exploded substrate plume is affected by the tip constraint, the number of the atoms that are above z= 34.5 nm at different instants are studied [shown in Fig. 5.7(b)]. In the beginning, the laser ablation is featured with a number of atoms ejected from the substrate. The effect of the tip-constraint is outstanding. The tip-free case has more atoms ejected into the space z> 34.5 nm. Due to the tip-confinement, the atom number above z= 34.5 nm is down to 4000 for d= 1 nm from 10000 for tip-free case. For the tip-free case, the number of flying-out atoms in the final state is 3982, accounting for 0.5% of the total number of the substrate atoms. Due to the constraint effect of the tip, the atom number in the case d= 7 nm is 575 which is only 15% of the tip-free case. Furthermore, the number of flying-out atoms decreases with the decrease of the tip-substrate distance. As d= 2 nm, the flying-out atom number in the final steady state is only 198, less than 5% of the tip-free case.

Because the laser fluence is the same for all cases shown in Fig. 5.7(a), the crater shape in Fig. 5.7(a) does not differ too much for all cases. The crater depth is controlled by the laser fluence while the side profile of the crater is slightly affected by the tip confinement. The change of tip-substrate distance does not make much difference in the side profile of the crater. However, the tip-substrate distance affects the shape of the protrusion. First, the tip-confinement affects the number of the atoms flying into the free space as discussed above. Second, the tip-confinement changes the trajectories of the ejected clusters. As shown in Fig. 5.7(b), there is oscillation due to the interaction between the tip and the substrate. The oscillation is very strong for d= 1 nm and d= 2 nm since the tip-substrate distance is very small. Most of the clusters deposit on the surface close to the crater for the small tip-substrate distance. As for the tip-free case, the ejected atoms are spread in a wide region. So the protrusion is small and consists of a small number of atoms. For the case with a small tip-substrate distance, the ejected atoms deposit on the surface close to the crater. Consequently, the protrusion is higher. By increasing the distance d, the deposition region move a little bit further away. That is the reason why the protrusion width is bigger for the case of d= 7 nm.

Figures 5.8(a) and (b) show the bottom point of the crater (Z_b) and the solid-liquid interface bottom point (Z_{sl}) in the substrate. In the early stage of melting, both Z_b and Z_{sl} go down very quickly [as shown in the insets of Figs. 5.8(a) and (b)]. The crater bottom moves up quickly after the laser ablation, while the solid-liquid interface goes up slower since this process is controlled by heat conduction and solidification. For the tip-free and d= 7 nm cases, the crater bottom point is the lowest at t= 500 ps when it is still in the recrystallization process. For the d= 1 nm and d= 2 nm cases, the crater bottom point at t= 500 ps is the highest. The interaction

between the tip and the substrate leads to the small number of ejected atoms and the change of the melting interface shape. The interface is round for the d= 2 nm and d= 1 nm, while the crater bottom is relatively sharp for the tip-free case. As a result, the crater bottom point differs for different cases. The interaction between the tip and the substrate also results in the relatively slow recrystallization process. This is also observed in Fig. 5.6. The solid-liquid interface moves up in the fastest speed for the tip-free case. Then it is the d= 7 nm. Around t= 2000 ps, the recrystallization process is finished for laser fluence E= 5 J/m^2 of various tip-substrate distance. The solid-liquid interface point is gone and a stable cone-shaped crater forms. The crater bottom points of different cases in the final state are very close to each other.

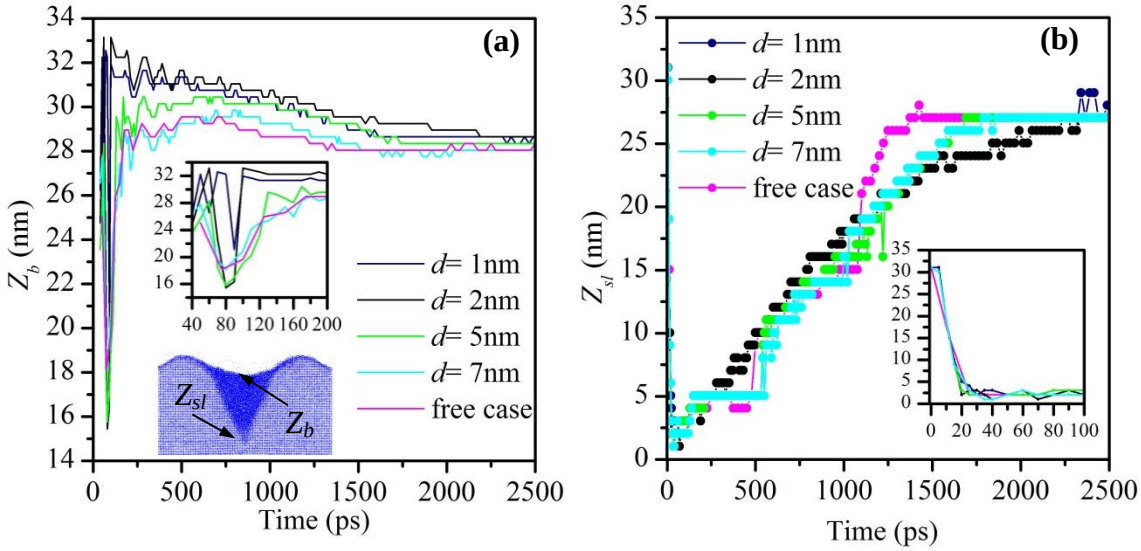

Fig. 5.8 (a) Z_b is the z bottom position of the crater during the ablation process. Z_b is going down quickly because of the laser ablation and also goes up quickly after the laser ablation. For the case of tip-free and d= 7 nm, the crater bottom point is the deepest at t= 500 ps, while d= 1 nm and 2 nm cases have the highest value. The crater bottom position for different cases is close to each other in the final stage. (b) Z_{sl} is the z position of the solid-liquid interface bottom point of the sample. Z_{sl} goes down very quickly for all the cases in the first 40 ps. The solid-liquid interface bottom point then goes up slowly for all cases. The solid-liqud interface of the tip-free case goes up in the fastest speed. And it takes the longest time for d= 1 nm and 2 nm to finish the recrystallization process.

5.2.3 Effect of laser energy on surface nanostructuring

Both the tip-substrate distance and the laser fluence play important roles in nanostructuring. Besides the various tip-substrate distance, different laser fluences (E= 2 J/m^2, 5 J/m^2, 10 J/m^2) are also studied in this work. The laser power affects the melting depth and the laser ablation process. Figure 5.9 is the snapshots and crystallinity contours under different laser fluence in the final simulation state. The crater size of the laser fluence E= 2 J/m^2 is much smaller than that of the laser fluence E= 5 J/m^2 and 10 J/m^2. The defects position of the low laser fluence case (E= 2 J/m^2) is much higher than that of the high laser fluence (E= 5 J/m^2 , 10 J/m^2). Large-size defects occur in the case with E= 10 J/m^2. Owing to the high laser energy, even after a long time recrystallization, the part near the crater is still in low crystallinity value which features bad crystal structure.

Figure 5.10(a) shows the crater profile for two different fluences. The width and depth of crater for the case E= 2 J/m^2 is smaller than that of the case E= 5 J/m^2. The protrusion size is also smaller for the low laser energy case. When the laser fluence is decreased, the atom number ejected from the substrate is also decreasing in the ablation. Consequently, a crater of smaller size is formed and the protrusion around the crater is also smaller. Figure 5.10(b) demonstrates that the solid-liquid interface bottom point Z_{sl} is higher for E= 2 J/m^2. This accounts for the location changes of these defects as shown in Fig. 5.9(a). For the small laser fluence, the melting depth is small and Z_{sl} is closer to the upper substrate surface. And the effect of the laser fluence on the bottom part of the substrate is small. As a result, the defect part is close to the upper surface. Otherwise it is close to the bottom part. The high laser fluence also effectively increases

the time of crystallization. It takes 2500 ps for the case E= 5 J/m^2 to get fully recrystallized. It is almost the 3 times of that for the case E= 2 J/m^2.

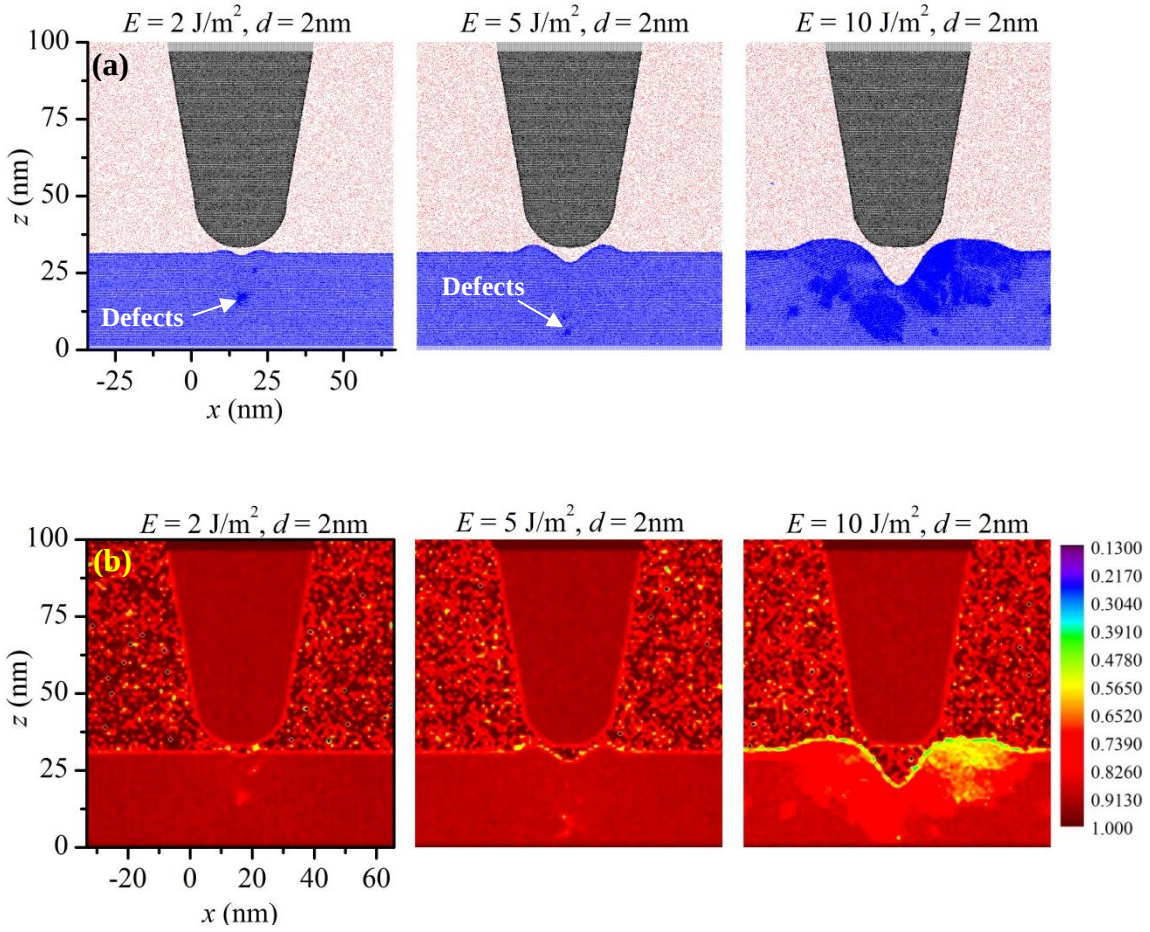

Fig. 5.9 Comparison of final structure under different laser fluences. The time points for the 3 cases are: E= 2 J/m^2, d= 2 nm, at t= 1440 ps; E= 5 J/m^2, d= 2 nm, at t= 4290 ps; E= 10 J/m^2, d= 2 nm, at t= 4940 ps. (a) The final profile of the nanostructuring in final steady state. The crater size under laser fluence E= 10 J/m^2 is the biggest one and the laser fluence E= 2 J/m^2 gives the smallest crater. (b) Crystallinity of the final structure under different lase fluences. Defects are clearly observed. The position of defects for laser fluence E= 2 J/m^2 is higher than that of the laser fluence E= 5 J/m^2. The defects are larger in size for laser fluence E= 10 J/m^2. This concludes when the laser fluence is becoming higher, larger and deeper defects are formed within the substrate.

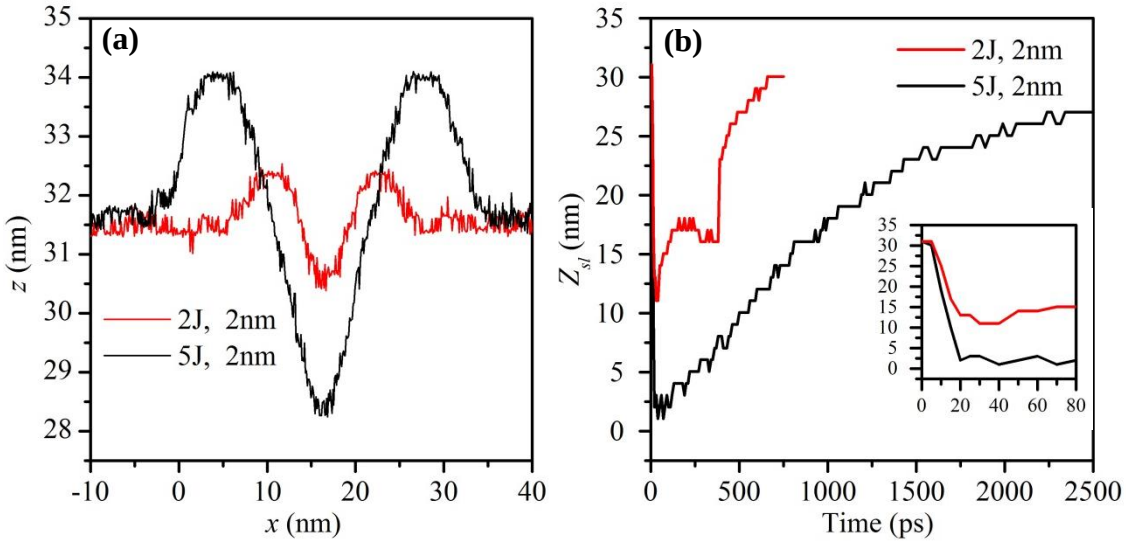

Fig. 5.10 (a) Comparison of the profile and the final nanostructure surface to show the laser fluence effect. For high laser fluence E= 5 J/m^2, the width and height of the cone-shape crater is bigger. And the protrusion is higher than that of E= 2 J/m^2. (b) Evolution of the solid-liquid interface bottom point Z_{sl} under different laser fluences. For the case of E= 2 J/m^2, the melting depth is much smaller than the case of laser fluence E= 5 J/m^2. Also it takes a much shorter time for the crater to fully form and get stable for the case of E= 2 J/m^2.

5.2.4 Tip distortion by the domain constraint

The tip is affected by the laser fluence as well. In SPM-based nanomanufacturing, this effect is a big concern, and usually requires frequent replacement of the SPM tip after a certain time of use. Figure 5.11(a) shows the effect of different laser fluence on the tip. They are the snapshots at t= 1440 ps. The tip apex is distorted seriously under the laser fluence of E= 10 J/m^2. The shape of the tip apex for the case E= 10 J/m^2 is more blunt than the case E= 5 J/m^2. Tip wear and thermal expansion is always a concern of researchers in the nanostructuring process. In Fig. 5.9(a), the tip apex is reshaped and blunt even after recrystallization for almost 5 ns when E= 10 J/m^2. However, the simulation results show that it is not only related to the laser fluence. The tip-substrate distance is also important for the tip distortion. Figure 5.11(b) shows the tip distortion

at t= 40 ps for different tip-substrate distance. For the case with tip-substrate distance d= 2 nm, the degree of distortion is more than that of the tip-substrate distance d= 7 nm. It is readily to understand that the interaction between the tip and the substrate is stronger when the distance is smaller. This stronger interaction leads to more severe tip apex damage and distortion.

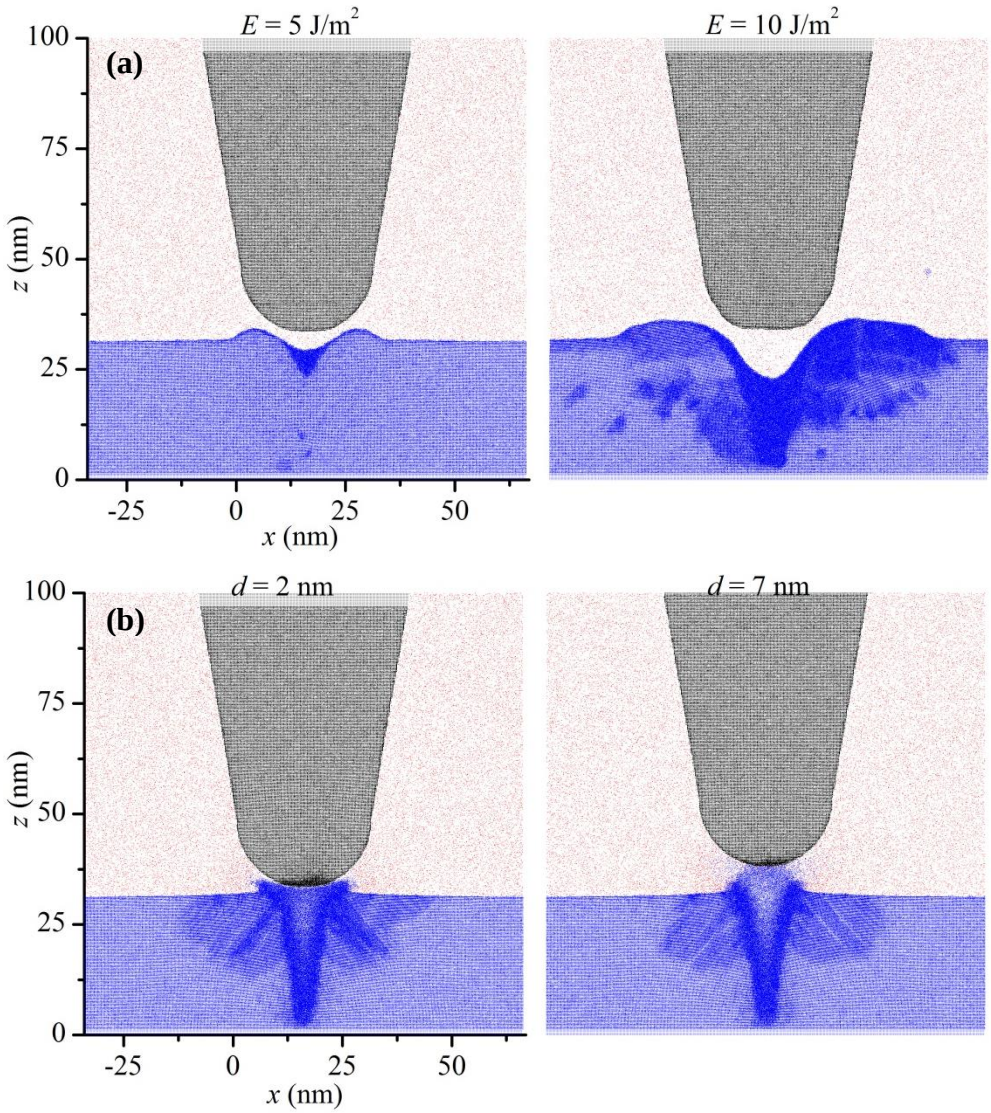

Fig. 5.11 (a) Tip profile at t= 1440 ps. For both cases, the tip-sample distance is d= 2 nm. The comparison shows that for a laser fluence as high as E= 10 J/m^2, the tip apex are seriously distorted and the shape is more blunt than the case of E= 5 J/m^2. (b) Tip profile at t= 40 ps. For both cases, the laser fluence is 5 J/m^2 . The degree of tip distortion is more serious for d= 2 nm than 5 nm.

Besides permanent apex distortion, we also observe oscillation of the tip apex during surface nanostructuring due to the interaction with the substrate. Figure 5.12 shows the movement of the tip apex. The oscillation of the tip is clearly observed. Meanwhile, the oscillation of the tip results in the oscillation of the substrate in the recrystallization process. The oscillation is in a relatively high frequency at the beginning because of the explosion of the target material in the laser ablation. For the case E= 5 J/m^2, d= 2 nm, the oscillation frequency becomes very small after 1500 ps. The oscillation is related to the tip-substrate distance and the laser fluence. When d= 7 nm, the frequency change is not as obvious as d= 2 nm. And the oscillation amplitude is big for the close tip-substrate distance since the interaction between the tip and the substrate is attenuated if the tip and substrate distance increases. The ablation weakens if the laser fluence is decreased. That is why the oscillation for the case E= 2 J/m^2 is negligible while the oscillation in the case of E= 5 J/m^2 is strong.

To have a deep insight of the constraint effect of the tip on the exploded plume dynamics, a window of size of $4\times10\times2$ nm^3($x\times y\times z$) beneath the tip is chosen as the area for temperature monitoring to study the constraint effect. For all the cases, the temperature in this window increases at first because of the laser ablation. Then the temperature decreases after around t= 30 ps. This is because at the later time, the ablated material deposited on the surface or they fly away from this window. When the tip-sample distance d is as small as 1 nm and 2 nm, the window temperature is higher than the free case during the laser ablation (t< 50 ps). The tip sets up the spatial confinement for the spread of the ablated material. When the tip-sample distance is small, the ablated material is trapped in the near field for a long time. That explains why the temperature in the window for d= 1 nm are 2 nm can reach a higher value.

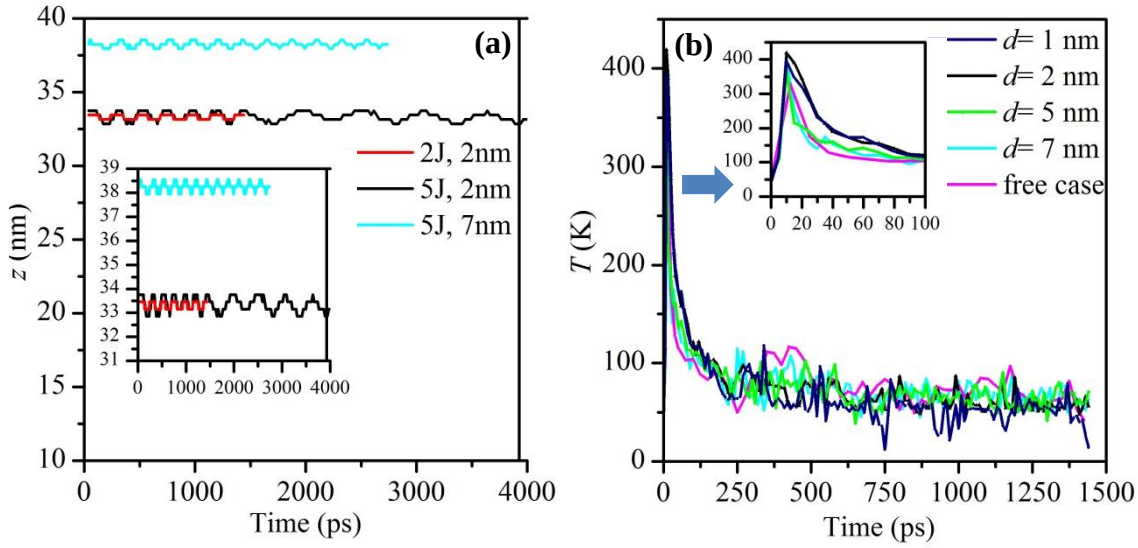

Fig. 5.12 (a) Variation of the position of the lowest point of the tip during surface nanostructuring. The tip moves up and down along the *z* direction and it is very clear that the tip oscillates more frequently at the beginning for the case E= 5 J/m^2, d= 2 nm. With time going by, the tip oscillation frequency decreases; (b) A window of size of 4×10×2 nm^3(x×y×z) beneath the tip is chosen as the area for temperature monitoring. For all the cases, the laser fluence is E= 5 J/m^2. The temperature in this window increases at first because of the laser ablation. Then it decreases since at the later time the ablated material deposits on the surface or they fly away from this window.

CHAPTER 6. CONCLUSIONS AND FUTURE WORK

6.1. Conclusions for effect of shock wave phase change and stress wave in pico-second laser material interaction

Systematic atomistic modeling has been conducted to study the shock wave formation in picosecond laser material interaction and the effect of shock wave on phase change and stress wave development and propagation. The bubbles grew in a fast speed and then decelerated in growth. Larger bubbles were found to maintain their large volume for a longer time. As to the contraction and collapsing process, all the bubbles experience fast contracting and then disappear slowly, and this process is almost symmetrical to the growing process with respect to time. Existence of the shock wave significantly suppressed the bubble growth and their lifetime. No effect from shock wave on the stress wave in solid was observed in this work. The decrease of the absorption depth and increase in laser fluence led to a sharp drop in stress wave front. Furthermore, ablated cluster re-deposition was found to generate a secondary stress wave in the target. The magnitude of this secondary (~15 MPa) stress wave is much smaller than that of the first primary laser-induced stress wave (~140 MPa). There is a close, almost linear relationship between the laser fluence and the stress wave maximum value. Under a laser fluence of 40 J/m^2, the stress wave in the target has a maximum compressive component exceeding 1.5 GPa.

6.2. Conclusions for structure evolution of nanoparticles under pico-second stress wave consolidation

MD simulations were conducted to investigate nanoparticle consolidation by a stress wave induced by pico-second laser ablation of a sacrificial layer. Upon fast laser irradiation, the

sacrificial layer quickly melted and phase exploded. Under the constrained domain, the exploded sacrificial layer atoms quickly moved to the nanoparticles and compressed them. Our detailed temperature and structure study revealed that the compression and reconstruction process was rather cold and well below the melting point of the material. On the other hand, destruction and reconstruction took place, and finally cold-sintering of the nanoparticles was achieved. The final cold-sintered structure was found to be nanocrystalline. Smaller nanoparticles were easy to reconstruct, but the final structure was more destructed, and structural defects were observed. For larger particles, the final cold-sintered structure was partially nanocrystalline. The center part of the particle was able to retain its original crystalline structure while consolidation occurred more in the particle-particle contact region. The ODF was developed to investigate the degree of orientation twisting. It was proved to be more comprehensive than RDF in structure analysis for the additional angle information it provides. Our quantitative analysis of the number of reconstructed atoms also showed that the number of reconstructed atoms is higher when the particle size is smaller.

6.3. Conclusions for shock wave confinement-induced plume temperature increase in laser-induced breakdown spectroscopy

MD simulations were conducted to investigate the spatial confinement effect on shock wave and the resulting boost in plume temperature and lifetime. The temperature, pressure and number density of the shock wave were observed to increase dramatically immediately after the reflection from the wall. The reflected shock wave and the forward-moving shock wave had a strong collision, and such an atomic collision/friction makes the velocity of the shock wave decreases to almost zero after reflection. This means a large part of the kinetic energy is

converted to the thermal energy of the shock wave. A temperature rise as high as 218 *K* was observed for the shock wave front after the wall reflection. The big difference of the pressure between the plume and ambient gas after the reflection caused the ambient gas to move back towards the plume. Finally, the plume was compressed by the reflected shock wave. In the compression process, the ejected clusters recombined with each other. The downward velocity of the plume increased dramatically. More importantly, the temperature of the plume is enhanced dramatically from 89 *K* to 132 *K*. Also this high temperature was maintained for quite a long time. This explains the sensitivity enhancement in the spatial confinement of LIBS. If we took 100 *K* as the criterion for plume radiation sensing in our modeling, the lifetime of the plume was increased from 480 ps (free space case) to more than 1800 ps. This could further improve the sensitivity of LIBS via spatial confinement.

6.4. Conclusions for material behavior under extreme domain constraint in laser-assisted surface nanostructuring

Systematic atomistic modeling has been conducted to understand the tip-confinement effect on surface nanostructuring. Material ablation was trapped by the tip and a significant decrease of the number of atoms flying out of the surface was observed. For tip-free laser-induced surface ablation, large atom clusters were observed in our reference modeling. However, for tip-confined laser-ablation, no such clusters were observed. Tip oscillation occurred because of the tip interaction with the substrate during laser ablation. The profile of the cone-shape crater was not affected by the tip substrate distance too much. The laser fluence played the dominant role in the crater characterization. The protrusion around the crater was affected by the tip-substrate distance and the laser fluence. The recrystallization process was significantly

influenced by the tip-confinement. The recrystallization time was longer for the case with stronger tip confinement. This is because of the interaction between the tip and the substrate: the confinement prevents high energy atoms from flying out. As a result, more laser energy was left to the substrate. The tip apex was distorted during the laser ablation. Both the tip-substrate distance and the laser fluence played import roles in the distortion. For the case of E= 10 J/m^2, the tip apex was reshaped to be blunt. In tip-based laser surface nanostructuring, careful control of the tip-substrate distance and laser energy becomes critical to maintain a sound tip-apex geometry for both structure quality control and prolonged life time of the tip before it gives intolerable surface nanostructures.

6.5 Future work

Up to now, our research focus has been placed on the single laser irradiation scenario. And the spatial confinement is from the ambient gas, potential wall or the tip in the nanostructuring. Like the sound wave, the stress wave and shock wave can interfere with each other if multiple laser irradiation spots exist. Figure 6.1 is the model of multiple irradiation spots. Since the underlying physical process is to be investigated, argon can be chosen as the material for this modeling.

The size of the substrate and the position of the laser spots are important since we are interested in the stress/thermal wave interference. The interference needs to happen before the wave reflection at boundaries. Periodic boundary condition is adopted. The two laser irradiation spots are symmetric about the symmetric axis of the substrate on the x-y plane. d_{bx} and d_{by} is 3

times of *d*. Target size along *z* axis is also 3 times of *d*. Single pico-second laser pulse is applied at the same time to the two spots.

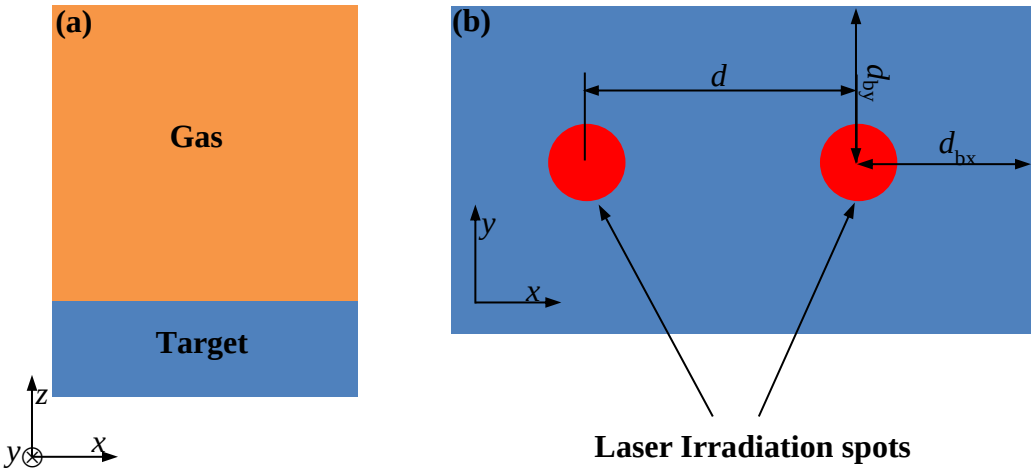

Fig. 6.1 Illustration of multiple laser irradiation spots. The distance between the two spots *d* and the size of the target is going to affect the interference of the stress wave and thermal wave in space. Different combination of the distance *d* and size of target can be investigated. (a) *x*-*z* plane model profile. (b) *x*-*y* plane model profile.

Figure 6.2(a) is a simple demonstration of the interference of the shock wave. The temperature and pressure of the shock wave front is expected to rise more. And cluster re-combination and the trajectories of the clusters are expected to change. The re-deposition of cluster is possibly very different from the vacuum and the ambient gas case. In addition, the place where the shock wave interference happens may have different surface features. Stress and thermal transport can be viewed as the form of wave. Their interference may result in local stress/temperature rise.

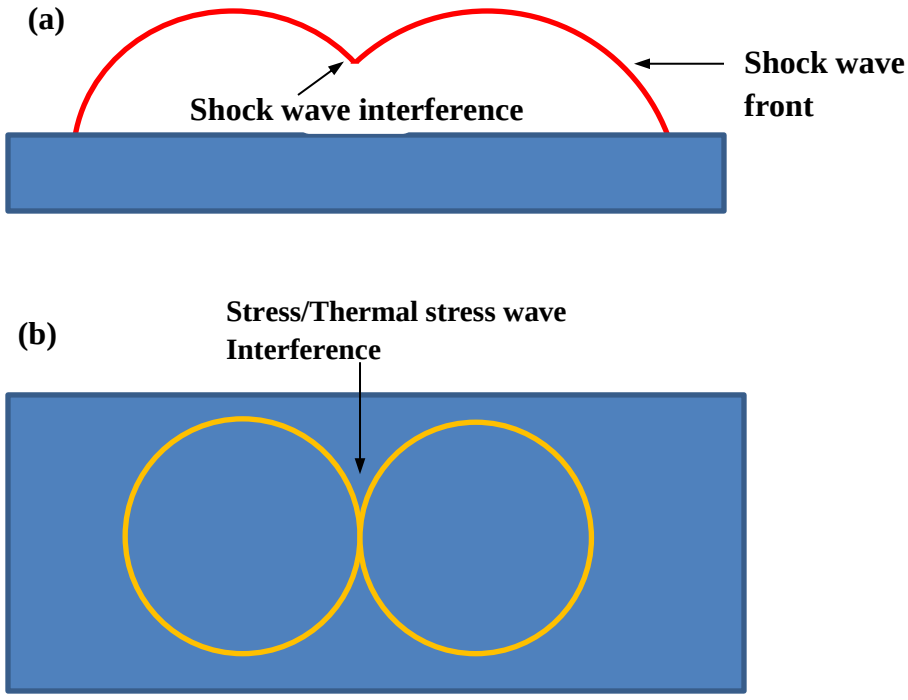

Fig. 6.2 (a) Illustration of shock wave interference. Due to superposition of the shock wave, the temperature, pressure of the shock wave front are expected to rise more than half of the single shock wave. Cluster recombination may happen at the interface. (b) Illustration of stress/thermal wave interference. The interference may result in the temperature and stress dramatic rise.

REFERENCES

[1] Piseth Seng, Michel Drancourt, Frédérique Gouriet, Bernard La Scola, Pierre-Edouard. Fournier, Jean Marc Rolain and Didier Raoult, Clinical Infectious Diseases **49**, 543 (2009).

[2] T. Takiya, I. Umezu, M. Yaga, and M. Han, Journal of Physics: Conference Series **59,** 445 (2007).

[3] S. Amoruso, G. Ausanio, R. Bruzzese, M. Vitiello, and X. Wang, Physical Review B **71,** 033406 (2005).

[4] Anton Plech, Vassilios Kotaidis, Maciej Lorenc, and Johannes Boneberg, Nature Physics **2,** 44 (2005).

[5] Michael N. R. Ashfold, Frederik Claeyssens, Gareth M. Fuge and Simon J. Henley, Chemical Society Reviews **33**, 23 (2004).

[6] S. Amoruso, R. Bruzzese, M. Vitiello, N. N. Nedialkov and P. A. Atanasov, Journal of Applied Physics **98**, 044907 (2005).

[7] Xinwei Wang and Xianfan Xu, Journal of Heat Transfer **124**, 265 (2002).

[8] Kevin H Song and Xianfan Xu, Applied Surface Science **127**, 111 (1998).

[9] Xianfan Xu and David A. Willis, Journal of Heat Transfer **124**, 293 (2002).

[10] Xianfan Xu, Applied Surface Science **197**, 61 (2002).

[11] Hee K. Park, Costas P. Grigoropoulos, Chie C. Poon and Andrew C. Tam, Applied Physics Letters **68**, 596 (1996).

[12] O. Yavas, P. Leiderer, H. K. Park, C. P. Grigoropoulos, C. C. Poon, W. P. Leung, N. Do and A. C. Tam, Applied Physics A **58**, 407-415 (1994).

[13] S. S. Harilal, C. V. Bindhu, M. S. Tillack, F. Najmabadi and A. C. Gaeris, Journal of Applied Physics **93**, 2380 (2003).

[14] David B. Geohegan, Thin Solid Films **220**, 138 (1992).

[15] Leonid V. Zhigilei, Elodie Leveugle, Barbara J. Garrison, Yaroslava G. Yinglingand Michael I. Zeifman, Chemical Review **103**, 321 (2003).

[16] Lijun Zhang and Xinwei Wang, Applied Surface Science **255**, 3097 (2008).

[17] Leonid V. Zhigilei and Barbara J. Garrison, Applied Physics Letters **71**, 551 (1997).

[18] L. V. Zhigilei, Applied Physics A **76**, 339 (2003).

[19] J. N. Leboeuf, K. R. Chen, J. M. Donato, D. B. Geohegan, C. L. Liu, A. A. Puretzky and R. F. Wood, Applied Surface Science **96-98**, 14 (1996).

[20] Xuhui Feng and Xinwei Wang, Physics Letters A **369**, 323 (2007).

[21] Cristian Porneala and David A. Willis, Applied Physics Letters **89**, 211121 (2006).

[22] Sobieslaw Gacek, Xinwei Wang, Applied Physics A **94**, 675 (2008).

[23] Lijun Zhang and Xinwei Wang, Japanese Journal of Applied Physics **47**, 964 (2008).

[24] Sobieslaw Gacek and Xinwei Wang, Journal of Applied Physics **104**, 126101 (2008).

[25] Xinwei Wang, Journal of Physics D: Applied Physics **38**, 1805 (2005).

[26] Wenwu Zhang, Y. Lawrence Yao and I. C. Noyan, , Journal of Manufacturing Science and Engineering **126,** 10 (2004).

[27] Wenwu Zhang and Y. Lawrence Yao, Journal of Manufacturing Science and Engineering **124,** 369 (2002).

[28] Pal Molian, Raathai Molian, and Rajeev Nair, Applied Surface Science **255,** 3859 (2009).

[29] P. Peyre, X. Scherpereel, L. Berthe, C. Carboni, R. Fabbro, G. Béranger, and C. Lemaitre, Materials Science and Engineering: A **280,** 294 (2000).

[30] Dong Lin, Chang Ye, Yiliang Liao, Sergey Suslov, Richard Liu, and Gary J. Cheng, Journal of Applied Physics **113,** 133509 (2013).

[31] H. K. Amarchinta, R. V. Grandhi, K. Langer, and D. S. Stargel, Modelling and Simulation in Materials Science and Engineering **17,** 015010 (2009).

[32] J. H. Kim, Y. J. Kim, and J. S. Kim, Journal of Mechanical Science and Technology **27,** 2025 (2013).

[33] W. Braisted and R. Brockman, International Journal of Fatigue **21,** 719 (1999).

[34] R. Nair, W. Jiang, and P. Molian, Journal of Manufacturing Science and Engineering **126,** 637 (2004).

[35] Francisco J. Fortes, Javier Moros, Patricia Lucena, Luisa M. Cabalín and J. Javier Laserna, Analytical Chemistry **85**, 640 (2012).

[36] R. Noll, H. Bette, A. Brysch, M. Kraushaar, I. Mönch, L. Peter and V. Sturm, Spectrochimica Acta Part B: Atomic Spectroscopy **56**, 637 (2001).

[37] Hahn DW, Omenetto N, Applied Spectroscopy **66**, 347 (2012).

[38] L. J. Radziemski, Spectrochimica Acta Part B: Atomic Spectroscopy **57**, 1109 (2002).

[39] J. D. Pedarnig, P. Kolmhofer, N. Huber, B. Praher, J. Heitz and R. Rössler, Applied Physics A **112**, 105 (2013).

[40] I. B. Gornushkin, B. W. Smith, H. Nasajpour and J. D. Winefordner, Analytical Chemistry **71**, 5157 (1999).

[41] Rosalba Gaudiuso, Marcella Dell'Aglio, Olga De Pascale, Giorgio S. Senesi and Alessandro De Giacomo, Sensors **10**, 7434 (2010).

[42] Savas Georgiou, Demetrios Anglos and Costas Fotakis, Contemporary Physics **49**, 1 (2008).

[43] Volker Sturm, Jens Vrenegor, Reinhard Noll and Michel Hemmerlin, Journal of Analytical Atomic Spectrometry **19**, 451-456 (2004).

[44] Owen T. Butler, Warren R. L. Cairns, Jennifer M. Cook and Christine M. Davidson, Environmental analysis. Journal of Analytical Atomic Spectrometry **27**, 187-221 (2012).

[45] Russell S. Harmon, Frank C. DeLucia, Catherine E. McManus, Nancy J. McMillan, Thomas F. Jenkins, Marianne E. Walsh and Andrzej Miziolek, *Applied Geochemistry* **21**, 730-747 (2006).

[46] C. G. Brown, R. Bernath, M. Fisher, M. C. Richardson, M. Sigman, R. A. Walters, A. Miziolek, H. Bereket, L. E. Johnson, Proc. Of SPIE **6219**, 62190B-1-62190B- 7 (2006).

[47] J. Gruber, J. Heitz, H. Strasser, D. Bäuerle and N. Ramaseder, Spectrochimica Acta Part B: Atomic Spectroscopy **56**, 685 (2001).

[48] Samek O, Beddows DCS, Kaiser J, Kukhlevsky SV, Liška M, Telle HH *et al*. Optical Engineering **39**, 2248-2262 (2000).

[49] Jon Scaffidi, S. Michael Angel and David A. Cremers, Analytical Chemistry **78**, 24 (2006).

[50] L. St-Onge, V. Detalle and M. Sabsabi, Spectrochimica Acta Part B: Atomic Spectroscopy **57**, 121 (2002).

[51] R. W. Coons, S. S. Harilal, S. M. Hassan and A. Hassanein, Applied Physics B **107**, 873 (2012).

[52] V. I. Babushok, F. C. DeLucia Jr, J. L. Gottfried, C. A. Munson and A. W. Miziolek, Spectrochimica Acta Part B: Atomic Spectroscopy **61**, 999-1014 (2006).

[53] Jinzhong Chen, Zhenyu Chen, Jiang Sun, Xu Li, Zechao Deng and Yinglong Wang, Applied Optics **51**, 8141 (2012).

[54] G. Abdellatif and H. Imam, Spectrochimica Acta Part B: Atomic Spectroscopy **57**, 1155 (2002).

[55] F. Anabitarte, A. Cobo and J. M. Lopez-Higuera, *ISRN Spectroscopy* **2012**, 1-12 (2012).

[56] A. Elhassan, A. Giakoumaki, D. Anglos, G. M. Ingo, L. Robbiola and M. A. Harith, Spectrochimica Acta Part B: Atomic Spectroscopy **63**, 504-511 (2008).

[57] Nakimana Agnes, Tao Hai-Yan, Hao Zuo-Qiang, Sun Chang-Kai, Gao Xun, Lin Jing-Quan, Chinese Physics B **22**, 014209 (2013).

[58] T. Dunbar, B. Maynard, D. A. Thomas, M. D. M. Peri, I. Varghese and C. Cetinkaya, Journal of Adhesion Science and Technology **21**, 67 (2007).

[59] X. K. Shen, J. Sun, H. Ling and Y. F. Lu, Applied Physics Letters **91**, 081501 (2007).

[60] X. K. Shen, J. Sun, H. Ling and Y. F. Lu, Journal of Applied Physics **102**, 093301 (2007).

[61] L. B. Guo, C. M. Li, W. Hu, Y. S. Zhou, B. Y. Zhang, Z. X. Cai, X. Y. Zeng and Y. F. Lu, Applied Physics Letters **98**, 131501 (2011).

[62] Andrey M. Popov, Francesco Colao and Roberta Fantoni, Journal of Analytical Atomic Spectrometry **25**, 837 (2010).

[63] Steve Plimpton, Journal of Computational Physics **117**, 1 (1995).

[64] Leonid V. Zhigilei and Barbara J. Garrison, Journal of Applied Physics **88**, 1281 (2000).

[65] A. Vogel, R. Engelhardt, U. Behnle and U. Parlitz, Applied Physics B **62**, 173-182 (1996).

[66] Xinwei Wang, Journal of Heat Transfer **126**, 355 (2004).

[67] X. Wang and X. Xu, Applied Physics A **73**, 107-114 (2001).

[68] Xinwei Wang and Yongfeng Lu, Journal of Applied Physics **98,** 114304 (2005).

[69] Xuhui Feng and Xinwei Wang, Applied Surface Science **254,** 4201 (2008).

[70] Chong Li, Jingchao Zhang, Xinwei Wang, Applied Physics A **112**, 677-687 (2013).

[71] Leonid V. Zhigilei and Barbara J. Garrison, MRS Proceedings **538**, 491 (1998).

[72] Xinwei Wang and Xianfan Xu, International Journal of Heat and Mass Transfer **46**, 45-53(2003).

[73] A., Chimmalgi, C.P. Grigoropoulos, and K. Komvopoulos, Journal of Applied Physics **97**, 104319 (2005).

[74] R. Huber, M. Koch, and J. Feldmann, Applied Physics Letters **73**, 2521 (1998).

[75] A. Lewis, M. Isaacson, A. Harootunian, A. Murray, Ultramicroscopy **13**, 227 (1984).

[76] D. W. Pohl, W. Denk and M. Lanz, Applied Physics Letter **44**, 651 (1984).

[77] G. Binning and C. F. Quate, Physical Review Letters **56**,930 (1986).

[78] E. Meyer, Progress in Surface Science **41**, 3 (1992).

[79] Yasushi Inouye, and Satoshi Kawata, Optics Letters **19**, 159 (1994).

[80] Neil. Anderson, Pascal Anger, Achim Hartschuh and Lukas Novotny, Nano Letters **6,** 744 (2006).

[81] Vladimir V. Protasenko, and Alan C. Gallagher, Nano Letters **4**, 1329 (2004).

[82] Gerd Kaupp, Andreas Herrmann, and Michael Haak, Journal of Physical Organic Chemistry **12**, 797 (1999).

[83] Stefan Grafström, Journal of Applied Physics **91**, 1717 (2002).

[84] G. Binnig, C.F. Quate, and C. Gerber, Physical Review Letters **56**, 930 (1986).

[85]. J. Koglin, U.C. Fischer, and H. Fuchs,. Physical Review B **55**, 7977 (1997).

[86]. F. Zenhausern, Y. Martin, and H.K. Wickramasinghe **269**, 1083 (1995).

[87]. J. Jersch, F. Demming, and K. Dickmann, Applied Physics A **64**, 29 (1996).

[88] S.M. Huang , M. H. Hong, Y. F. Lu, B.S. Lukỳanchuk, W. D. Song and T. C. Chong, Journal of Applied Physics **91**, 3268 (2002).

[89] GN Makarov, Physics-Uspekhi **56**, 643 (2013).

[90] R. Bachelot, *et al*., Journal of Applied Physics **94**, 2060 (2003).

[91] Yves C.Martin, Hendrik F. Hamann, and H.Kumar Wickramasinghe,. Journal of Applied Physics **89**, 5774 (2001).

[92] John L. Bohn, D.J. Nesbitt, and A. Gallagher, Journal of the Optical Society of America A **18**, 2998 (2001).

[93] Xiaoduan Tang, Yanan Yue, Xiangwen Chen and Xinwei Wang, Optics Express **20**, 14152 (2012).

[94] Yong-Feng Lu, Zhi-Hong Mai, Wai-Kin Chim,. Japanese Journal of Applied Physics **38,** 5910 (1999).

[95] J. Boneberg, H.-J. Münzer, M. Tresp, M. Ochmann and P. Leiderer, Applied Physics A **67**, 381 (1998).

[96] V.A. Ukraintsev, and J.T. Yates, Journal of Applied Physics **80**, 2561 (1996).

[97] I., Lyubinetsky, Z. Dohnálek ,V. A. Ukraintsev and J. T. Yates Jr., Journal of Applied Physics **82**, 4115 (1997).

[98] Ch. Lienau, A. Richter, and T. Elsaesser, Applied Physics Letters **69**, 325 (1996).

[99] Yong-Feng Lu, Bing Hu, Zhi-Hong Mai, Wei-Jie Wang, Wai-Kin Chim and Tow-Chong Chong, Japanese Journal of Applied Physics **40**, 4395 (2001).

[100] Y.F. Lu, Z. H. Mai, Y. W. Zheng and W. D. Song,. Applied Physics Letters **76**, 1200 (2000).

[101] David L. Jeanmaire, Richard P. Van Duyne, Journal of Electroanalytical Chemistry and Interfacial Electrochemistry **84**, 1 (1977).

[102] Alan Campion and Patanjali Kambhampati, Chemical Society Reviews **27,** 241 (1998).

[103] Katrin Kneipp, Physics Today **60**, 40 (2007).

[104] Mark S. Anderson, Applied Physics Letter **76,** 3130 (2000).

[105] Elena Bailo and Volker Deckert, Chemical Society Review **37**, 921 (2008).

[106] Andrew Downes, Donald Salter and Alistair Elfick, Journal of Physical Chemistry B **110**, 6692 (2006).

[107] Geshev P I, Fischer U and Fuchs H, Physics Review B **81**, 125441 (2010).

[108] Z.Q. Tian, B. Ren, and B.W. Mao, The Journal of Physical Chemistry B **101**, 1338 (1997).

[109] Alexander A. Milner, Kaiyin Zhang, Valery Garmider, Yehiam Prior, Applied Physics A **99**, 1 (2010).

[110] Brendan McCarthy, Yanming Zhao, Ranjan Grover and Dror Sarid, Applied Physics Letters **86**, 111914 (2005).

[111] Xiangwen Chen, Xinwei Wang, Nanotechnology **22**, 075204 (2011).

[112] Yanan Yue, Xiangwen Chen, and Xinwei Wang, ACS Nano **5**, 4466 (2011).

[113] Chong Li, Kelsey Burney, Kevin Bergler, Xinwei Wang, Computational Materials Science **95**, 74 (2014).

[114] Chong Li, Jianmei Wang, and Xinwei Wang, Physics Letters A **378**, 3319 (2014).

[115] Liying Guo and Xinwei Wang, Journal of Physics D: Applied Physics **42**, 015307 (2009).

[116] Sobieslaw Gacek, Xinwei Wang, Physics Letters A **373**, 3342 (2009).